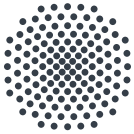

Universität Stuttgart

Towards highly efficient single photon detectors for near- and mid-infrared using integrated niobium plasmonics

Von der Fakultät Mathematik und Physik
der Universität Stuttgart zur Erlangung der Würde
eines Doktors der Naturwissenschaften (Dr. rer. nat.)
genehmigte Abhandlung

vorgelegt von

Philipp Karl
aus Herrenberg

Hauptberichter:	Prof. Dr. Harald Giessen
Mitberichter:	Prof. Dr. Peter Michler
Prüfungsvorsitzende:	Prof. Dr. Maria Daghofer

Tag der mündlichen Prüfung: 26. Juli 2023

4. Physikalisches Institut der Universität Stuttgart
2023

Philipp Karl: *Towards highly efficient single photon detectors for near- and mid-infrared using integrated niobium plasmonics*, 2023

Für meine Familie, Freunde und mich.

The difference between screwing around and science is writing it down.

— Adam Savage

ABSTRACT

Analyzing and detecting light is crucial in several areas of technologies. One interesting and exciting phenomena which can be utilized here is the resonant interaction of light with metallic nanoparticles. These so-called plasmonic resonances and corresponding nanostructures are constantly used in new technological applications to enhance, improve or enable various different technologies. In most cases noble metals are used, due to their beneficial optical properties. However, other metals, such as niobium-based materials like niobium itself, niobium nitride and niobium titanium nitride, also provide excellent plasmonic properties, which we have demonstrated in this work, and can therefore be used for plasmonic applications. More important, these niobium-based metals exhibit an additional interesting and useful characteristic, namely they are superconductors.

This superconducting behavior can be used to fabricate superconducting nanowire single photon detectors, utilizing the superconducting-to-normal-conducting phase transition to detect even single photons. They enable high efficient, precise and fast photo detection, which is required for quantum applications. Avalanche photo diodes were used in the past, but they are not able to keep up with the new developments and required speed. The big challenge for these new superconducting nanowire detectors is to reduce the trade-off between detection efficiency, which requires larger active areas, and speed, which requires small active areas, since their recovery time scales with the inductance, and hence the length of the detector structure.

To address this problems, we take advantage of the high resonant absorbing cross section of plasmonic resonances, by utilizing the so-called plasmonic perfect absorber principle, to reach near 100% absorption, even with small active areas and also in the infrared spectral range. First we have simulated niobium-based nanowire arrays on a perfect absorber substrate, since they lay the foundation of the detector structures. These simulations have revealed high absorbing, broad and tunable plasmon resonances, with over 99% absorption over a wide spectral range. Hereby the plasmonic resonances shift red, for larger wire widths, due to their dipole nature. The fabricated samples have confirmed these results and measurements have shown an absorption of over 95%. Even the smaller detector structures with

an active area of only $30 \times 30\ \mu m^2$ exhibit a maximum absorption of around 90 - 95% at our target wavelength of 1140 nm. The finished detector is able to detect laser powers below 1 µW in TM polarization. In TE polarization a minimum of $\approx 2\ \mu W$ is needed, confirming a stronger response and hence a higher detection efficiency for TM polarized light, where the plasmons are excited. In addition, this leads to a polarization-dependent detector response. Further, we have investigated different polarization-independent detector designs, with a maximum absorption of around 90% and measured their absorption and response to an external light source.

After confirming the functionality of our detectors we have fabricated ultra-small and fiber-coupled detectors with an active area of only $3 \times 3\ \mu m^2$, by utilizing 3D-printed fiber optics for focusing, fiber chucks for alignment and the angular independence of the plasmonic perfect absorber principle. After the evaluation of measurements with the new design and setup, we have been able to calculate the number of the incoming photons on these detectors. With these results we have estimated that our structures can measure pulses containing in average only single-digit photon numbers. This is an important step towards single photon detection, since it shows that already pulses with photon numbers on the order of single photons cause a change in our detector. However, due to the bad signal-to-noise ratio this is not possible without lock-in at the moment. In addition, we estimated that our detectors have at least a detection efficiency of about 80%, which corresponds with their absorption efficiency of around 80% for unpolarized light. The combination with 3D-printing can enable completely fiber-coupled and ultra-fast detectors with high detection efficiencies at any desired wavelength in the visible and near-IR spectral range, including the telecommunication bands.

We have also shown two different approaches to create scalable detector arrays: One single layer and one multi layer approach. Whereby the multilayer design can enable even large arrays, since the electrical contacts only scale with the square root of the detector number. In addition, these structures would inherit all the previous excellent properties of the detector structures which have been demonstrated before.

DEUTSCHE ZUSAMMENFASSUNG

Die Analyse und Detektion von Licht ist in verschiedenen Bereichen der Technik von entscheidender Bedeutung. Ein interessantes und spannendes Phänomen, das hier genutzt werden kann, ist die resonante Wechselwirkung von Licht mit metallischen Nanopartikeln. Diese sogenannten plasmonischen Resonanzen und die entsprechenden Nanostrukturen werden ständig in neuen technologischen Anwendungen genutzt, um verschiedene Technologien zu verbessern oder zu ermöglichen. In den meisten Fällen werden Edelmetalle aufgrund ihrer vorteilhaften optischen Eigenschaften verwendet. Aber auch andere Metalle, wie z. B. auf Niob basierende Stoffe wie Niob selbst, Niobnitrid und Niobtitannitrid, bieten hervorragende plasmonische Eigenschaften, wie wir in dieser Arbeit gezeigt haben und können daher für plasmonische Anwendungen genutzt werden. Noch wichtiger ist, dass diese Metalle auf Niob-Basis eine weitere interessante und nützliche Eigenschaft aufweisen, nämlich ihre Supraleitung.

Dieses supraleitende Verhalten kann genutzt werden, um supraleitende Nanodraht-Einzelphotonendetektoren herzustellen, die den Phasenübergang von supraleitend zu normalleitend ausnutzen, um sogar einzelne Photonen nachzuweisen. Sie ermöglichen eine hocheffiziente, präzise und schnelle Photodetektion, die für Quantenanwendungen erforderlich ist. In der Vergangenheit wurden Avalanche-Photodioden verwendet, die jedoch mit den neuen Entwicklungen und der erforderlichen Geschwindigkeit nicht mehr mithalten können. Die große Herausforderung mit den neuen supraleitenden Detektoren besteht darin, den Konflikt zwischen der Detektionseffizienz, die größere aktive Flächen erfordert, und der Geschwindigkeit, die kleine aktive Flächen erfordert, zu verringern, da die Erholungszeit mit der Induktivität und somit mit der Länge der Detektorstruktur korreliert.

Um dieses Problem zu lösen, wird der hohe Absorptionsquerschnitt plasmonischer Resonanzen ausgenutzt, indem das Prinzip des sogenannten plasmonischen perfekten Absorbers angewendet wird, um eine Absorption von nahezu 100% zu erreichen, selbst bei kleinen aktiven Flächen und auch im infraroten Spektralbereich. Wir haben Niob-basierte Nanodrahtarrays auf einem perfekten Absorbersubstrat simuliert, da sie die Grundlage der Detektorstrukturen bilden. Diese Simulationen haben hochabsorbierende,

breite und durchstimmbare Plasmonenresonanzen mit über 99% Absorption über einen breiten Spektralbereich ergeben. Dabei verschieben sich die plasmonischen Resonanzen aufgrund ihres Dipolcharakters bei größeren Drahtbreiten ins Rote. Die hergestellten Proben haben diese Ergebnisse bestätigt und Messungen haben eine Absorption von über 95% ergeben. Selbst die kleineren Detektorstrukturen mit einer aktiven Fläche von nur $30 \times 30\ \mu m^2$ weisen bei unserer Zielwellenlänge von 1140 nm eine maximale Absorption von etwa 90 - 95% auf. Der fertige Detektor war in der Lage, Laserleistungen von unter 1 µW in TM-Polarisation zu erfassen. Bei TE-Polarisation ist ein Minimum von ca. 2 µW erforderlich, was eine stärkere Absorption und damit eine höhere Detektionseffizienz für TM-polarisiertes Licht bestätigt, bei dem die Plasmonen angeregt werden. Dies führt zu einer polarisationsabhängigen Reaktion. Außerdem haben wir verschiedene polarisationsunabhängige Detektordesigns untersucht, die ein Absorptionsmaximum von etwa 90% aufweisen, und ihre Absorption und Reaktion auf eine externe Lichtquelle gemessen.

Nachdem wir die Funktionalität unserer Detektoren bestätigt haben, haben wir ultrakleine Detektoren mit einer aktiven Fläche von nur $3 \times 3\ \mu m^2$ hergestellt. Dazu haben wir 3D-gedruckte Glasfaseroptiken zur Fokussierung, Faserspannvorrichtungen zur Ausrichtung und die Winkelunabhängigkeit des plasmonischen Prinzips des perfekten Absorbers verwendet. Nach der Auswertung dieser Messungen konnten wir die Anzahl der ankommenden Photonen auf diesen Detektoren berechnen. Mit diesen Ergebnissen haben wir abgeschätzt, dass unsere Strukturen Pulse messen können, die im Durchschnitt nur einstellige Photonenzahlen enthalten. Dies ist ein wichtiger Schritt in Richtung Einzelphotonendetektion, denn es zeigt, dass bereits Pulse mit Photonenzahlen in der Größenordnung von Einzelphotonen eine Veränderung in unserem Detektor hervorrufen. Aufgrund des schlechten Signal-Rausch-Verhältnisses ist dies jedoch derzeit nicht ohne Lock-in möglich. Wir stekken fest, dass unsere Detektoren eine Detektionseffizienz von etwa 80% haben, was mit ihrer Absorptionseffizienz von etwa 80% für unpolarisiertes Licht übereinstimmt. Die Kombination mit 3D-Druck kann vollständig fasergekoppelte und ultraschnelle Detektoren mit hoher Detektionseffizienz bei jeder benötigten Wellenlänge im sichtbaren und nahen IR-Spektralbereich, einschließlich der Telekommunikationsbänder, ermöglichen.

Wir haben auch zwei verschiedene Ansätze zur Erstellung skalierbarer Detektorarrays gezeigt: Einen einlagigen und ein mehrlagigen Ansatz, wobei das mehrschichtige Design auch große Arrays ermöglicht, da die elektrischen Kontakte nur mit der Quadratwurzel der Detektoranzahl skalieren. Darüber hinaus würden diese Strukturen alle bisherigen hervorragenden Eigenschaften der zuvor gezeigten Detektorstrukturen erben.

CONTENTS

PUBLICATIONS

Parts of this thesis and associated work have been published in scientific journals, have been submitted to a journal, are being prepared for publication, and/or have been presented at national and international conferences.

JOURNAL PUBLICATIONS

P1 P. Karl, M. Ubl, M. Hentschel, P. Flad, Z.-Y. Chiao, J.-W. Yang, Y.-J. Lu, and H. Giessen
"**Optical properties of niobium nitride plasmonic nanoantennas for the near- and mid-infrared spectral range**",
Optical Materials Express **10**, 2597-2606 (2020),
DOI 10.1364/OME.403093.

P2 P. Karl, S. Mennle, M. Ubl, P. Flad, J.-W. Yang, T.-Y. Peng, Y.-J. Lu, and H. Giessen
"**Niobium nitride plasmonic perfect absorbers for tunable infrared superconducting nanowire photodetection**",
Optics Express **29**, 17087-17096 (2021),
DOI 10.1364/OE.424148.

P3 P. Karl, S. Mennle, M. Ubl, M. Hentschel, P. Flad, J.-W. Yang, T.-Y. Peng, Y.-J. Lu, and H. Giessen
"**Tunable infrared high absorbing polarization independent niobium nitride plasmonic perfect absorber nanowire photodetectors**",
Optical Materials Express **12**, 2453-2461 (2022),
DOI 10.1364/OME.458242.

P4 S. Mennle, P. Karl, M. Ubl, P. Ruchka, K. Weber, M. Hentschel, P. Flad, and H. Giessen
"**Towards fiber-coupled plasmonic perfect absorber superconducting nanowire photodetectors for the near- and mid-infrared**",
Optics Continuum **2**, 1901-1910 (2023),
DOI 10.1364/OPTCON.496334.

CONFERENCE CONTRIBUTIONS AS PRESENTING AUTHOR

C1 P. Karl, M. Ubl, M. Hentschel, P. Flad, A. Farag, J.-W. Yang, Y.-J. Lu, and H. Giessen
"**Superconducting NbN plasmonic perfect absorbers for tunable single photon near- and mid-IR photodetection**",
CLEO, All-Virtual (2021), Oral conference presentation.

C2 P. Karl, S. Mennle, M. Ubl, K. Weber, M. Hentschel, P. Flad, J.-W. Yang, Y.-J. Lu, and H. Giessen
"**Superconducting Nb-based plasmonic perfect absorbers for tunable near- and mid-IR photodetection**",
Fall Meeting of the German Physical Society (DPG), All-Virtual (2021), Oral conference presentation.

C3 P. Karl and H. Giessen
"**Tunable near and mid-infrared polarization-independent Niobium based plasmonic perfect absorber photodetectors**",
IQST Day 2022, All-Virtual (2022), Oral conference presentation.

C4 P. Karl, S. Mennle, M. Ubl, K. Weber, M. Hentschel, P. Flad, J.-W. Yang, T.-Y. Peng, Y.-J. Lu, and H. Giessen
"**Tunable superconducting Nb-based plasmonic perfect absorber photodetectors for the near- and mid-IR spectral range**",
PhD Conference of the Quantum Alliance, Munich, Germany (2022), Oral conference presentation.

C5 P. Karl, S. Mennle, M. Ubl, M. Hentschel, P. Flad, K. Weber, J.-W. Yang, T.-Y. Peng, Y.-J. Lu, and H. Giessen
"**Niobium-based plasmonics for photo detection**",
Annual IQST PhD Retreat 2022, Ulm, Germany (2022), Poster presentation.

C6 P. Karl, S. Mennle, M. Ubl, M. Hentschel, P. Flad, K. Weber, P. Ruchka, J.-W. Yang, T.-Y. Peng, Y.-J. Lu, and H. Giessen
"**Tunable Niobium-based Plasmonics for Photo Detection**",
IQST Day 2023, Ulm, Germany (2023), Poster conference presentation.

C7 P. Karl, S. Mennle, M. Ubl, K. Weber, P. Ruchka, M. Hentschel, P. Flad, and H. Giessen
"**Ultra-small superconducting Nb-based plasmonic perfect absorbers single mode fiber coupled photodetectors**",
Spring Meeting of the German Physical Society (DPG), Hannover, Germany (2023), Oral conference presentation.

C8 P. Karl, S. Mennle, M. Ubl, M. Hentschel, P. Flad, K. Weber, P. Ruchka, J.-W. Yang, T.-Y. Peng, Y.-J. Lu, and H. Giessen
"**Tunable, ultra-small and fiber-coupled niobium-based plasmonic photo detectors**",
Annual IQST PhD Retreat 2023, Ulm, Germany (2023), Poster presentation.

1

INTRODUCTION

Detecting and analyzing light is essential in several areas of technologies. One fascinating and interesting phenomena which could be utilized here is the resonant interaction of light with metallic nanoparticles. These so-called plasmonic resonances can be described as a collective oscillation of the free charge carriers in these metallic nanostructures and are achieved under matching conditions. The resonances depend on the optical material properties and the shape of the structures, which lead to a strong electrical field enhancement.

The field of plasmonic nanostructures is constantly expanding to new technological applications. It is already used to enhance, improve or enable various different technologies such as plasmonic-based solar cells [1], heat transfer systems [2], non linear optics [3, 4], different gas sensing detectors [5–7] and single photon detectors [8–10]. In most cases noble metals are used, due to their beneficial optical properties. However, other metals, such as Niobium-based materials like niobium (Nb) itself, niobium nitride (NbN) and niobium titanium nitride (NbTiN) [11, 12], also provide excellent plasmonic properties and can therefore be used for plasmonic applications. More important, these Nb-based metals exhibit an additional exciting and useful characteristic, namely they are superconductors.

This superconducting behavior can be used to fabricate superconducting nanowire single photon detectors (SNSPDs). SNSPDs consist of superconducting nanowires and utilize their superconducting to normal conducting phase transition to detect even single photons. They enable highly efficient, precise and fast photo detection, which is required for quantum applications, such as quantum key distribution [13], quantum cryptography [14, 15] and quantum computing [16, 17]. Avalanche photodiodes were used in the past, but they are not able to keep up with the new developments and required

speed. Furthermore, their quantum efficiency is strongly reduced in the IR spectral range.

The properties, such as the efficiency, of SNSPDs strongly depend on the used material and type of the detector, leading to a large variety of detectors. Most SNSPDs are using either the intrinsic absorption of the material or optical cavities [18, 19] to enable these single photon detection properties, leading to a decreased detection efficiency at higher wavelength and narrow resonances. In addition, there is always a trade-off between detection efficiency, which requires larger active areas and speed, which requires small active areas, since the recovery time of SNSPDs scales with the inductance of the detector structure.

We present one way to overcome this problems, by taking advantage of the high resonant absorbing cross-section of plasmonic resonances, which in addition, can be used to enhance the absorption, even in the infrared (IR) spectral range. This absorption enhancement can be further increased by utilizing the so-called plasmonic perfect absorber principle [20], to achieve up to 100% absorption over a wide spectral range.

These described properties can then be used to fabricate ultra-small and fast plasmonic enhanced SNSPDs. To couple the light efficiently to this small detectors, 3D-printed nanostructures are the optimal choice, since they enable a completely fiber-coupled system, featuring precise alignment with fiber chucks and small focal spots, due to 3D-printed micro lenses. Moreover, the use of these small micro lenses with large numerical apertures (NA) is possible due to the angle of incidence insensitivity of the perfect absorber principle. The combination of these three aspects allows us in the end to produce ultra-small detector structures with dimensions below the core diameter of optical fibers, which should enable completely fiber-coupled and ultra-fast SNSPDs with high detection efficiency at any desired wavelength in the visible and near-IR spectral range, including the telecommunication bands.

1.1 THESIS OUTLINE

This thesis starts with the theory of plasmonic systems, since it is the foundation of the used concepts, by explaining the interaction between light and matter in chapter 2. Hereby, we start with Maxwell's equations, followed by the Drude model, leading to the light interaction in metallic nanoparticles.

At the end of the chapter we will discuss the plasmonic perfect absorber principle and how it enhances the plasmonic absorption up to 100%.

In chapter 3 we discuss the fundamentals of superconductivity and SNSPDs, as well as their working principle and important properties.

Chapter 4 describes the fabrication of the studied samples. We utilize different techniques such as sputter and electron beam deposition, electron beam lithography and plasma etching to produce different precise and reproducible nanostructures. Moreover, we characterize the superconducting properties of our Nb-based films.

The plasmonic properties of NbN nanostructures are presented and discussed in chapter 5. We compare the permittivity of Nb and NbN with well known plasmonic materials and demonstrate their plasmonic properties by presenting transmission spectra of different NbN nanoantenna arrays.

Chapter 6 is about the Nb-based plasmonic superconducting photodetectors. We demonstrate the simulated and measured absorption of our perfect absorber nanostructures. Afterwards, we explain the detector design, confirm their working principle under low temperature conditions and present our cryogenic measurement setup. As our detectors exhibit a strong polarization-dependence, such as most typical SNSPDs, due to their meander structure, we also present polarisation insensitive detector structures for application which do not need or want this kind of property.

In chapter 7 we introduce the combination of our plasmonic photodetectors and 3D-nanoprinting applications, to create ulta small ($3 \times 3\ \mu m^2$) and hence ultra-fast detector structures. We also present the new measurement setup, which enables the measurements of these new samples, as well as time-dependent measurements. With this new setup we confirm that our plasmonic enhanced detectors can indeed measure single photons.

Chapter 8 is about pixelated superconducting photodetectors and our first designs and approaches to create scalable detector arrays.

A short summery of the most important results and concepts is given in chapter 9. Furthermore, it reveals a possible outlook and future possibilities with the introduced technology and concepts.

2

THEORY OF PLASMONIC SYSTEMS

In this chapter we will lay the foundation of the further work in this thesis by explaining the interaction between light and matter. First we focus on the basis, namely Maxwell's equations, followed by the Drude model, to understand the dynamics of conduction electrons, specifically in metals. With this groundwork, we are able to examine the consequences of this interaction with metallic nanoparticles, which enables us to discuss and understand plasmonic systems. Furthermore, we will show how to excite localized surface plasmon resonances in such nanostructures and close by demonstrating a way to enhance their absorption to almost 100%, with the so-called plasmonic perfect absorber principle.

The basic theory of electrodynamics and plasmonics is discussed in a variety of physic textbooks. This chapter follows the argumentation in [21] and [20].

2.1 BASIC EQUATIONS OF LIGHT-MATTER INTERACTIONS

The theoretical fundamentals of light and matter interaction are given by Maxwell's equations. In matter and SI-units they link the four macroscopic fields as followed:

$$\nabla \cdot \vec{D} = \rho_{\text{ext}} \tag{2.1}$$

$$\nabla \cdot \vec{B} = 0 \tag{2.2}$$

$$\nabla \times \vec{E} = -\frac{\partial}{\partial t}\vec{B} \tag{2.3}$$

$$\nabla \times \vec{H} = \frac{\partial}{\partial t}\vec{D} + \vec{J}_{\text{ext}}. \tag{2.4}$$

Whereby $\vec{E}$ is the electric field, $\vec{H}$ the magnetic field, $\vec{D}$ electric displacement field, $\vec{B}$ the magnetic flux density, ρ the charge and $\vec{J}$ the current density of

external charges. In matter polarization $\vec{P}$ and magnetization $\vec{M}$ further link the fields by:

$$\vec{D} = \epsilon_0 \epsilon \vec{E} = \epsilon_0 \vec{E} + \vec{P} \tag{2.5}$$

$$\vec{H} = \frac{1}{\mu_0 \mu} \vec{B} = \frac{1}{\mu_0} \vec{B} - \vec{M}. \tag{2.6}$$

The constants ϵ_0 and μ_0 are known as dielectric permittivity and dielectric permeability of the free space. Whereas ϵ and μ are the relative dielectric permittivity and relative dielectric permeability. They, however, fully depend on the material and characterize their electric and magnetic response. For most non-magnetic materials we approximate $\mu \approx 1$.

Another important relation connects $\vec{J}$ and $\vec{E}$ via the conductivity σ

$$\vec{J} = \sigma \vec{E}. \tag{2.7}$$

In general ϵ and σ are complex values and frequency dependent. Therefore, we can expressed them with ϵ_1, σ_1 and ϵ_2, σ_2 as their real and imaginary parts:

$$\epsilon(\omega) = \epsilon_1(\omega) + \mathrm{i}\epsilon_2(\omega) \tag{2.8}$$

$$\sigma(\omega) = \sigma_1(\omega) + \mathrm{i}\sigma_2(\omega) \tag{2.9}$$

There is a significant relationship between $\epsilon(\omega)$ and $\sigma(\omega)$, which enables us to describe electromagnetic phenomena in metals with either quantity

$$\epsilon(\omega) = 1 + \frac{\mathrm{i}\sigma(\omega)}{\epsilon_0 \omega}. \tag{2.10}$$

One way to determine $\epsilon(\omega)$ is via the measurement of the complex refractive index $\tilde{n}(\omega) = n(\omega) + \mathrm{i}\kappa(\omega)$ and the relation:

$$\tilde{n} = \sqrt{\epsilon(\omega)\mu(\omega)} \tag{2.11}$$

With $\mu \approx 1$ (2.11) reduces to $\tilde{n} = \sqrt{\epsilon(\omega)}$.

With the following relation for the speed of light in vacuum c

$$c = \frac{1}{\sqrt{\mu_0 \epsilon_0}}, \tag{2.12}$$

a plane wave ansatz with the wave vector $\vec{k}$ and by studying the traveling-wave solution of Maxwell's equations without external influences, through

combining equation (2.3) and (2.4), we are able to receive the wave equations and their solutions:

$$\nabla \times \nabla \times \vec{E} = -\mu_0 \frac{\partial^2 \vec{D}}{\partial t^2} \tag{2.13}$$

$$\vec{k}(\vec{k} \cdot \vec{E}) - \vec{k}^2 \cdot \vec{E} = -\epsilon \cdot \frac{\omega^2}{c^2} \vec{E}. \tag{2.14}$$

Leading to the general dispersion relation for transverse waves $\vec{k} \cdot \vec{E} = 0$:

$$k^2 = \epsilon \frac{\omega^2}{c^2} \tag{2.15}$$

and yields for longitudinal waves, that collective oscillations are only possible at frequencies with $\epsilon = 0$.

2.2 CONDUCTION ELECTRONS IN METALS

To describe the optical properties of metals, the Drude model is used. In 1900 the Drude model was invented by Paul Drude [22]. It describes the general electrodynamic properties of metals, although it is based on classical physics, the main result is valid even by considering quantum mechanics.

The general idea of the Drude model is an application of kinetic theory. It assumes that the electric conductivity is caused by free charge carriers, called conduction electrons, which move relative to a fixed positively charged background. After an average relaxation time τ they will scatter with the background, whereby the movement after collision is temperature-dependent and occurs in a random direction.

For the static system the electrons are accelerated in a fixed external electric field, until they scatter with the background after the time τ. This results in a velocity of:

$$\vec{v} = -\frac{e\vec{E}\tau}{m}, \tag{2.16}$$

where m is the mass of the electrons and e its charge. The current density is then given by:

$$\vec{J} = -Ne\vec{v} = \frac{Ne^2\vec{E}\tau}{m}, \tag{2.17}$$

where N is the concentration of the electrons. By comparison with Ohm's law (2.7) the DC conductivity σ_0 can be identified as:

$$\sigma_0 = \frac{Ne^2\tau}{m} \tag{2.18}$$

2.2.1 *Frequency-dependent properties*

To obtain the frequency-dependent dynamics we apply an equation of motion with a time-dependent external electric field and a characteristic collision time $\gamma = 1/\tau$:

$$m\frac{\mathrm{d}^2}{\mathrm{d}t^2}\vec{x} + m\gamma\frac{\mathrm{d}}{\mathrm{d}t}\vec{x} = -e\vec{E}(t). \tag{2.19}$$

By assuming an external harmonic oscillating electric field as driving force and the following ansatz:

$$\vec{E}(t) = \vec{E}_0 \cdot \mathrm{e}^{-\mathrm{i}\omega t}$$
$$\vec{x}(t) = \vec{x}_0 \cdot \mathrm{e}^{-\mathrm{i}\omega t}$$

we receive

$$\vec{x}(t) = \frac{e}{m(\omega^2 + \mathrm{i}\gamma\omega)}\vec{E}(t) \tag{2.20}$$

as possible solution for $\vec{x}(t)$. Due to the displacement of the electrons, they are contributing to the macroscopic polarization $\vec{P} = -Ne\vec{x}$:

$$\vec{P} = -\frac{Ne}{m(\omega^2 + \mathrm{i}\gamma\omega)}\vec{E}(t), \tag{2.21}$$

and by inserting this equation in (2.5) we obtain

$$\vec{D} = \epsilon_0\left(1 - \frac{\omega_\mathrm{p}^2}{\omega^2 + \mathrm{i}\gamma\omega}\right)\vec{E}(t), \tag{2.22}$$

with the plasma frequency

$$\omega_\mathrm{p}^2 = \frac{Ne^2}{\epsilon_0 m} \tag{2.23}$$

of the material. The comparison of $\vec{D}$ with (2.5) yields to the dielectric function of our free electron

$$\epsilon(\omega) = 1 - \frac{\omega_\mathrm{p}^2}{\omega^2 + \mathrm{i}\gamma\omega}. \tag{2.24}$$

We are now able to separate the complex function $\epsilon(\omega) = \epsilon_1(\omega) + i\epsilon_2(\omega)$ in its real and imaginary part:

$$\epsilon_1(\omega) = 1 - \frac{\omega_p^2 \tau^2}{1 + \omega^2 \tau^2} \qquad \epsilon_2(\omega) = \frac{\omega_p^2 \tau}{\omega(1 + \omega^2 \tau^2)}. \tag{2.25}$$

These results enable the calculation of the relation of a complex refractive index $\tilde{n}(\omega)$ and following relations by using (2.11):

$$\tilde{n}(\omega) = n(\omega) + i\kappa(\omega), \tag{2.26}$$

$$\epsilon_1 = n^2 - \kappa^2 \qquad \epsilon_2 = 2n\kappa, \tag{2.27}$$

with its real part n and imaginary part κ.

2.3 PLASMONIC RESONANCES

In this section we explore the interaction of external light at interfaces and sub-wavelength nanostructures. The plasmon represents hereby a collective excitation of our free conduction electrons.

2.3.1 *Surface plasmons*

Surface plasmons polaritons (SPPs) are a special kind of plasmons. These plasmons are propagating as an electromagnetic wave at a dielectric-metal interface, whereby their perpendicular components decay exponentially. The source of these plasmons are electromagnetic fields, which are coupling to the oscillations of the conduction electrons in the metal.

In the last section we have identified the wave equation, and by neglecting the variation of the dielectric permittivity ϵ for distances shorter than a wavelength, we can simplify (2.13) to obtain

$$\nabla^2 \vec{E} - \frac{\epsilon}{c^2} \frac{\partial^2 \vec{E}}{\partial t^2} = 0. \tag{2.28}$$

With the ansatz of a general harmonic time-dependent electrical field this equation yields

$$\nabla^2 \vec{E} + k_0^2 \epsilon \vec{E} = 0, \tag{2.29}$$

with the wave vector in vacuum $k_0 = \frac{\omega}{c}$ and is called Helmholz equation.

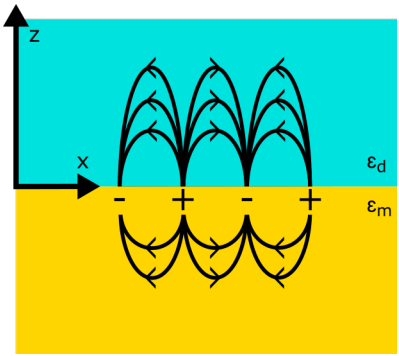

Figure 2.1: Schematic sketch of a SSP propagations at a dielectric-metal interface and its corresponding electric field lines. We note a strong field enhancement and a surface charge wave.

Figure 2.1 depicts the electric field of such a SPP. We notice a strong electrical field enhancement directly at the dielectric-metal interface, represented by the density of the electrical field lines. The complete and detailed calculation of the x- and z-part of the displayed electrical field can be found in a variety of books, such as [21]. These results hold only for TM (transverse-magnetic) surface modes, TE (transverse-electric) modes are not possible, due to the fact that their only possible solution yields an amplitude of zero.

The continuity at the interface implies following dispersion relation between the wave vector k_x of our plasmon wave and the frequency ω:

$$k_x = \frac{\omega}{c}\sqrt{\frac{\epsilon_\mathrm{d}\epsilon_\mathrm{m}}{\epsilon_\mathrm{d}+\epsilon_\mathrm{m}}}, \tag{2.30}$$

with the permittivity of the dielectric ϵ_d and the permittivity of the metal ϵ_m.

In figure 2.2 we display the real part of (2.30) for an air-metal interface, whereby the frequency is normalized to the plasma frequency.

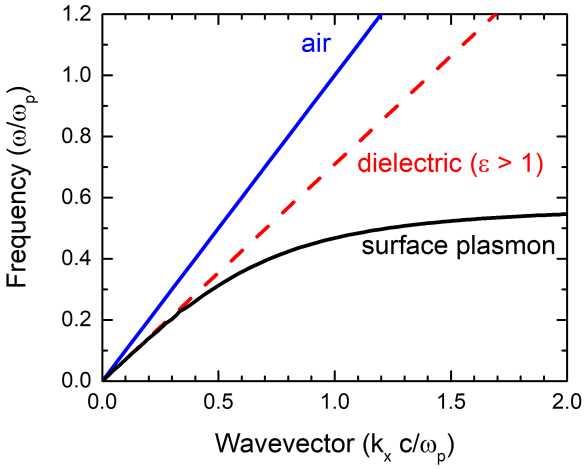

Figure 2.2: Dispersion relation of surface plasmons (black) compared to air (blue) and a dielectric medium (red) with an $\epsilon > 1$.

By taking a closer look at this relation in figure 2.2 we notice, that the dispersion curve of the excited plasmons lies to the right of the corresponding light lines. Hence, we need to phase-match these relations by using special techniques, such as gratings or prism coupling.

2.3.2 *Localized surface plasmons*

In the last section we have investigated SPPs, which are propagating electromagnetic waves of free electrons in a metal. In contrast to them, we introduce now non-propagating excitations, so-called localized surface plasmons (LSPs). These excitations occur in metallic sub-wavelength nanostructures, which are coupled to an electromagnetic field. LSPs can be exited without special phase-matching techniques, while maintaining the large field enhancement of SPPs.

For simple and symmetric systems this problem can be solved analytically, by using the simple quasi-static approximation. Whereby the size d of the structure is considered much smaller than the wavelength of the exciting light $d \ll \lambda$, leading to an constant external electromagnetic field over the whole structure at the same moment. This enables us to calculate the prob-

lem by utilizing an electrostatic field and the harmonic time-dependence can be added later.

Let us assume a homogeneous metallic nano-sphere with radius a and permittivity ϵ_m, placed at the origin of our electrostatic field $\vec{E}_0$, located in a non-absorbing surrounding dielectric medium with ϵ_d, see figure 2.3

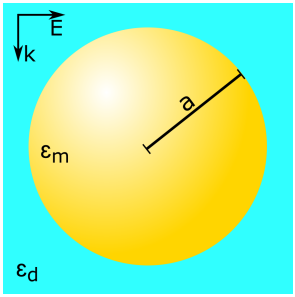

Figure 2.3: Schematic sketch of a metallic nano-sphere with radius a and ϵ_m, placed at the origin of an electrostatic field $\vec{E}_0$, located in a non-absorbing surrounding dielectric medium with ϵ_d.

We use spherical coordinates to describe the problem and due to the static approach we are investigating solutions of the Laplace equation of our potential and its corresponding electrical field. The general solution of our symmetric problem is given by the Legendre Polynomials. A detailed calculation and type of the potential and field can be found in [21].

We are able to find a dipole moment $\vec{p}$ in the resulting resonance on the basis of the collectively oscillating free electrons in the metallic sphere and their stationary positive background

$$\vec{p} = 4\pi\epsilon_0\epsilon_d a^3 \frac{\epsilon_m - \epsilon_d}{\epsilon_m + 2\epsilon_d}\vec{E}_0. \tag{2.31}$$

With the polarizability

$$\alpha = 4\pi a^3 \frac{\epsilon_m - \epsilon_d}{\epsilon_m + 2\epsilon_d}, \tag{2.32}$$

we can identify with $\vec{p} = \epsilon_0\epsilon_d\alpha\vec{E}_0$. We notice the maximum of the dipole moment is reached, when $|\epsilon_m + 2\epsilon_d|$ is a minimum. In metals we assume small losses $\Im(\epsilon_m) \approx 0$, so the resonance reduces to

$$\Re(\epsilon_m) = -2\epsilon_d. \tag{2.33}$$

With the permittivity ϵ extracted from the Drude model, we are able to derive the resonance frequency ω_{LSP} for our metallic sphere

$$\omega_{\mathrm{LSP}} = \frac{\omega_{\mathrm{p}}}{\sqrt{1+2\epsilon_{\mathrm{d}}}}. \tag{2.34}$$

The electric fields inside and outside of our nano-sphere, which are based on our potential, can be calculated and yield

$$\vec{E}_{\mathrm{in}} = \frac{3\epsilon_{\mathrm{m}}}{\epsilon_{\mathrm{m}}+2\epsilon_{\mathrm{d}}}\vec{E}_0 \qquad \vec{E}_{\mathrm{out}} = \vec{E}_0 + \frac{3\vec{n}(\vec{n}\cdot\vec{p})-\vec{p}}{4\pi\epsilon_0\epsilon_{\mathrm{d}}}\frac{1}{r^3}, \tag{2.35}$$

with the unit vector $\vec{n}$ in the direction of the point of interest.

LSPs structures are already used in plenty of applications [6, 23, 24]. Their high resonant absorption cross section enables high detection efficiency, even with small active areas. In addition, the absorption can be further increased by using perfect absorber geometries.

2.3.3 *Plasmonic perfect absorber principle*

In this section we investigate the plasmonic perfect absorber principle [20], which enhances the absorption of our plasmon resonances close to unity. This is especially important for applications in the near- and mid-infrared spectral range, due to the strong reflectivity and weak absorbance of metals in this regime.

To understand the mechanics behind the perfect absorber principle we look at figure 2.4. We notice the perfect absorber consists of a stack of different thin films. On top we have the plasmonic material, this is followed by a dielectric spacer and on the bottom we attach a metallic mirror. In our case the mirror consists of gold (Au), which is basically a perfect mirror in the IR spectral range, for visible wavelengths a silver mirror can be more suitable.

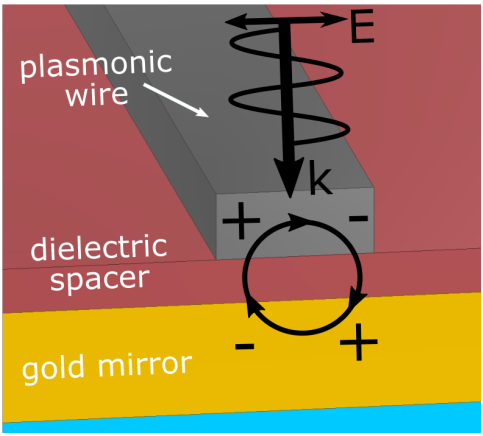

Figure 2.4: Working principle of the plamonic perfect absorber substrate. The incoming light starts a plasmon oscillation in the plasmonic nanowire, which creates an antiphase mirror plasmon in the gold mirror below. Their interaction can be seen as a circulating current, and thus a magnetic response is generated. This magnetic response can interact with the magnetic field of the incident light and hereby enhances the absorption.

We are able to describe the structure with a simple mathematical model to explain its working principle. Hereby we assume our structure is a medium with a magnetic permeability $\mu(\lambda)$ and an electric permittivity $\epsilon(\lambda)$. The first step to reach unity absorbance is to suppress the reflectance R. This can be achieved by matching the optical impedance of our structure $Z_s = \sqrt{\mu/\epsilon}$ and the vacuum impedance $Z_v = 1$, due to

$$R = \left| \frac{Z_v - Z_s}{Z_v + Z_s} \right|^2 . \tag{2.36}$$

The impedance matching is realized by adjusting the geometry of our plasmonic structure on top, as well as the spacer thickness. The second step is to block the transmission T of our sample. This is handled by the thick metallic mirror at the bottom of the structure. The combination of the suppressed reflectance and blocked transmission leads to an unity absorbance $A = 1 - R - T = 1$. However, this holds only for a specific wavelength region.

An alternative phenomenological explanation can be imagined as followed. Perpendicular polarized light, as shown in figure 2.4, excites LSPs in the plasmonic nanostructure. The oscillation of this plasmons leads to the

excitation of an antiphase mirror plasmon of the free electrons in the metallic mirror. The interaction between this two plasmons can be interpreted as a circular current flow, leading to a magnetic response. The magnetic field of the incoming light interacts with the magnetic response, increasing the absorption.

Perfect plasmonic absorbers are useful in a variety of different plasmonic sensing application, to enhance the absorption and hence the performance of these detectors [5, 25].

An additional important feature of the plasmonic perfect absorber is its strong incident angle independence [5, 25], allowing the use of high-NA objectives to reach smaller active areas, without loosing detection efficiency, unlike cavity approaches.

3

SUPERCONDUCTION NANOWIRE SINGLE PHOTON DETECTORS

In this chapter we will briefly discuss the fundamentals of superconductivity and its importance for SNSPDs. In addition, the working principle and significant properties of SNSPDs will be listed and explained, whereby we use [26] as foundation and orientation.

SNSPDs consist of superconducting nanowires and are utilizing their superconducting to normal conducting phase transition. They enable highly efficient, precise and fast photodetection, which is required for quantum applications, such as quantum key distribution [13], quantum cryptography [14, 15] and quantum computing [16, 17]. Avalanche photodiodes were used in the past, but are not able to keep up with the new developments and required speed, furthermore, their quantum efficiency is strongly reduced in the IR spectral range, due to the low intrinsic absorption of their materials. The new choice are SNSPDs due to their superior properties.

The efficiency and other properties of SNSPDs strongly depend on the used material and type of the detector, leading to a large variety of detectors. Typical material are NbN [18, 27, 28], NbTiN [29–31], tungsten silicide [32], molybdenum silicide [33] and other superconducting metals. To ensure a high quantum efficiency, different approches are used, such as optical nanoantennas [34, 35], waveguides [36], optical cavities [18, 19] and plasmonic structures [26, 37].

3.1 SUPERCONDUCTIVITY

3.1.1 *Phenomenology*

In 1908 Onnes was able to liquefy helium [38, 39]. This has opened up the field of low temperatures physics. In 1911 he has measured the resistance of a mercury sample during a cool down process. The result is displayed in figure 3.1. We notice a jump in the resistance and a not measurable resistance value after reaching a certain temperature, which we call critical temperature T_c.

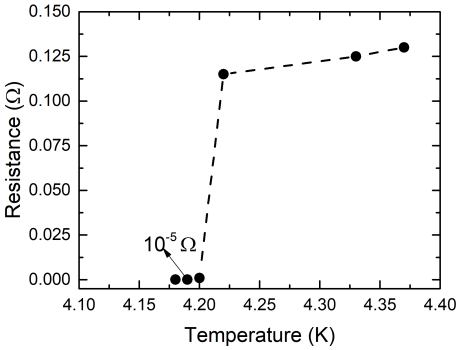

Figure 3.1: Superconducting transition of mercury measured by Heike Kamerlingh Onnes in 1911 [39].

Thanks to this, Walther Meissner and Robert Ochsenfeld were able to make another big discovery in 1933. They discovered that superconductors prevent a penetration of an external magnetic field, due to the formation of so-called screening currents [40]. This effect is called the Meissner–Ochsenfeld effect. Furthermore, the superconducting behavior breaks at a certain external magnetic field, which implies the existence of a critical magnetic field as well as a critical current. With the following theories we give a short overview to explain these behaviors.

3.1.2 *London thoery*

In 1935 Fritz and Heinz London explained the vanishing resistance and the Meissner-Ochsenfeld effect with a theory based on the Drude model as followed [41]

$$m\frac{\mathrm{d}\vec{r}}{\mathrm{d}t^2} + \frac{m}{\tau}\frac{\mathrm{d}\vec{r}}{\mathrm{d}t} = -e\vec{E}(t). \tag{3.1}$$

With $\vec{J} = N_s e\vec{v} = N_s e\frac{\mathrm{d}\vec{r}}{\mathrm{d}t}$, it leads to

$$\frac{m}{N_s e}\frac{\mathrm{d}\vec{J}}{\mathrm{d}t} + \frac{m}{\tau N_s e}\vec{J} = e\vec{E}(t). \tag{3.2}$$

Using $\lim_{\tau\to\infty}$, for representing the electrical transport with no resistance, we will end up with the first London equation:

$$\frac{\mathrm{d}\vec{J}(t)}{\mathrm{d}t} = \frac{N_s e^2}{m}\vec{E}(t). \tag{3.3}$$

The second London equation can be obtained be utilizing the third Maxwell equation (2.3):

$$\nabla \times \vec{J}(t) = -\frac{N_s e^2}{m}\vec{B}(t). \tag{3.4}$$

The fourth Maxwell equation (2.4) will yield a differential equation for the magnetic field:

$$\Delta\vec{B} = \frac{\mu_0 N_s e^2}{m}\vec{B} =: \frac{1}{\lambda_\mathrm{L}^2}\vec{B}, \tag{3.5}$$

which leads to the London penetration depth λ_L:

$$\lambda_\mathrm{L} = \sqrt{m/(\mu_0 N_s e^2)}. \tag{3.6}$$

3.1.3 *BCS theory*

The BCS theory was developed by Bardeen, Cooper and Schrieffer and represents the first microscopic theory of superconductors [42].

Two electrons at temperatures below T_c and above the Fermi energy E_F will form a Cooper pair, due to energy minimization. The emerging particles are handled as quasiparticles with an integer spin and the charge $2e$. They exhibit a bosonic nature. Therefore, they do not have to follow the Pauli principle, and thus can occupy the same ground state. This enables lossless charge transport, due to the fact that they are no longer affected by impurities or atomic nuclei, thanks to their overall Bose-Einstein wave function.

Cooper pairs exhibit an energy gap Δ, which can be calculated a followed [43]:

$$2\Delta_0 = 2\Delta(T = 0\ \mathrm{K}) = 3.53 k_\mathrm{B} T_\mathrm{c} \tag{3.7}$$

and for higher temperatures:

$$\frac{\Delta(T)}{\Delta(T=0)} = 1.74\sqrt{1 - \frac{T}{T_\mathrm{c}}}. \tag{3.8}$$

3.2 WORKING PRINCIPLE OF SNSPDS

SNSPDs are utilizing the superconducting to normal conducting phase transition to detect single photons. By measuring the resistance of the detector we are able to observe a voltage drop caused by arriving photons. The detector is cooled below its critical temperature with a cryostat and a bias current is applied. This current is slightly below the critical current density of our system [26].

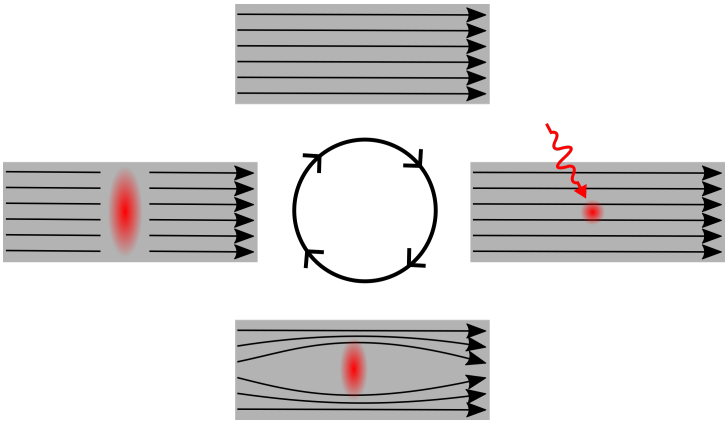

Figure 3.2: Schematic sketch of the working principle of SNSPDs. The absorbed photons cause a hot spot in the nanowire, leading to a small resistance increase. The bias current will avoid this region, creating a higher current density in the surrounding area. The increased current density will surpass the critical current density, which switches the structure to its normal conducting state.

The absorbed photons are now causing a hot spot in the plasmonic nanowire by disturbance and heating of cooper pairs, leading to a small

resistance increase in the hot spot area. Due to this higher resistance the bias current will avoid this region, creating a higher current density in the surrounding area. The increased bias current density will surpass the superconducting critical current density, which switches our detector to its normal conducting state, resulting in a measurable detector resistance. After a certain time the detector will cool down again and is ready to detect the next photons. A schematic sketch is depicted in figure 3.2.

This triggered transition is more likely to happen in thinner films, since the current has less space to avoid the hotspot area. For this reason SNSPDs require thin films.

3.3 PROPERTIES OF SNSPDS

As all detectors, SNSPDs have different important properties to characterize their performance. These will be described in the following sections, which is based on [26].

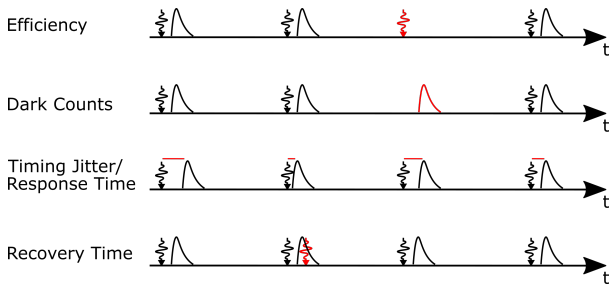

Figure 3.3: Important properties to characterize the performance of photodetectors. Efficiency: How many of the incoming photons are detected. Dark Counts: Counts without a photon incidence. Response time: Time between the arrival of the photon and its detection. Recovery time: Dead time of the detector.

3.3.1 *Detection efficiency*

The detection efficiency characterizes how many of the incoming photons are detected. It is also described as the quantum efficiency of the detector. It consists of two different parts, first the absorption efficiency η_a, which gives

us the probability for the absorption of an incoming photon. The second part is the read-out efficiency η_r, giving us the likelihood to detect the absorbed photon as an electric signal, which we call a count. The overall detection efficiency η can written as

$$\eta = \eta_a \cdot \eta_r. \tag{3.9}$$

The advantage of our approach is to enhance η_a up to 100%, and hence to obtain high and broadband detection efficiencies, even in the infrared spectral range. Conventional SNSPDs are struggling to reach high detection efficiencies in this regime, due to the metallic behavior of the material and the need to rely on narrowband cavities, for example [18, 44]. With these techniques SNSPDs can reach 80% or even higher quantum efficiencies, but only at narrow and specific wavelengths.

3.3.2 *Dark Counts*

Sometimes the detector indicates the arrival of a photon, even without an actual photon hitting the detector. This is due to an accidental breaking of the superconductivity, caused by structural or material imperfections, as well as temperature fluctuations. Dark counts are more likely to appear with a higher applied bias current, however the detection efficiency also increases with higher bias currents, due to more sensitive and simpler breaking of the superconductivity. One way to reduce dark counts is to use smaller, shorter and thinner detector wires, as there is less space for imperfections and in addition a smaller bias current is required. State-of-the-art SNSPDs exhibit low noise with milli-hertz dark count rates [44].

3.3.3 *Timing jitter*

Before we talk about the timing jitter we have to discuss the response time of our detectors. The response time tells us how much time has passed between the arrival of the photon and its detection, which takes for example the travelling time of the electrical signal into account. The timing jitter informs us about the variation of the response time, is a statistical value and limits the timing resolution of the detectors. For state-of-the-art SNSPDs the timing jitter lies in the picoseconds regime [44].

3.3.4 *Recovery time*

If we have a closer look at the working principle of our SNSPDs we realize that there is a dead time of our detector after successfully detecting a photon, due to the fact that the structure has to switch back to its superconducting state. The recovery time τ_{re} limits the detection speed of SNSPDs and is dependent on the kinetic inductance L_{k} of the detectors

$$L_k = \alpha \frac{l}{d \cdot w} \tag{3.10}$$

$$\tau_{\mathrm{re}} \approx \frac{L_{\mathrm{k}}}{Z_{\mathrm{load}}}, \tag{3.11}$$

with the length l, the width w and the thickness d of the superconducting wire. α represents a material-specific constant and Z_{load} is the impedance of the load, typically 50 Ω. State-of-the-art recovery times are in the low nanosecond regime [45, 46]. By utilizing the high resonant cross section of plasmons we are able the produce high absorbing detectors with small active areas and hence short recovery times.

4

FABRICATION OF THE STUDIED SAMPLES

To achieve the best superconducting and optical properties for our films and structures, we need high quality films, as well as precisely defined nanostructures. In this chapter we discuss the fabrication of our superconducting films and their perfect absorber substrate, via electron beam and sputter depositions and afterwards the structuring into precise nanostructures, by using electron beam lithography (EBL) and plasma etching techniques. The fabrication methods for the different studied samples can also be found in our different papers [12, 47, 48].

4.1 THIN FILM PRODUCTION

4.1.1 *Perfect absorber substrate*

The perfect absorber substrate consists of any substrate at the bottom, in our case these are thin, high quality polished 1×1 cm^2 glass or silicon plates. The glass is used for the NbN samples, due to the fact, that the substrate is pre-heated before the NbN sputtering and glass does not melt or evaporate particles even at high temperatures of around 800 °C. For samples with lower deposition temperatures a silicon substrate can also be used.

The perfect absorber substrate consists as described of two parts, a metallic mirror at the bottom, followed by a dielectric spacer on top. In our case we use a 120 nm thick Au mirror, which acts as an almost perfect mirror in the IR range. The whole substrate is evaporated with an electron gun to obtain a clean and smooth surface, unless explicitly stated otherwise. First the surfaces of the glass/silicon plates are carefully cleaned with acetone and isopropyl alcohol. To ensure our substrate sticks to the plates a 5 nm thick titanium sticking layer is evaporated before the Au mirror. On top of the gold mirror is the dielectric spacer, which consists of aluminum oxide (Al_2O_3), its

thickness depends on the material and the target wavelength. For Nb with a target wavelength of around 1100 nm a 70 nm thick spacer is used. For NbN at the same wavelength we used 100 nm Al_2O_3, but this time evaporate via atomic layer deposition to enhance superconducting properties of the NbN film, because it allows for a more orderly deposition of the molecules and comes closer to the structure of silicon, than the more chaotic e-gun evaporation. The thickness of our dielectric spacer is hereby determined in advance with simulations.

4.1.2 *Niobium films*

The 50 nm thick Nb film are sputtered in-house onto the perfect absorber substrates. We are using a Nb sputtering target with the following sputtering parameters: Deposition temperature: room temperature, chamber pressure: $\approx 5 \times 10^{-8}$ mbar, argon flow rate: 25 sccm, sputter power 530 W. It is important to notice that to fabricate good quality Nb films we need good quality perfect absorber substrates.

With these parameters we fabricate films with a critical temperature of around 4.5 K, which is high enough for our cryostat, so we are able to perform tests and proof of concepts with the in-house Nb samples, before using the NbN films, which are made in Taiwan. The critical temperature is measured with a superconducting quantum interference device (SQUID), which measures the magnetic moment, and hence we are able to identify the superconducting transition of our samples as shown in figure 4.1.

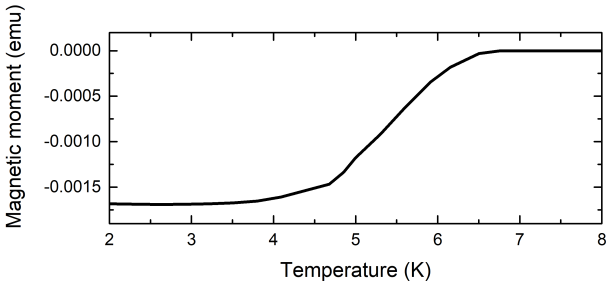

Figure 4.1: SQUID measurement of our 50 nm thick Nb sample, which shows a critical temperature of around 4.5 K.

On closer inspection of the measured superconducting behavior in figure 4.1, we notice a wide transition temperature range for the 50 nm thick

Nb films. This could indicate a slight contamination or light porous structure. Since the Nb is sputtered with the high power of 530 W, to prevent contamination caused by the not perfect vacuum, a porous structure is more likely. Ideally the Nb would be sputtered in an ultra-high vacuum with a slow sputter rate. These facts lead us to use 50 nm thick Nb for our experiments, because thinner films are not completely superconducting any more.

4.1.3 *Niobium nitride films*

The 20 nm thick NbN films have been sputter-deposited onto the prepared perfect absorber substrates by our collaborators in Taiwan from the Yu-Jung Lu group. They were using a radio-frequency magnetron sputtering system, together with a NbN sputter target and the following process parameters: Deposition temperature: 800°C, chamber pressure: $< 6 \times 10^{-8}$ torr, nitrogen/argon flow rate ratio: 1/24, sputter power 120 W. With these parameters we ensured the highest possible critical temperature for our thin NbN films.

The critical temperature of these 20 nm thick films are around 11 K, as depicted in the following figure 4.2 and was determinate via a SQUID measurement.

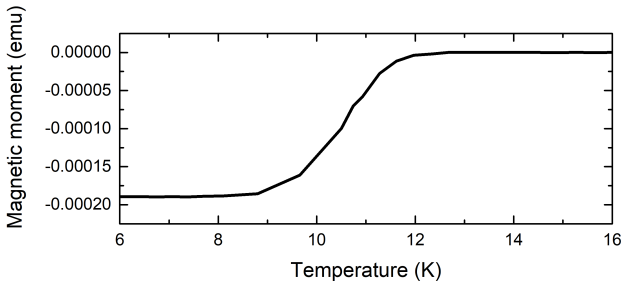

Figure 4.2: SQUID measurement of our 20 nm thick NbN sample, which shows a critical temperature of around 11 K.

Considering the critical temperature of bulk NbN with T_c = 16.5 K, a critical temperature of 11 K is a good achievement for thin films, due to the fact that values of thin films are lower than bulk values [49, 50].

However, it also shows a relative broad transition, leading to the idea that here are also some impurities in the NbN film.

4.1.4 *Niobium titanium nitride*

The 10 nm thick NbTiN films have been deposited onto the prepared perfect absorber substrates by our collaborators in Munich from the Kai Mueller group. Unlike the previous samples, these have a dielectric spacer made of Silicon dioxide (SiO_2).

4.2 NANOFABRICATION

To achieve the needed precision and reproducibility for our nanostructures we are using EBL and plasma etching. This process is depicted in figure 4.3.

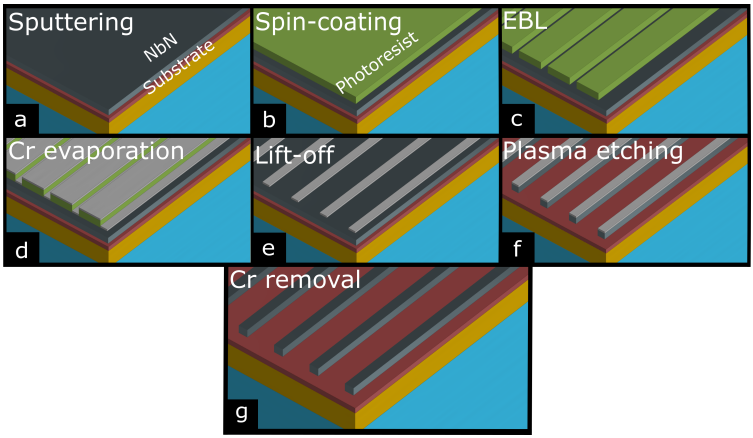

Figure 4.3: Schematic sketch of our nanofabrication process. a) Sputter the plasmonic material on the perfect absorber substrate. b) Spin-coating a high resolution positive photoresist on top. c) Electron beam pattering creates an inverse pattern of our nanostructure. d) Cr is evaporated. e) Cr etching mask is created with a lift-off. f) Plasma etching of the uncovered plasmonic material. g) Cr removal and finished plasmonic nanostructure.

First we spin-coated a high resolution positive photoresist on our samples. For the first structures including the NbN nanoantennas we have used 200R and 950K Polymethyl methacrylate and for the investigated plamonic lattices and detectors we have used AR-P 6200.04 (CSAR62). In addition we applied an Espacer for easier handling during the EBL process. With electron beam pattering we write an inverse pattern of our desired nanostructure into the photoresist, which is created after the development process. Afterwards we evaporate 50 nm chromium (Cr) via e-gun evaporation and obtain a Cr

etching mask after the lift-off process, with a n-ethyl-2-pyrrolidon based remover. Due to the Cr etching mask we are able to etch the undesired Nb/NbN away with plasma etching. After removing the remaining Cr mask with a Cr remover we have fabricated highly precise nanostructures on top of a perfect absorber substrate.

The additional advantage of this fabrication method is its flexibility, because we can easily adjust for example the period or wire width of our structures, which allows us to tune our plasmonic resonance to different target wavelengths, which is a desired feature for detectors [5, 51].

5

PLASMONIC PROPERTIES OF NB-BASED NANOSTRUCTURES

In this chapter we discuss the plasmonic properties of Nb-based, mostly NbN, nanostructures and want to introduce them as plasmonic material. We compare the permittivity of Nb and NbN with well known plasmonic materials and demonstrate their plasmonic properties by presenting transmission spectra of different NbN nanoantenna arrays on magnesium oxide (MgO), as well as their temperature stability. This chapter is based on our own publication [12].

As mentioned in the introduction, the field and areas of application of plasmonic nanostructures are constantly expanding. They are already used to enhance, improve or enable various different technologies such as plasmonic based solar cells [1], heat transfer systems [2], non linear optics [3, 4], different gas sensing detectors [5–7] and single photon detectors [8–10].

In most cases, the mentioned application use silver [52] and Au [53] nanostructures, due to their beneficial optical properties. However, less noble metals can also exhibit good plasmonic resonances, including Nb [11] and NbN [12], as we have demonstrated in the mentioned publications.

5.1 OPTICAL PROPERTIES OF THIN NB-BASED FILMS

To enable photons the opportunity to interact with a material, the frequency of the incoming photons has to be below its plasma frequency. For higher frequencies the material is too slow to respond to the light and becomes transparent. In addition, to allow plasmonic interaction a negative real part of the dielectric function is required [54].

In figure 5.1 we compare the complex permittivity of NbN with Au, Titanium nitride (TiN) [55] and Nb [11], three already established plasmonic materials. We identify a negative real part of the permittivity for Au, TiN and also for Nb and NbN [12, 56–58]. By comparing the NbN with the other materials we notice that the absolute value of the real part of ϵ_1 is lower compared to Au, TiN and Nb, due to being a less noble metallic material. Nevertheless, it fulfils the necessary requirements for plasmonic interactions.

The comparison of the imaginary part of the permittivity reveals, that it is highest in NbN, and hence it has more losses compared to the other three materials, again due to being a less noble metal. This will lead to broad resonances, which we can later use to create broadband detectors. Moreover, the higher losses will help to create more efficient detectors, due to the stronger intrinsic absorption of the material. Additionally, NbN could be used for other application [59], such as loss induced heat applications [60].

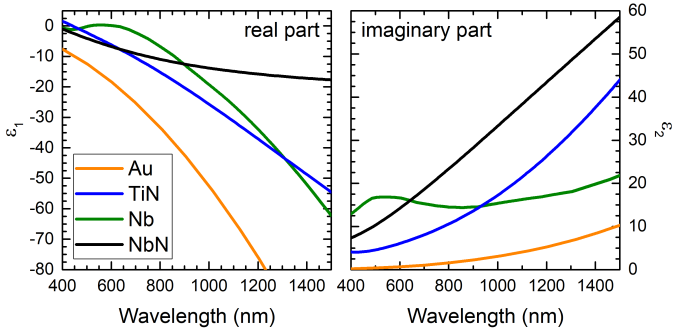

Figure 5.1: Permittivity of Nb and NbN in comparison with Au and TiN. The left and right graphs show the real and imaginary part of the dielectric function [11, 12, 61].

5.2 TRANSMISSION SPECTRA OF NBN NANOANTENNA ARRAYS

To demonstrate the plasmonic properties of NbN we have simulated and fabricated different nanoantenna arrays. The arrays in this section consist of a 50 nm thick NbN film on a MgO substrate with an area of $100 \times 100\ \mu m^2$.

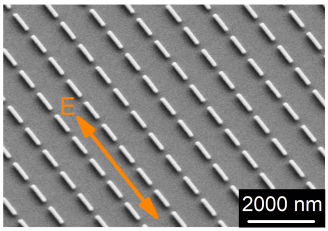

Figure 5.2: SEM image of a fabricated nanoantenna array. The double arrow indicates the applied electrical field for simulations and measurements of the plasmonic response.

Figure 5.2 depicts a SEM image of such a NbN nanoantenna array, as well as the applied electric field to measure the plasmonic response. We hereby excite the plasmon along the long side of the nanoantennas.

In order to fabricate appropriate nanoantennas, we have performed simulations of the desired nanostructures. To carry out these simulations we have used an in-house implementation of the Fourier modal method with a scattering matrix approach and 225 plane waves to model the nanoantenna arrays and their optical spectra, which is called smatrix. The smatrix program is written in Matlab and was implemented by Prof. Dr. T. Weiss [62, 63]. It is able to simulate the optical spectra of different types of nanostructures, for example such as nanoantenna and nanowire arrays or even more complex structures. Hereby the complex refractive index of the used materials is required for the calculation.

With the smatrix program we are able to model our desired 50 nm thick nanoantenna arrays and can calculate their corresponding transmission, absorption and reflection spectra. For our simulations we have utilized air with a refractive index of $n = 1$ as upper material and an infinite thick MgO layer with a refractive index of $n \approx 1.7$ as bottom substrate. For the plasmonic structures we have used the presented NbN permittivity data from figure 5.1 to calculate their corresponding complex refractive index with equation (2.11).

Figure 5.3 presents the simulated transmission spectra of 50 nm thick NbN nanoantenna arrays with different lengths, a width of 100 nm and a constant x- and y-periodicity of 500 nm. It confirms well-modulated and relatively narrow plasmon resonances in between wavelengths of 800 and 1500 nm. These resonances are fundamental nanoantenna dipole resonances

and not $\lambda/2$ resonances, as the effective wavelength of the material is used for such nanoantennas [64].

Furthermore, the resonance is tunable and scales with the length of the antenna. Longer antennas lead to resonances at higher wavelengths, and shorter antennas accordingly lead to a blue shift. This tunability allows access to important wavelength ranges, such as the telecommunications bands at 1310 and 1550 nm [65]. In addition, the modulation depth increases with larger antennas, leading to a modulation of up to 80%. These properties can be explained by the dipole nature of our resonances, as bigger antennas lead to larger dipole moments and hence to a higher interaction with the nanostructures.

An additional feature, which usually can only be observed in the simulated spectra are the sharp edges at 850 nm. These are Rayleigh anomalies caused by the perfect periodicity, geometry and boundary condition of the simulation. They arise due to a strong diffraction at the structures at a 90° angle. The anomalies chance for different periodicities, which can be verified by the simulation depicted in figure 5.5, and they occur at wavelengths which are the product of the periodicity and the refractive index of the substrate.

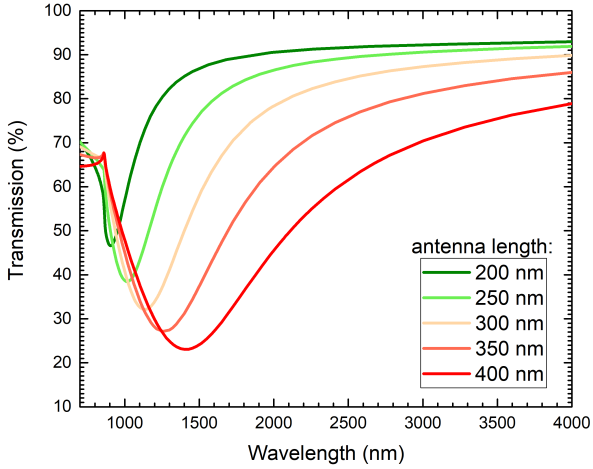

Figure 5.3: Simulated relative transmission spectra of 50 nm thick NbN nanoantenna arrays with different lengths, a width of 100 nm and a constant x- and y-periodicity of 500 nm [12].

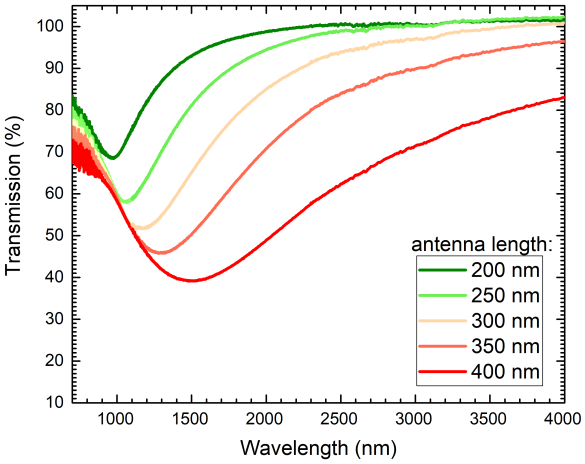

Figure 5.4: Measured relative transmission spectra of 50 nm thick NbN nanoantenna arrays with different lengths, a width of 100 nm and a constant x- and y-periodicity of 500 nm [12].

The measurement of the corresponding fabricated sample is presented in figure 5.4. It confirms the simulation results, as we observe the well-modulated and relative narrow plasmon resonances also in the measured spectra.

The measurements have been carried out with a Fourier-transform infrared spectrometer (FTIR). A FTIR utilizes the Fourier transformation to measure high resolution optical spectra over a wide spectral range. It uses a Michelson interferometer to produce a raw signal of light intensity versus mirror position. The intensity data are afterwards converted into a light intensity over wavelength plot. To ensure a clean and nice sample spectra a reference sample is measured. By subtracting the reference signal from the actual sample spectrum environmental and substrate influences are eliminated. In our case the used reference has been the MgO substrate, resulting in a relative transmission spectrum of the nanoantenna arrays.

By comparing the resonance wavelengths of measured spectra with the simulated ones we realize a good agreement, which confirms the good quality of our permittivity data and simulation program. The comparison of the modulation depths results in some slight mismatch since the simulation predicts a larger modulation. This is typical for simulations due to the perfect

periodicity, geometry and boundary condition, which are not possible in reality, because of fabrication imperfections and finite arrays.

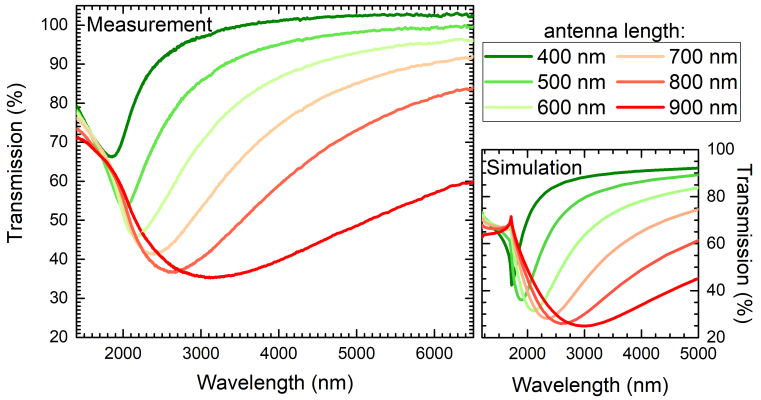

Figure 5.5: Transmission spectra of 50 nm thick NbN nanoantenna arrays with different lengths, a width of 200 nm and a constant x- and y-periodicity of 1000 nm. On the left side the measurement of the fabricated samples is shown and on the right the simulation is depicted for comparison [12].

Figure 5.5 depicts the measurement and simulation of a second set of 50 nm thick NbN nanoantenna arrays on MgO, this time with a larger periodicity of 1000 nm, a width of 200 nm and different antenna lengths. The left figure shows the measurement of the fabricated samples and the right picture displays the according simulation.

Once again, both plots confirm tunable, relatively narrow and well-modulated plasmon resonances. The larger period of the fabricated arrays enables longer nanoantennas, leading to higher resonance wavelengths of up to 3000 nm, due to their dipole nature. This demonstrates that NbN plasmonics can also be used in the mid-IR spectral range. The comparison of the two plots reveals again a good agreement of the simulations and the real sample measurements. The simulations also show the sharp Rayleigh anomalies and bigger modulation depths, due to the perfect simulated conditions.

In conclusion, NbN exhibits good plasmonic properties and yields well-modulated and tunable plasmonic resonances up into the mid-IR spectral range, which has been demonstrated using different plasmonic nanoantenna arrays.

5.2.1 *Temperature stability of the nanoantennas*

The high melting point of bulk NbN with over 2000 °C [66] and its internal oxidation temperature of 800 °C make NbN an excellent candidate for high temperature plasmonics. In this section we demonstrate the temperature stability of our nanoantennas up to 600 °C.

So-called refractory material are utilized for high temperature plasmonics [67, 68]. These materials exhibits melting points of over 2000 °C and high temperature stability. Refractory materials are for example different nitrides, such as TiN [55, 61, 69, 70], zirconium nitride [55, 71], titanium oxynitride [72, 73], tungsten [74] and Nb [11].

Even with the high melting and oxidation temperature of for example NbN, we have to take into account that the high temperatures can slightly change the plasmonic properties of our nanaoantennas, due to a change in their optical properties, as we are in the nanoscale regime [75].

As an additional step to improve the temperature stability of our nanostructures, we cover the sample with 10 nm of Al_2O_3 as protective layer via atomic layer deposition. This deposition method ensures a completely covered surface and yields different advantages. First it prevents oxidation, while annealing the sample under ambient condition, due to the fact that surface oxidation occurs already at lower temperatures compared to its bulk and second it protects the shape of our nanoantennas [76].

Figure 5.6 depicts the relative transmission spectra of a 50 nm thick NbN nanoantenna array with an antenna length of 700 nm, a width of 200 nm, a constant x- and y-periodicity of 1000 nm, which is covered with the protective Al_2O_3 layer. To measure these data the sample was annealed for 45 min at different temperatures up to 600 °C. Between each temperature step the relative transmission spectra was measured with the FTIR spectrometer. These measurements were carried out at room temperature to prevent a temperature induced change in our sample during the measurements.

The first measurement was done at room temperature, after applying the Al_2O_3 layer. The second measurement has been performed after the sample was annealed for 45 min at 100 °C. We notice a decrease in the modulation depth of around 10%, without a frequency shift, which could be explained by a change in the optical properties, as explained before. The

next measurements at 200 °C, 300 °C and 400 °C yielded the same results as the second one. After annealing the sample at 500 °C the modulation depth start decreasing again, leading to an almost vanished resonance after the 600 °C annealing step.

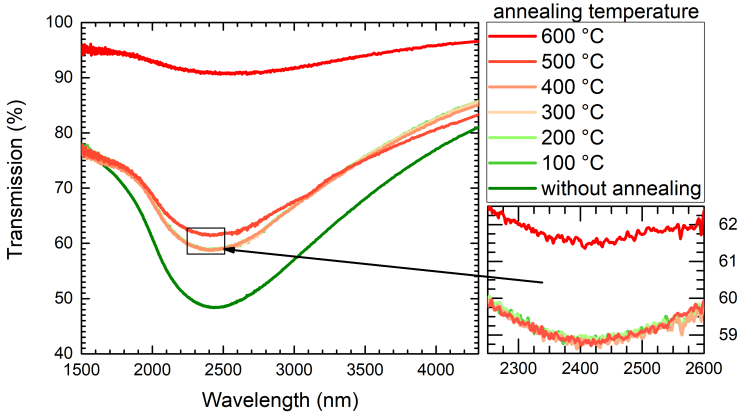

Figure 5.6: High-temperature plasmonic properties of NbN nanoantennas, covered with a protective 10 nm Al_2O_3 layer. Demonstrated by annealing a NbN nanoantenna array with an antenna length of 700 nm, a width of 200 nm and a constant x- and y-periodicity of 1000 nm at different temperatures for 45 minutes [12].

With figure 5.7, which displays a SEM image of the covered nanoantennas before and after the annealing steps, we are able to confirm the geometric temperature stability of our structures. Nevertheless, the plasmonic resonance almost vanished after the annealing at 600 °C leading to a strong reduction of the plasmonic properties. The most likely explanation for this behavior is an oxidation of the NbN and the formation of niobium oxynitride, causing a change in the optical properties of the nanoantennas due to the higher oxygen concentration [77].

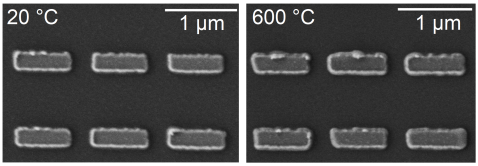

Figure 5.7: SEM image of a nanoantenna array covered with 10 nm Al_2O_3 at 20 °C before annealing and after annealing at 600 °C [12].

In conclusion, we have demonstrated good geometric temperature properties of up to 600 °C and good plasmonic properties of temperatures of up to 400 - 500 °C.

5.3 PERFECT ABSORBER NBN NANOANTENNAS

In order to utilize the plasmonic properties of Nb-based materials to create SNSPDs the absorption efficiency has to be enhanced, since we only have a maximum absorption of ≈ 40%, as showcased in section 5.2 above. One way to enhance the absorption is the so-called plasmonic perfect absorber principle, to reach almost 100% absorption, by suppressing reflection and transmission. The theoretical working principle is explained in section 2.3.3 and [20].

Since NbN exhibits good plasmonic properties and a nice match between the simulated and measured data, a smatrix simulation of a plasmonic perfect absorber was performed using the permittivity data shown in figure 5.1. This simulation has been carried out to check whether theoretically all conditions for a successful plasmonic perfect absorber enhancement are given by NbN. As dielectric spacer we used 125 nm Al_2O_3 as it is similar to sapphire and our collaborators in Taiwan are able to sputter high quality NbN films on sapphire. Multiple simulations have been carried out and the most promising results are depicted in figure 5.8, with following nanoantenna parameters, a width of 150 nm, a length 300 nm and different periodicities.

Figure 5.8 reveals the absorption of the described nanostructures. For adjusted and optimized parameters the simulation confirms an absorption of up to 99%. These promising results enable the next step on the way to plasmonic enhanced SNSPDs, as we can start focusing on the simulation and production of nanowire arrays, which are foundation structures of our later photodetectors.

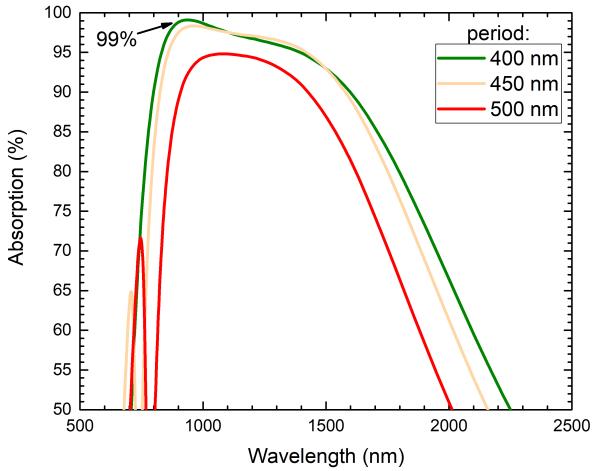

Figure 5.8: Simulated absorption spectra of 20 nm thick NbN nanoantenna arrays on a perfect absorber substrate with different periodicity, a width of 150 nm, a length 300 nm and 125 nm Al_2O_3 dielectric spacer.

6

NB-BASED PLASMONIC SUPERCONDUTCTION PHOTODETECTORS

This chapter is about the Nb-based plasmonic superconducting photodetectors. We present and discuss the absorption and plasmonic properties of Nb-based nanowire arrays, followed by the absorption spectra for different angles of incidence and the electric field distribution of our nanowires, to explain and lay the foundation of the detector structures. Before discussing the detector properties, the optical, electrical and cryogenic setup is introduced. Afterwards, we explain the detector design and confirm their working principle and properties under low temperature conditions. These steps are discussed at first for NbN and afterwards for Nb to avoid mixing and confusing the different materials. This first NbN part is published and based on our own publication [47].

As we will demonstrate that the detector absorption and response are strongly dependent on the polarization of the incoming photons. To tackle this property we have designed different polarization-independent structures and detector types. These are characterized and afterwards compared with each other and the polarization-dependent design. These NbN structures were published and are part of our own publication [48].

Quantum technologies are in high need for precise, highly efficient and fast single photon detectors for their applications. Therefore, SNSPDs are the ideal detectors for quantum technologies, as they are able to fulfill all these criteria. Their working principle, important characteristics and typical values are explained in chapter 3.

Up to date SNSPDs often utilize only the intrinsic absorption of the materials or mostly cavity effects [18, 19], leading to a strong angle of incidence dependency or large active areas. One big challenge is to create a detector

with a high quantum efficiency, hence a high absorption, while at the same time only using a small active detection area, to shorten the recovery time of the detector [78]. Plasmonic nanostructures and their resulting resonances are able to tackle this challenge, due to their high resonant absorption cross section. Moreover, the absorption of plasmonic structures can be further increased up to almost 100%, by utilizing the plasmonic perfect absorber principle. It additionally exhibits a strong angle of incidence independence, which could lead to even smaller detectors by the use of high-NA objectives and small focal spots.

6.1 NBN PERFECT ABSORBER NANOWIRE ARRAYS

Perfect absorber nanowire arrays form the basic structure of the later detectors. To begin we have simulated the absorption of different nanowire arrays to find the most promising structure geometries and fabricated the corresponding nanostructures later on.

Figure 6.1 presents a SEM image of the fabricated samples and clarifies the used polarizations in the grid-like nanowire samples. For the rest of this work we will always define TM polarization for the polarization in which the plasmons are excited. The simulations, as well as the measurements are also done in TM polarization, if not stated differently. TM polarized light is hereby perpendicular to the nanowires, as shown. TE polarized light is alongside the nanowires and only shows the intrinsic properties of the sample material.

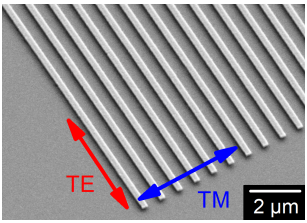

Figure 6.1: SEM image of the simulated and measured nanowire arrays, it displays an enlarged section of an array.

6.1.1 *Simulation*

The simulations in this section have been carried out using the smatrix program and the permittivity data displayed in figure 5.1. As dielectric spacer we

used Al_2O_3, due to similar properties and structure to sapphire. In addition, it exhibits basically no absorption with its imaginary refractive index of $\kappa \approx 0$ [79] in the near-IR region. With this parameters we have modeled the desired nanowire arrays to find the optimal structure geometries. During the process we have used a thickness of 20 nm for the NbN for all structures and simulation, if not stated differently. We optimized the spacer thickness, periodicity and wire width to reach almost 100% absorption around our target and laser wavelength of 1140 nm. On the following pages the optimized structures are shown and discussed, as well as the influence of the different geometric parameters.

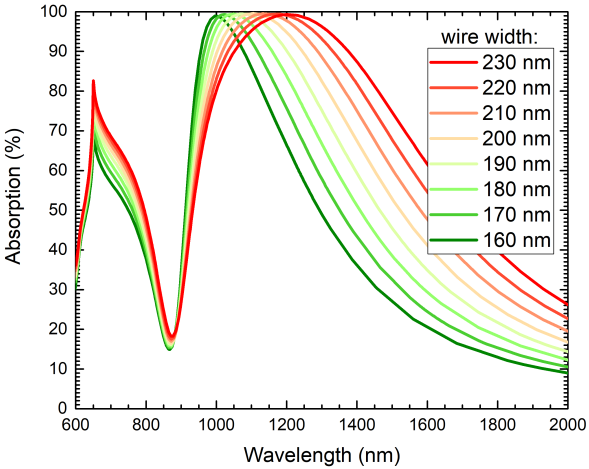

Figure 6.2: Simulated absorption spectra of 20 nm thick NbN nanowire arrays on a perfect absorber substrate with a constant period of 650 nm, an Al_2O_3 spacer thickness of 100 nm and different wire widths.

Figure 6.2 depicts the simulated absorption spectra of 20 nm thick NbN nanowire arrays on a perfect absorber substrate with a constant period of 650 nm, an Al_2O_3 spacer thickness of 100 nm and different wire widths. We notice high absorbing plasmon resonances with over 99% between 1000 and 1200 nm. The resonances shift red for larger wire widths, as expected for fundamental dipole resonances. These high absorbing plasmon resonances can be tuned even further in the IR spectral range by adjusting the different geometries.

An additional feature which is visible in the simulation is the sharp lattice mode at 650 nm, which matches exactly the period of the simulated structure. The shape of this lattice resonance overlaps partly with a weaker resonance, which can be observed in a few measured samples later on.

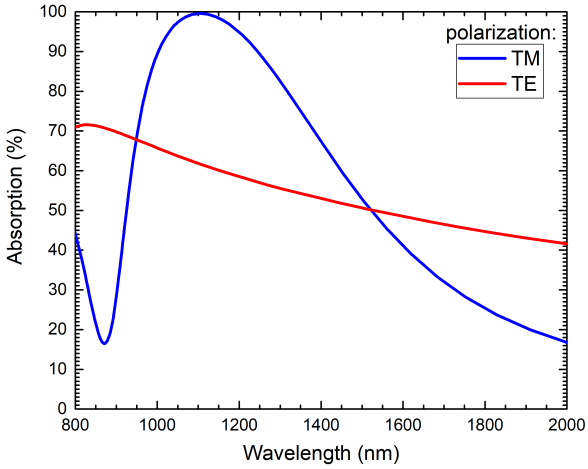

Figure 6.3: Comparison between TM and TE polarization of the simulated absorption spectra of a 20 nm thick NbN nanowire array on a perfect absorber substrate with a period of 650 nm, an Al_2O_3 spacer thickness of 100 nm and a wire width of 200 nm.

In figure 6.3 the comparison between TM and TE polarization of the optimized simulated absorption spectra of a 20 nm thick NbN nanowire array with a period of 650 nm, an Al_2O_3 spacer thickness of 100 nm and a wire width of 200 nm is presented. It reveals the strong absorbance enhancement by utilizing the plasmonic perfect substrate. As shown, the intrinsic absorption of NbN drops at higher wavelengths, due to more metallic and reflective behavior and additionally, these photons posses less energy, leading to fewer absorption possibilities.

To understand the influence of the different geometric parameters, such as spacer thickness and periodicity, we have simulated different nanowire arrays with 20 nm thick NbN on a perfect absorber substrate with a constant wire width of 200 nm.

First we have simulated the absorption spectra with a constant periodicity of 650 nm and different Al_2O_3 spacer thicknesses. These spectra are presented in figure 6.4. We notice high absorbing plasmon resonances for all the different spacer thicknesses. Depending on the target wavelength a different thickness is optimal, usually it applies that a thicker spacer is needed for higher wavelengths. Although, a thicker spacer shifts the resonance slightly blue.

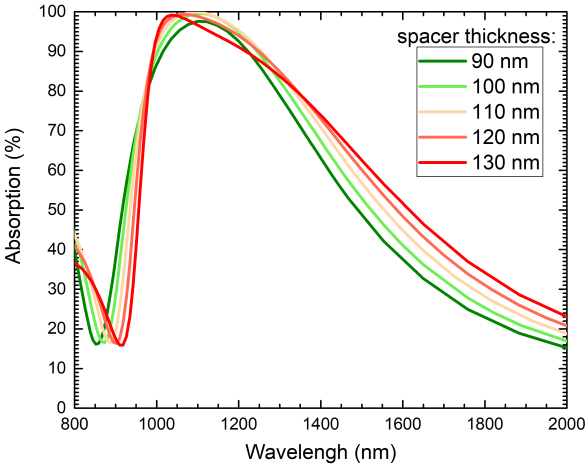

Figure 6.4: Simulated absorption spectra of 20 nm thick NbN nanowire arrays on a perfect absorber substrate with a constant wire width of 200 nm, period of 650 nm and different Al_2O_3 spacer thicknesses.

Figure 6.5 depicts the simulated absorption spectra with a constant Al_2O_3 spacer thicknesses of 100 nm and different periods. The high absorbing plasmon resonances are occurring again for a period of 500 - 700 nm. One notices a strong red shift for higher periods and a lower absorption for not optimized parameters. Once again, the sharp lattice mode is visible for the structure with the 800 nm period, as well as the weaker and overlapped second resonance.

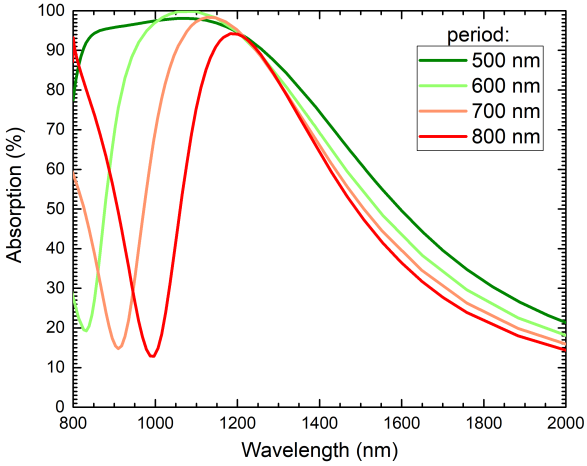

Figure 6.5: Simulated absorption spectra of 20 nm thick NbN nanowire arrays on a perfect absorber substrate with a constant wire width of 200 nm, an Al_2O_3 spacer thicknesses of 100 nm and different periods.

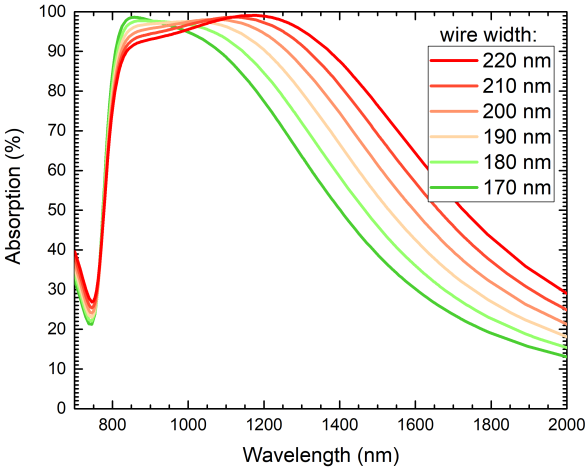

Figure 6.6: Simulated absorption spectra of 20 nm thick NbN nanowire arrays on a perfect absorber substrate with a constant period of 500 nm, an Al_2O_3 spacer thicknesses of 100 nm and different wire widths [47].

After simulating the absorption spectra with the different periods and observing a high absorbing plasmon resonance in a structure with a period of 500 nm, we have carried out additional simulation using this period.

Figure 6.6 presents the simulated absorption spectra of 20 nm thick NbN nanowire arrays on a perfect absorber substrate with a constant period of 500 nm, an Al_2O_3 spacer thicknesses of 100 nm and different wire widths. The simulation reveals also for this period high absorbing plasmon resonances, all with over 95% absorption between 900 and 1200 nm. The resonances shift red for larger wire widths and are well-modulated, showing the typical characteristics of a plasmon.

Furthermore, a smaller period leads to a more compact and dense structure, aiding the absorption in real samples, due to the less free space between the wires. As real samples show fabrication imperfections, a bigger effective active area can additionally increase the absorption.

Typical SNSPDs have a thickness of 7 - 10 nm to enhance the probability to detect a photon, as explained in chapter 3. Therefore, we have carried out simulation using different NbN thicknesses. For the simulation we used nanowire arrays on a perfect absorber substrate with a constant wire width of 200 nm, an Al_2O_3 spacer thicknesses of 100 nm, a period of 500 nm and different NbN thicknesses. The results of these simulations are displayed in figure 6.7.

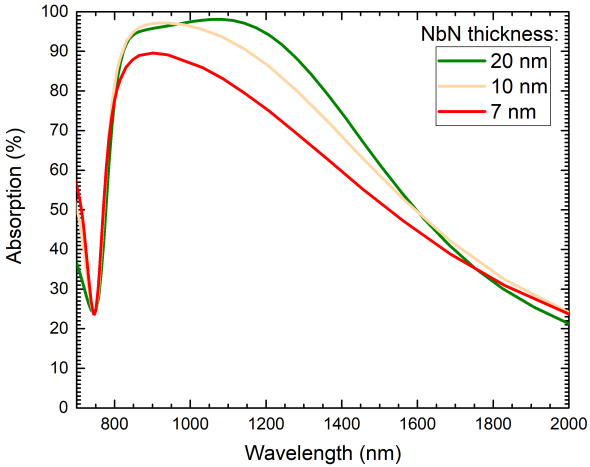

Figure 6.7: Simulated absorption spectra of NbN nanowire arrays on a perfect absorber substrate with a constant wire width of 200 nm, an Al_2O_3 spacer thicknesses of 100 nm, a period of 500 nm and different NbN thicknesses.

The simulations confirm for the 20 nm thick NbN the same high absorbing plasmon resonance as before and for 10 nm thick structures we still see a strong and well-modulated resonance. For 7 nm thick NbN the absorption of the simulated resonance is going down, this happens also with different parameters, the presented 90% absorbance is the maximum we could achieve. One reason for this behavior is the fact, that the plasmon needs a certain amount of space to manifest and with a thickness of 7 nm, we are already close to the limit.

Nevertheless, a 10 nm detector should be possible. In this work though we used 20 nm thick NbN, as the superconducting properties of our provided thin NbN films worsen drastically at 10 nm and with the high absorption enhancement, photons should still be reliably detectable. In addition, we notice a strong blue shift for smaller thicknesses, leading to wider wire widths to keep the target resonance wavelength and all in all to almost the same structure volumes. Nonetheless, this feature can be useful when operating at lower wavelengths.

In this part, high absorbing and tunable plasmon resonances with over 99% absorption have been demonstrated. These structure geometries provide the starting points for the fabrication of the real samples.

6.1.2 *Measurements*

After successfully simulating the nanowire array structures and confirming high absorbing plasmon resonances, we have fabricated the corresponding real structures with an area of $100 \times 100\ \mu m^2$. The detailed fabrication process of the samples is explained in chapter 4. The measurements of the samples have been done with a FTIR spectrometer. As reference we have used a spot at the same sample without nanostructures. This ensures that fabrication differences in the perfect absorber substrate are taken into account. The FTIR measures the light intensity which is reflected by the sample and subtracts the reference, giving us the relative reflection spectrum R of the measured nanostructure. Since the transmission T is zero, due to thick gold mirror, the absorption A can be calculated as

$$A = 1 - R - T \qquad \text{with } T = 0, \tag{6.1}$$

resulting in the relative absorption spectrum of the nanowire array.

Figure 6.8 presents the measured absorption spectra of 20 nm thick NbN nanowire arrays on a perfect absorber substrate with a constant period of 500 nm, an Al_2O_3 spacer thickness of 100 nm and different wire widths. It reveals the same highly absorbing plasmon resonances, which were already predicted in the simulations and the maximum absorbance is over 95%. Moreover, it confirms the tunability of the resonances, as the plasmon absorption shifts red for larger wire widths, due to its dipole nature. However, the absorption decreases for larger widths, since the structure has been optimized for wavelengths around 1140 nm.

In addition, the resonances are broadband, which gives the opportunity to use a single wire array or detector for more than one wavelength. This feature is not possible for other approaches like cavities, as they are only usable at their designed narrow wavelength range.

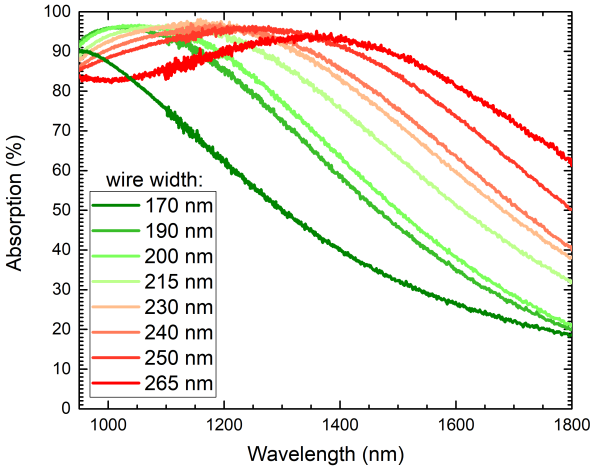

Figure 6.8: Measured absorption spectra of 20 nm thick NbN nanowire arrays on a perfect absorber substrate with a constant period of 500 nm, an an Al_2O_3 spacer thickness of 100 nm and different wire widths in TM polarization [47].

In figure 6.9 we have measured the same structure as in figure 6.8, but this time in TE polarization. The absorption reaches a maximum of around 50% in the lower wavelength region and none of the spectra show any sign of a resonance. This behavior confirms again the plasmonic nature of the displayed resonances. Furthermore, it demonstrates the strong enhancement through the optimized plasmonic perfect absorber substrate, as the intrinsic

absorption drops at higher wavelengths, due to the more metallic and hence more reflective properties of NbN.

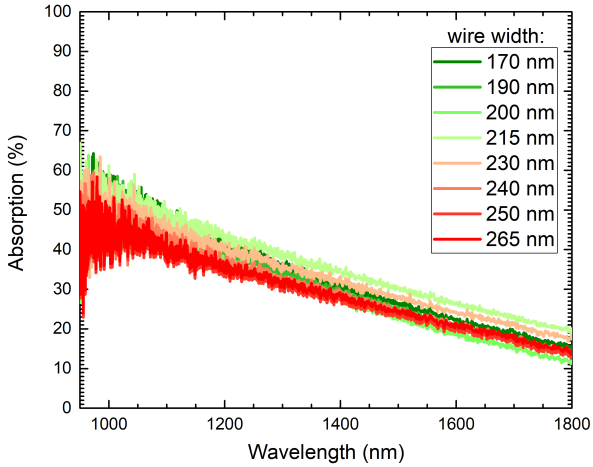

Figure 6.9: Measured absorption spectra of 20 nm thick NbN nanowire arrays on a perfect absorber substrate with a constant period of 500 nm, an Al_2O_3 spacer thickness of 100 nm and different wire widths in TE polarization [47].

Since the simulations have also shown a promising high absorption for arrays with a periodicity of 650 nm, we also fabricated and measured arrays with a period of 600 and 700 nm. The measured absorption spectra of 20 nm thick NbN nanowire arrays on a perfect absorber substrate, with a constant period of 600 nm, an Al_2O_3 spacer thickness of 100 nm and different wire widths are depicted in figure 6.10. Here we notice tunable plasmon resonances with an absorption of over 90%. This is lower compared to the simulation and the arrays with a period of 500 nm. One possible explanation is the fact, that real samples exhibit fabrication imperfections and in addition, real samples have no perfect boundary conditions. The sample with the 500 nm period also has a larger effective active area than the 600 nm sample, as both wire arrays are $100 \times 100\ \mu m^2$ large.

By comparing the resonance wavelengths of wires with the same wire width but different periods, it confirms the result predicted by the simulation, as we notice a red shift for higher periods. This behavior is even better visible by using figure 6.11, as these arrays have a period of 700 nm.

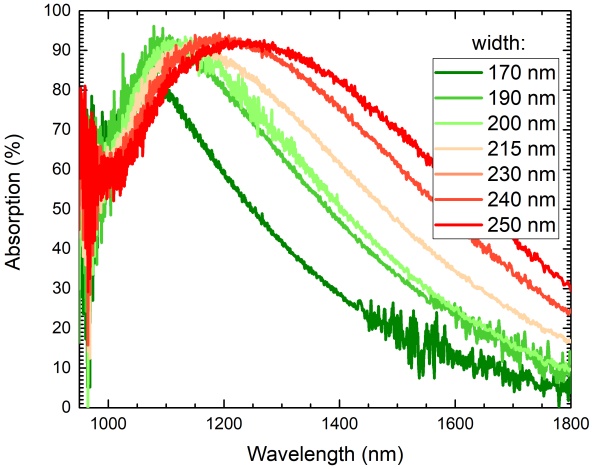

Figure 6.10: Measured absorption spectra of 20 nm thick NbN nanowire arrays on a perfect absorber substrate with a constant period of 600 nm, an Al_2O_3 spacer thickness of 100 nm and different wire widths in TM polarization.

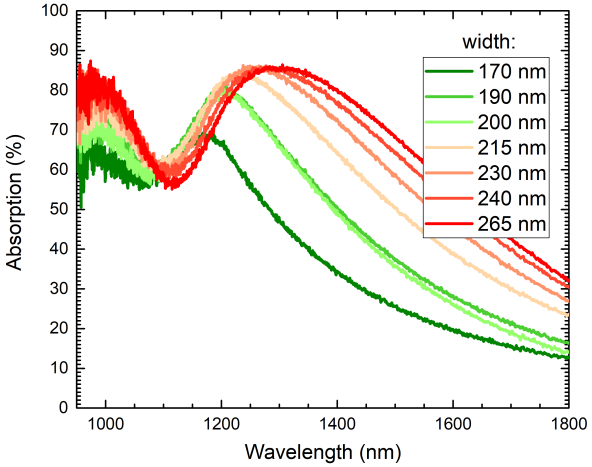

Figure 6.11: Measured absorption spectra of 20 nm thick NbN nanowire arrays on a perfect absorber substrate with a constant period of 700 nm, an Al_2O_3 spacer thickness of 100 nm and different wire widths in TM polarization.

As mentioned, figure 6.11 depicts the measured absorption spectra of 20 nm thick NbN nanowire arrays on a perfect absorber substrate with a

constant period of 700 nm, an Al_2O_3 spacer thickness of 100 nm and different wire widths. It displays plasmon resonances with an absorption of around 85%, which is lower compared to the other two. Since these arrays have a large period of 700 nm it is possible to see the weaker second resonance at lower wavelengths, also predicted by the simulation. Even with the lower absorption compared to the 500 and 600 nm period sample, we still see a strong enhancement compared to the intrinsic absorption of NbN at these wavelengths.

In this section we have shown well-modulated, broadband, high absorbing plasmon resonances on real NbN samples and demonstrated their plasmonic nature, as well as the strong enhancement induced by the plasmonic perfect absorber principle.

6.1.3 *Comparison of Measurements and Simulation*

In this part we directly compare several of the measured nanowire arrays with their corresponding simulations. Figure 6.12 compares the measured and simulated absorption spectra of 20 nm thick NbN nanowire arrays on a perfect absorber substrate with a constant period of 500 nm, an Al_2O_3 spacer thicknesses of 100 nm and different wire widths.

The resonance wavelengths show an excellent match between simulation and measurement. The maximum absorption an the other hand, is slightly smaller for the real samples. This can be explained by the perfect boundary and geometric condition, such as the infinite array, used in the simulations. Real samples on the other hand always show some fabrication imperfection and finite borders.

In conclusion, the simulated and the corresponding measured real nanostructures exhibit a good match, which once again confirms the excellent quality of our simulations and permittivity data shown in figure 5.1.

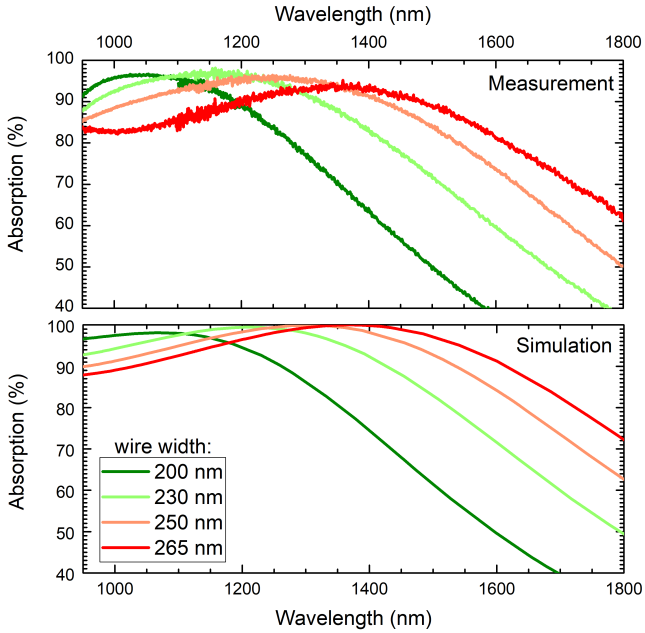

Figure 6.12: Comparison of measured and simulated absorption spectra of 20 nm thick NbN nanowire arrays on a perfect absorber substrate with a constant period of 500 nm, an Al_2O_3 spacer thicknesses of 100 nm and different wire widths [47].

6.2 ELECTRIC FIELD ENHANCEMENT AND ANGLE INDEPENDENCE

The previous sections confirmed the excellent quality of the simulated spectra and the good match between simulation and measurement. With this knowledge we have carried out simulations for different angles of incidence for our nanowire arrays to demonstrate the angle of incidence independence of the plasmonic perfect absorber structure [80, 81]. In addition, we have simulated the electric field enhancement and field distribution to confirm the absorption and light interaction of our structures and to ensure that the photons are absorbed in the plasmonic nanostructure on top and not in the dielectric spacer or gold mirror below.

Figure 6.13 demonstrates the angle dependence for our simulated structure. Therefore, we simulated the absorption spectra of a 20 nm thick NbN nanowire arrays on a perfect absorber substrate with a constant wire width

of 200 nm, an Al_2O_3 spacer thicknesses of 100 nm, a period of 500 nm and different angles of incidence. These array parameter have been chosen, because they correspond to the parameters of the NbN detector discussed later.

We notice again the almost 100% absorption for normal incidence. For small angles up to 30° the simulated absorption spectra hardly change at all. The first real change is observed at 45°, where the absorption drops to around 95% and the resonance peak shifts slightly red. For angles over 60° the absorption is reduced to 90% and shifts ≈ 100 nm red, for even higher angles such as 80° the maximum absorption drops to 55%, but shows a weaker red shift.

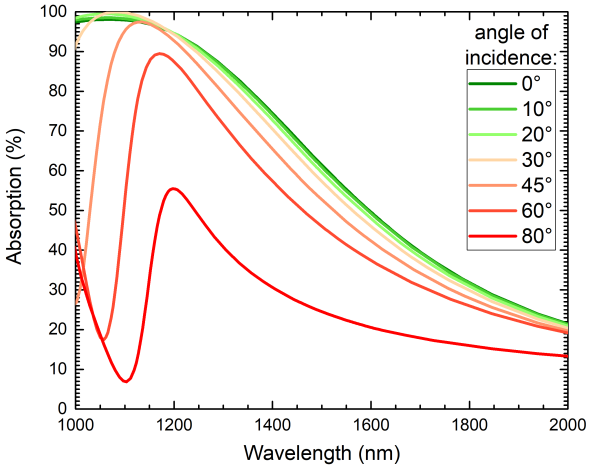

Figure 6.13: Simulated absorption spectra a 20 nm thick NbN nanowire array on a perfect absorber substrate with a constant wire width of 200 nm, an Al_2O_3 spacer thicknesses of 100 nm, a period of 500 nm and different angles of incidence [47].

In Figure 6.14 we depict the simulated electric field enhancement distributions for the 20 nm thick NbN wire array, which is the same structure as before, for 1140 nm (at resonance) and for 2000 nm (off resonance). The interaction of the plasmonic structure with the incoming light can be observed by looking at the electrical field distribution, whereby an interaction leads to strong enhancement.

For the distribution at a wavelength of 1140 nm we observe a strong electric field at the edges of the plasmonic NbN structure above the Al_2O_3 spacer. In addition, there are no other parts that show an enhancement, which confirms that the incoming light is basically completely absorbed by the plasmonic nanostructure. The simulation for 2000 nm also reveals interactions only at the plasmonic structure, but the interaction is weaker compared to the one at 1140 nm due to the smaller absorption.

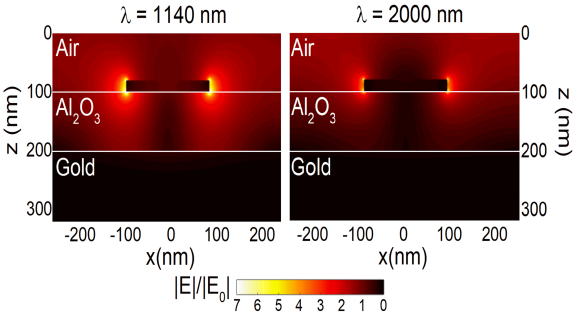

Figure 6.14: Simulated electric field enhancement distributions of a 20 nm thick NbN wire array for 1140 nm (at resonance) and for 2000 nm (off resonance) [47].

All in all we have demonstrated in this section the strong angle of incidence independence of our structure and confirmed that the light is absorbed by the plasmonic structure on top. This can enable the production of ultra-small detectors by using high-NA objectives, leading to small recovery times and hence faster detectors.

6.3 FREE SPACE MEASUREMENT SETUP

In this section the free space measurement setup will be discussed. All cryogenic measurements of the following detectors have been carried out by using this setup.

6.3.1 *Cryostat and electrical setup*

The cryostat which has been used for the measurements is depicted in figure 6.15. It is a bath cryostat from Oxford. The lowest temperature it can reach is ≈ 1.4 K at the bottom of its inner chamber, this inner part is called

variable temperature inset (VTI). The temperature in the VTI can be chosen between 1.4 and 300 K, due to the use of liquid helium in combination with a built-in heater. To reach this low temperatures the VTI is shielded with a vacuum chamber at the outer part and a liquid nitrogen and helium chamber in the middle. The vacuum stops heat transport caused by particles, such as air molecules, while the nitrogen shields against radiation.

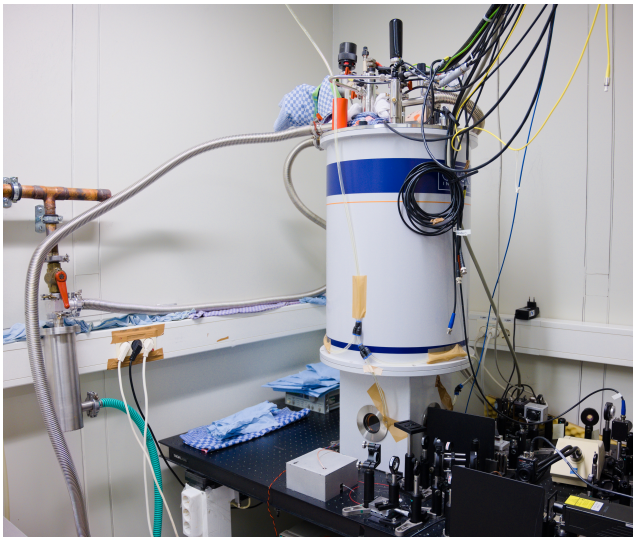

Figure 6.15: Picture of the used cryostat. On the bottom of the cryostat are four windows, which give optical access to the sample.

Figure 6.16: Picture of the used sample holder.

The VTI is actively cooled by liquid helium and by pumping at the VTI chamber with a helium pump. It is connected to the big helium bath via a small needle valve, by opening this valve liquid helium can be sucked in the VTI chamber and starts cooling the whole chamber, as well as the sample

and its holder. Liquid helium has a base temperature of 4.2 K and due to the pumping we can reach low temperatures of 1.4 K by utilizing the vapor pressure curve of helium.

The sample itself is mounted at the right end of a long sample holder, depicted in figure 6.16. This sample holder is inserted at the top of the cryostat. After installing the holder, we have optical access to the sample via four windows at the bottom of the cryostat. These windows are used to illuminate our detectors with the laser to perform the detector response measurements.

To measure the actual detector response, which is a voltage drop, four thin cooper wires are installed on the sample holder. These wires are used to perform a four-point resistance measurement. The needed current is applied via a KEITHLEY 2611B current source and the voltage drop caused by the sample is simultaneously measured with a KEITHLEY 2182A nanovoltmeter. In addition, to ensure good thermal stability of the sample and the four wires, the latter ones are winded around the sample holder.

6.3.2 *Optical setup*

The optical part of the measurement setup consists of a continuous wave Topica ECDL Pro laser source with a wavelength of 1140 nm, mirrors, two linear polarizer, one $\lambda/2$ plate, a CCD camera, a 50/50 beam splitter and lenses. In figure 6.17 we present a schematic sketch with the arrangement of the different components.

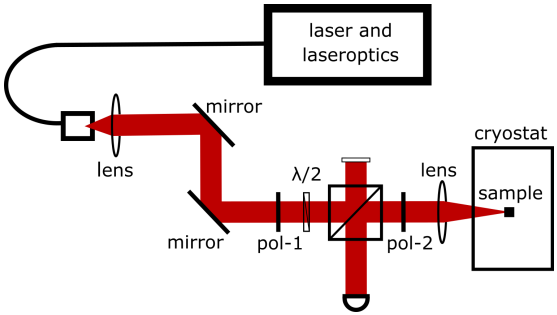

Figure 6.17: Schematic representation of the optical setup to measure the detectors under incident light.

With the first lens we collimate the laser beam after it leaves the fiber and the last lens focuses the beam on the sample. The 50/50 beam splitter is used to depict the light reflected from the sample into a CCD camera, which is utilized to align the laser beam on the detector structure. The mirrors are also used to align the laser spot with the nanostructure. The two linear polarizer and the $\lambda/2$ plate enable us to adjust the laser power which impinging at the sample, whereby the last polarizer also specifies the polarization of the laser light hitting the detector structure. The resulting laser spot size on the sample is hereby in the same order of magnitude as detector structure itself.

6.4 NBN PERFECT ABSORBER NANOWIRE DETECTORS

This section is about the design and performance of the 20 nm thick NbN detectors with a constant period of 500 nm, an Al_2O_3 spacer thickness of 100 nm, a wire width of 200 nm and an active area of $30 \times 30\ \mu m^2$. We will discuss the design, its absorption spectrum in the near-IR and visible spectral range, as well as its superconducting properties and electrical response under light incidence.

6.4.1 *Design*

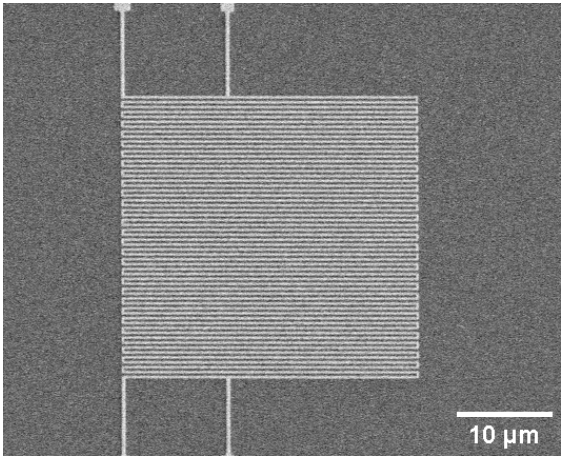

Figure 6.18: SEM image of the active detection area of a finished detector structure.

The designed active area of the detector is similar to the plasmonic wire arrays, but this time the active area has a size of only $30 \times 30\ \mu m^2$ and in

addition the different wires are connected at alternating ends to form one long continuous wire. The active area is depicted in figure 6.18.

Four larger NbN lines connect the small active area to four big Au contact pads with an area of $250 \times 250\ \mu m^2$ each. The entire structure, with its pads in the corners, is displayed in figure 6.19. These large contact pads are used to connect the detector structure with the cooper wires of the cryostat to perform a four-point resistance measurement.

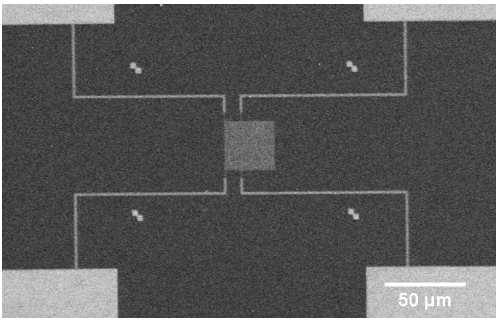

Figure 6.19: SEM image of an entire finished detector structure, with the big Au contact pads in each corner, which are used to carry out a four-point resistivity measurement.

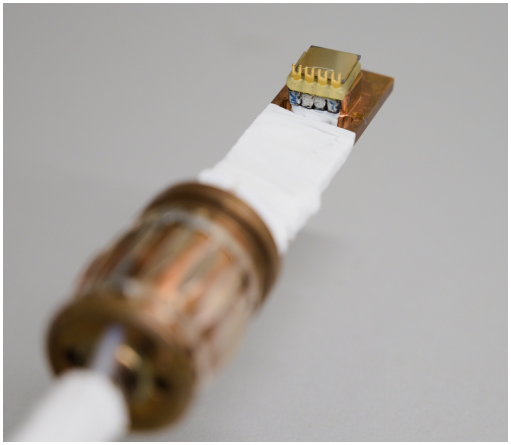

Figure 6.20: Picture of a finished and bonded detector on a chip carrier and mounted on the sample holder.

To be able to contact the detector with the cryostat, an additional component is needed. Therefore, we have used a chip carrier with four pins, as shown in figure 6.20. The nanostructure itself is hereby connected to the chip carrier with small gold bonding wires, one from each pin to one Au pad.

6.4.2 *Absorption*

The measured absorption spectrum for TM and TE polarization of our 30 × 30 µm^2 NbN detector is depicted in figure 6.21. Compared to the 100 × 100 µm^2 wire array we notice a red shift of ≈ 50 nm of the maximum. This could be caused by the shorter wires and the additional connections at their ends. The maximum absorption is around 90 - 95%, which is also slightly smaller compared to the wire arrays. There could be several reasons for this behavior. One could be that there are now less wires overall. Another reason could be bigger measurement uncertainties, as we have to further close the beam aperture in the FTIR, which makes the measurement more difficult and stray light has a greater impact on the measurements on such small structures, which leads to smaller measured absorptions. The small reduction however, is a great result, considering the fact that the active area was reduced by over 90%.

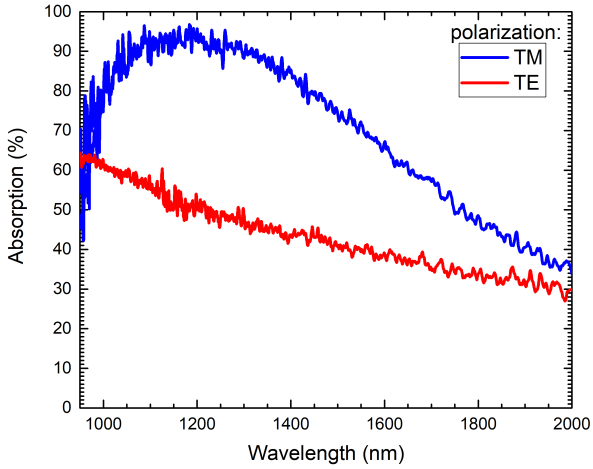

Figure 6.21: Measured absorption spectra of the 20 nm thick NbN detector on a perfect absorber substrate with a constant period of 500 nm, an Al_2O_3 spacer thickness of 100 nm and a wire width of 200 nm [47].

By comparing the absorption between the TM and TE polarization we, once again, observe a big difference. The excited plasmon resonance enhances the absorption also for the small detector structure by a factor of two in the near IR spectral range. The resonance itself is still broadband and could hence be used for more than one wavelength.

The simulated absorption for the structure, displayed in figure 6.22 reveals a good agreement between simulation and measurement. Furthermore, it confirms the plasmonic absorption enhancement.

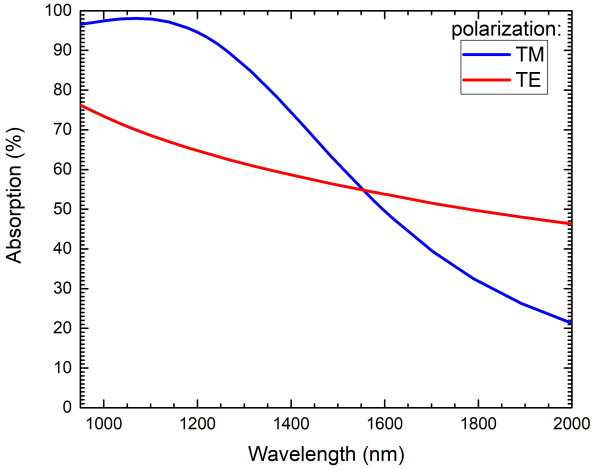

Figure 6.22: Simulated absorption spectra of the 20 nm thick NbN detector on a perfect absorber substrate with a constant period of 500 nm, an Al_2O_3 spacer thickness of 100 nm and a wire width of 200 nm [47].

6.4.3 *Superconducting properties*

The superconducting properties can change during the fabrication process, for example due to the heating during the baking of the photoresists and etching process. Therefore, we check these properties again, before starting to measure the actual detector response to light incidence.

In figure 6.23 the black curve represents the normalized measured resistance of the cooled detector structure in the cryostat, obtained with a four-point resistivity measurement. The green curve shows the normalized

magnetic moment of the unstructured NbN film, measured with the SQUID. The superconducting to normal conducting transition is in both measurements between 9.5 and 12 K, leaving us with an averaged critical temperature of $\approx$ 11 K. The fact that both curves represent the same critical temperature reveals that the fabrication process does not effect the superconducting properties of our NbN films.

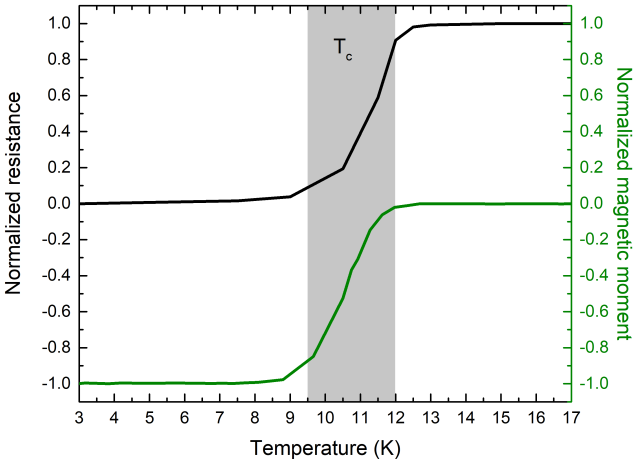

Figure 6.23: Normalized resistance and normalized magnetic moment of the demonstrated 20 nm thick detector structure. The resistance measurement has been performed with a four-point measurement and the magnetic moment has been measured in a SQUID device. Both measurement indicate a critical temperature of $\approx$ 11 K [47].

The critical current I_c of the demonstrated NbN detector for different temperatures is depicted in figure 6.24. The data points were fitted with the following function

$$I_c(T) = I_{c0}\left(1 - \left(\frac{T}{T_c}\right)^2\right), \tag{6.2}$$

with the critical current I_{c0} for $T = 0$ K. This function results from the critical magnetic field, which is explained in [43]. The fit confirms a critical temperature of 11.2 K. Furthermore, the critical currents for different temperatures are important for the response measurement later on, since for applied bias currents above this critical current no detector responses can be detected, as the structure is no longer in its superconducting state.

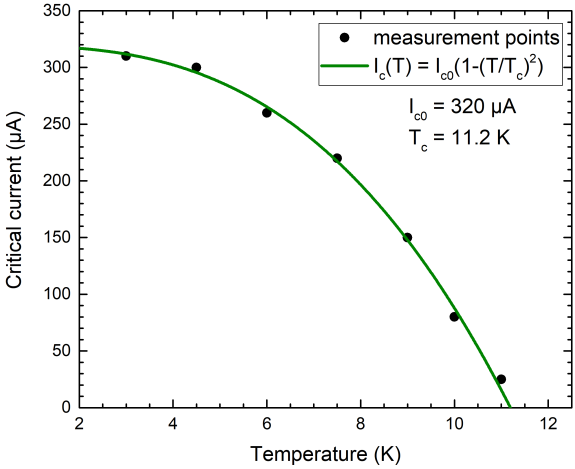

Figure 6.24: Measured critical current of the demonstrated 20 nm thick NbN detector. The fitted function confirms a critical temperature of 11.2 K [47].

6.4.4 *Detector response*

After confirming the superconducting properties of the detector structure, we look at the actual detector response to our external light source with a wavelength of 1140 nm under cryogenic conditions. To perform the following measurements, the setup described in section 6.3 was used.

To ensure the maximal response, the optimal bias current has been determined. Figure 6.25 depicts the measured detector response of the NbN detector for different applied currents to find the optimal bias current at 1140 nm, at a temperature of 3.5 K and with a constant laser power of ≈ 23 µW. This proves the functionality and concept of the detector, as we see a voltage drop for certain applied bias currents while illuminating the structure.

The investigation of figure 6.25 reveals a maximum detector response for an applied current of 220 µA. This current is slightly below the critical current at 3.5 K of ≈ 300 µA. In addition, we notice that for small currents, no detector response is visible, as the current density is too low to trigger the superconducting to normal conducting transition. For higher currents, some of the structure could already be in the normal conducting state, hence leading to a weaker response, as less structure could switch.

Currents over 350 µA give no response, as we have determined the maximum critical current of the structure with 320 µA, as measured in figure 6.24.

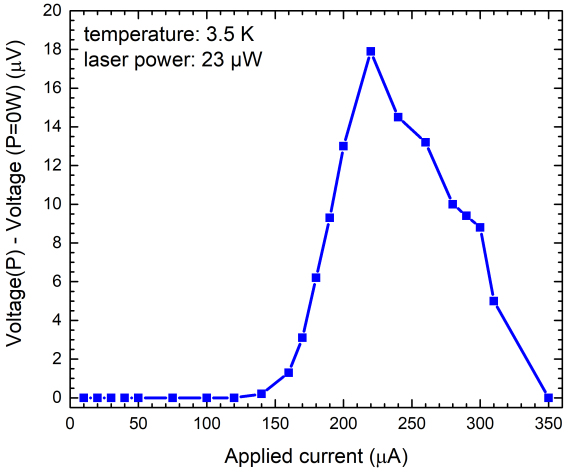

Figure 6.25: Measured detector response of the 20 nm thick NbN detector on a perfect absorber substrate for different applied currents to find the optimal bias current, at 1140 nm, 3.5 K and with a constant laser power of ≈23 µW [47].

Figure 6.26 depicts the measured detector response of the NbN detector on a perfect absorber substrate with a wire width of 200 nm for different laser powers and both polarizations and with the optimized applied current of 220 µA. The stronger absorption in TM polarization, compare figure 6.21, is clearly visible in the voltage drop, measured with the four-point measurement.

The detector is able to detect laser powers of under 1 µW in TM polarization. In TE polarization a minimum of ≈ 2 µW is needed, confirming a stronger response and hence a higher detection efficiency for TM polarized light, which in addition leads to a polarization-dependent response. The overall shape of the response resembles a curve, which ends in a plateau for high laser powers, due to the fact that at this point most of the structure is normal conducting, due to the high laser power and the introduced heat. In addition, this is leading to an indistinguishability between both polarization due to the heating.

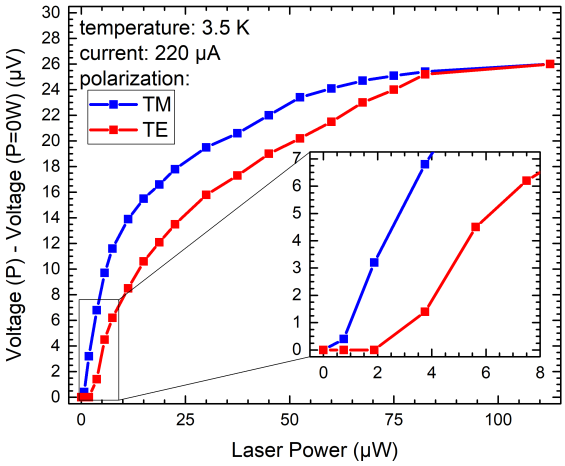

Figure 6.26: Measured detector response of the 20 nm thick NbN detector on a perfect absorber substrate with a wire width of 200 nm, for different laser powers, both polarizations and an optimized applied current of 220 µA [47].

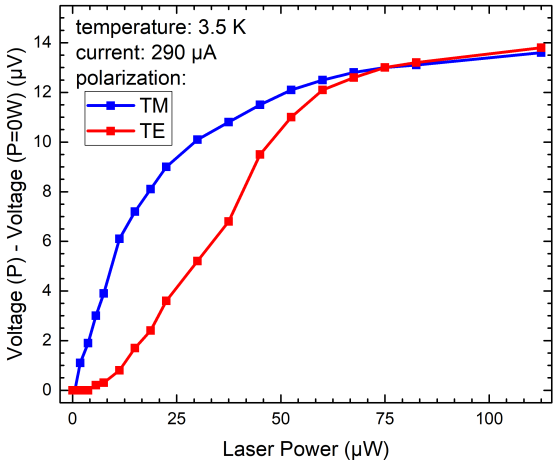

Figure 6.27: Measured detector response of the 20 nm thick NbN detector on a perfect absorber substrate with a wire width of 200 nm, for different for different laser powers, both polarizations and with a not optimized applied current of 290 µA [47].

Figure 6.27 confirms the results obtained in figure 6.25, since it presents the measured detector response of the same NbN detector under the same conditions, but this time with a not optimized applied current of 290 µA. The shape of the response is similar to the measurement with 220 µA, however, the overall voltage drop is smaller, due to the not optimized current, as explained before.

The detector response has also been investigated at different temperatures of 8.5 K and 20 K, these results are displayed in figure 6.28. For the measurement at 8.5 K the optimized current has been determined before the response measurement and is 120 µA. This is lower compared to the measurements at 3.5 K, as the critical current is temperature dependent, see figure 6.24. The measurement at 8.5 K also exhibits the same characteristics as the other response measurements. The difference to the other measurements at lower temperatures is the overall lower voltage drop. Possible explanations are, that at this temperature some small parts of the detector could be already in their normal conducting state. Moreover, the lower applied current could be a reason.

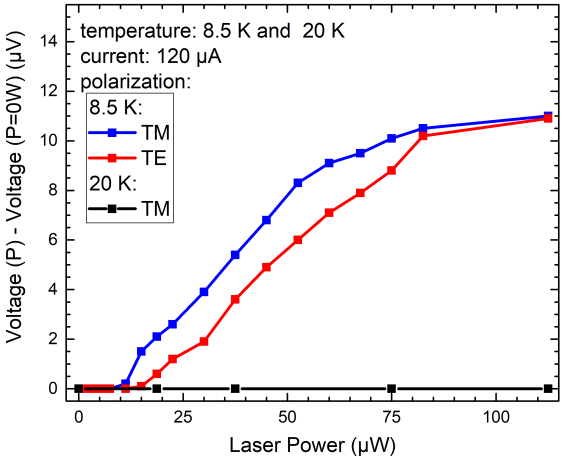

Figure 6.28: Measured detector response of the 20 nm thick NbN detector on a perfect absorber substrate with a wire width of 200 nm, for different for different laser powers, both polarizationsand with an optimized applied current of 120 µA at 8.5 K [47].

Measurements at 20 K show no measurable response to light, because the structure is no longer superconducting. This behavior confirms the working

principle of our structures and demonstrates that heating alone can not create a response.

6.4.5 *Detector response for other wavelengths*

The measurements and simulations of the nanowire array predicted an additional resonance at lower wavelengths. Therefore, the absorption of the detector has been measured with a grating spectrometer for the visible spectral range, which is connected to a microscope. The result is depicted in figure 6.29 and presents the measured absorption spectra in the visible and IR spectral range of the 20 nm thick NbN detector on a perfect absorber substrate with a constant period of 500 nm, an Al_2O_3 spacer thickness of 100 nm and a wire width of 200 nm.

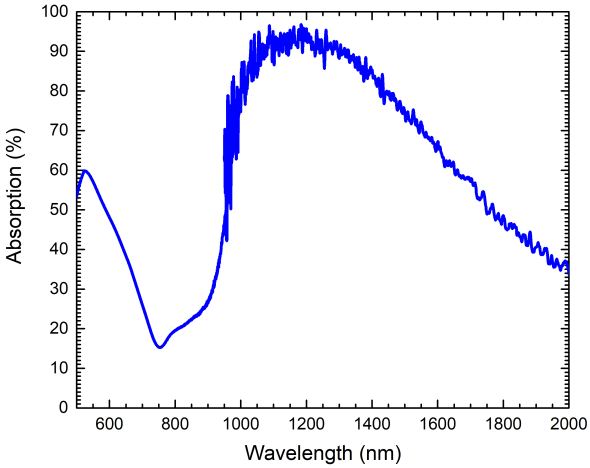

Figure 6.29: Measured absorption spectra in the visible and IR spectral range of the 20 nm thick NbN detector on a perfect absorber substrate with a constant period of 500 nm, an Al_2O_3 spacer thickness of 100 nm and a wire width of 200 nm.

The measurement confirms the existence of the additional resonance at around 550 nm, however this resonance is much smaller than the optimized plasmon resonance at higher wavelengths. The maximum absorption is 60%. By comparing this to the absorption in TE polarization at 1140 nm, which is

also around 60% we realize that the detector should also give a measurable response at these lower wavelengths.

Figure 6.30 verifies this expectation and compares the measured detector response for different wavelengths, 1140 nm and 561 nm, of the NbN detector. The measurement was performed at 3.5 K, with the optimized applied current of 220 µA and in TM polarization.

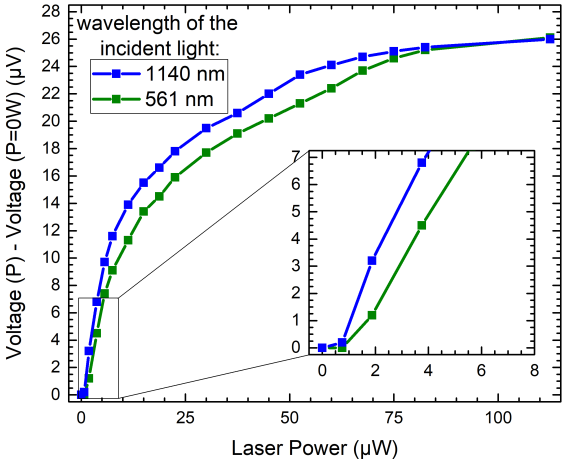

Figure 6.30: Measured detector response for different wavelengths of the 20 nm thick NbN detector on a perfect absorber substrate with a constant period of 500 nm, an Al_2O_3 spacer thickness of 100 nm and a wire width of 200 nm. The measurement has been performed in TM polarization, at 3.5 K and with an optimized applied current of 220 µA.

As expected by comparing the absorption for the different wavelengths and polarization, the response for light with a wavelength of 561 nm is similar to the measurement at 1140 nm in TE polarization, see figure 6.26. This is possible, since the experimental conditions, such as temperature, applied current and absorption are nearly identical.

All in all we have demonstrated the absorption and the working principle of our NbN detector structures and proved the fact that the enhanced absorption leads to a higher detection efficiency and in addition to a polarization-dependent response.

6.5 NB PERFECT ABSORBER NANOWIRE ARRAYS

The 50 nm thick Nb films can be sputtered in-house giving us the opportunity to test different designs and ideas. Therefore, we like to present some results of the Nb samples, which are also sputtered and structured on a optimized perfect absorber substrate. The overall dimensions and designs are comparable to the NbN nanaowire array and are illustrated in figure 6.1.

As we have already discussed a great variety of simulations and measurement, as well as the influence of the different geometric parts of the structure for the NbN wire arrays, we will demonstrate and discuss in this section only a few important and the most promising structures to create an overview.

6.5.1 *Simulation*

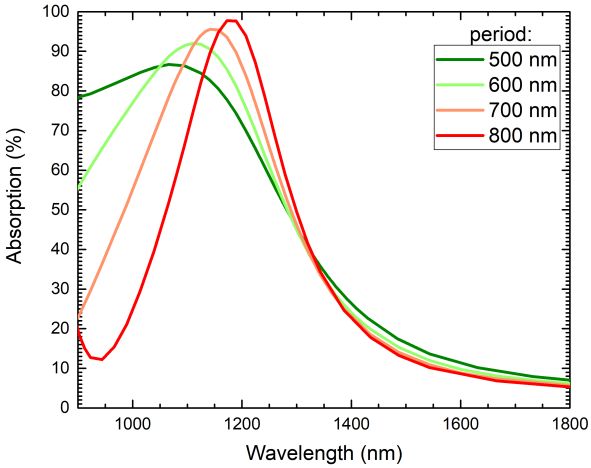

Figure 6.31: Simulated absorption spectra of 50 nm thick Nb nanowire arrays on a perfect absorber substrate with a constant wire width of 170 nm, an Al_2O_3 spacer thickness of 70 nm and different periods.

Before starting the fabrication process, simulations are carried out to determine the optimal sample geometry, such as spacer thickness, period and wire width. A few exemplary simulations are displayed in figure 6.31, which depicts the simulated absorption spectra of 50 nm thick Nb nanowire arrays on a perfect absorber substrate with a constant wire width of 170 nm,

an Al_2O_3 spacer thickness of 70 nm and different periods. The simulations reveal some highly absorbing plasmon resonances with over 95% absorption and confirm the red shift of the plasmon for larger periods.

Figure 6.32 compares the simulated absorption spectra of 50 nm thick Nb nanowire arrays on a perfect absorber substrate with a constant period of 600 nm, an Al_2O_3 spacer thickness of 70 nm and a wire width of 170 nm in TM and TE polarization. As demonstrated for the NbN wire arrays, the Nb arrays exhibit a strong absorbance enhancement for TM polarization compared to the intrinsic absorption of the material, represented by the absorption measured in TE polarization.

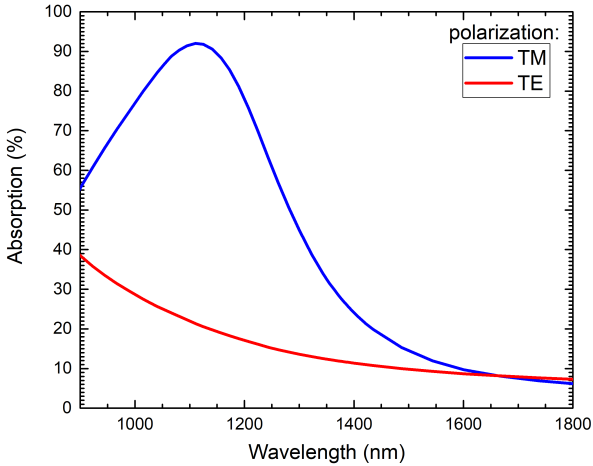

Figure 6.32: Simulated absorption spectra of 50 nm thick Nb nanowire arrays on a perfect absorber substrate with a constant period of 600 nm, an Al_2O_3 spacer thickness of 70 nm, a wire width of 170 nm in TM and TE polarization.

6.5.2 *Measurements*

After confirming the high absorbing plasmonic resonances we have fabricated the corresponding Nb nanowire array samples. These arrays also have an active area of $100 \times 100\ \mu m^2$. The fabrication process is explained in chapter 4 and the measurement process is described in the NbN part.

Figure 6.33 depicts the FTIR measurement and the measured absorption spectra of 50 nm thick Nb nanowire arrays on the perfect absorber substrate with a constant period of 600 nm, an Al_2O_3 spacer thickness of 70 nm and different wire widths. It verifies the high absorbing plasmon resonances, which are tunable over a wide spectral range and show 95% absorption up to 1600 nm, which includes the important telecommunication wavelengths. The resonance wavelength is dependent on the wire width and shifts red for larger widths, due to the dipole nature.

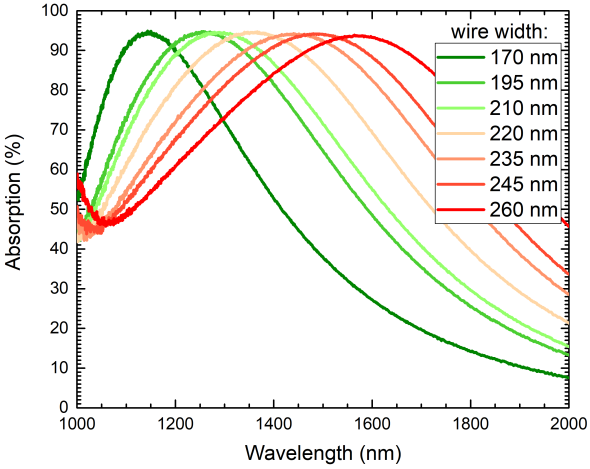

Figure 6.33: Measured absorption spectra of 50 nm thick Nb nanowire arrays on a perfect absorber substrate with a constant period of 600 nm, an Al_2O_3 spacer thickness of 70 nm and different wire widths.

As predicted by the NbN wire arrays, we tested also a nanowire array with a smaller period, expecting a higher absorption due to the denser active area. Therefore, we have fabricated the same wires with a period of 500 nm and present the results in figure 6.34. These measured structures confirm this assumption. The structures reach a slightly higher absorption of $\approx$ 97% over the same spectral range.

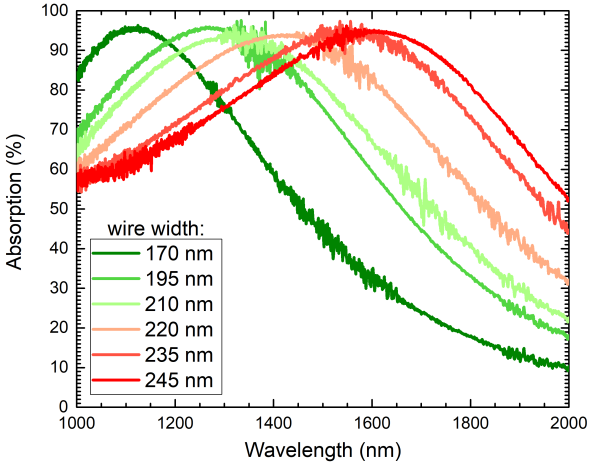

Figure 6.34: Measured absorption spectra of 50 nm thick Nb nanowire arrays on a perfect absorber substrate with a constant period of 500 nm, an Al_2O_3 spacer thickness of 700 nm and different wire widths.

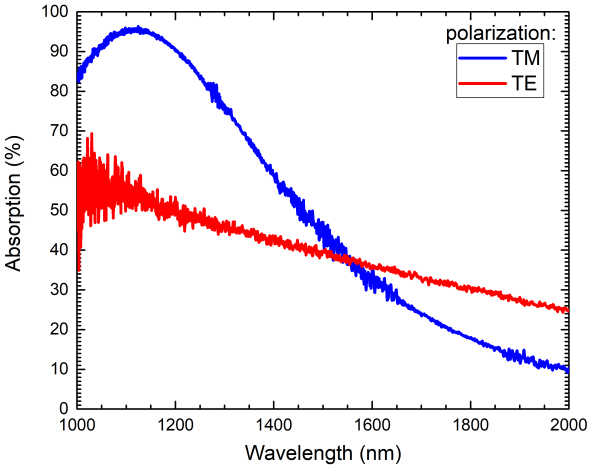

Figure 6.35: Measured absorption spectra of 50 nm thick Nb nanowire arrays on a perfect absorber substrate with a constant period of 500 nm, an Al_2O_3 spacer thickness of 70 nm and a wire width of 170 nm in TM and TE polarization.

To confirm the plasmonic enhancement depicted in figure 6.35 we have measured absorption spectra of the 50 nm thick Nb nanowire arrays with a

constant period of 500 nm, an Al_2O_3 spacer thickness of 70 nm and a wire width of 170 nm in TM and TE polarization. The absorption in TE polarization is again only 50% - 60% and drops even further for higher wavelengths, due to the metallic behavior of the Nb.

The comparison between the measured and simulated data point out a slight mismatch between both. The simulated structures predicts for the lower period around 10% less absorption, which could indicate an error in ellipsometry data. Nevertheless, the position of the resonance can be predicted well and therefore the simulation could still be used as starting point for the sample fabrication.

6.6 NB PERFECT ABSORBER NANOWIRE DETECTORS

This section is analogous to the NbN detector section and describes the performance of our 50 nm thick NbN detector on a perfect absorber substrate with a constant period of 500 nm, an Al_2O_3 spacer thickness of 70 nm and a wire width of 180 nm.

The design of the detector is identical as for the NbN detector and can be seen in figure 6.18 and 6.19. The difference is the active material and therefore we had to adjust the spacer thickness and wire width.

The measurements as well as the characterizations are explained in more detail in the NbN detector section above and the following measurements are carried out in the same way.

6.6.1 *Absorption*

In figure 6.36 we display the measured absorption spectra of our Nb detector structure with an active area of $30 \times 30\ \mu m^2$. The detector exhibits an absorption of over 90% at resonance. The maximum absorption occurs at a wavelength slightly longer than the target wavelength, nevertheless, it still exhibits around 90% absorption. In addition, we can again see a strong enhancement for the TM polarization, compared to the intrinsic absorption, which is around 55% at the target wavelength. This should lead to a clearly distinguishable, polarization-dependent detector response.

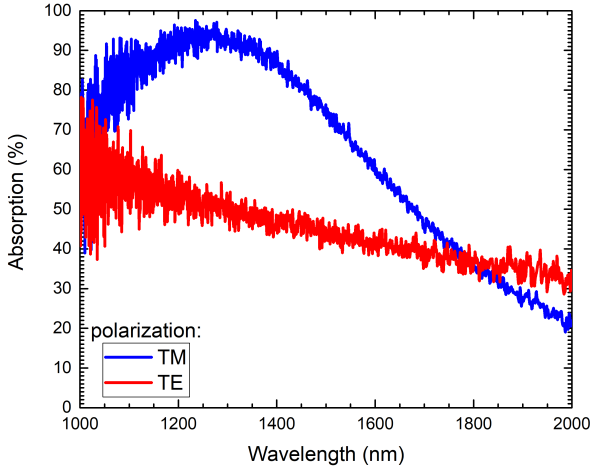

Figure 6.36: Measured absorption spectra of the 50 nm thick NbN detector on a perfect absorber substrate with a constant period of 500 nm, an Al_2O_3 spacer thickness of 70 nm and a wire width of 180 nm.

6.6.2 *Superconducting properties*

To ensure good superconducting properties we have measured the resistance at lower temperature and compared it to the SQUID measurement, to confirm that the fabrication process has not worsen our Nb films and to double check if the detector is functioning and the structure is superconducting.

Figure 4.1 depicts the normalized resistance and normalized magnetic moment of the demonstrated 50 nm thick Nb detector structure. The resistance measurement has been performed with a four-point measurement and the magnetic moment has been measured in the SQUID. Both measurements indicate a critical temperature of around 5 K and show a good match. These measurements verify that our fabrication process does not worsen the quality of our Nb films.

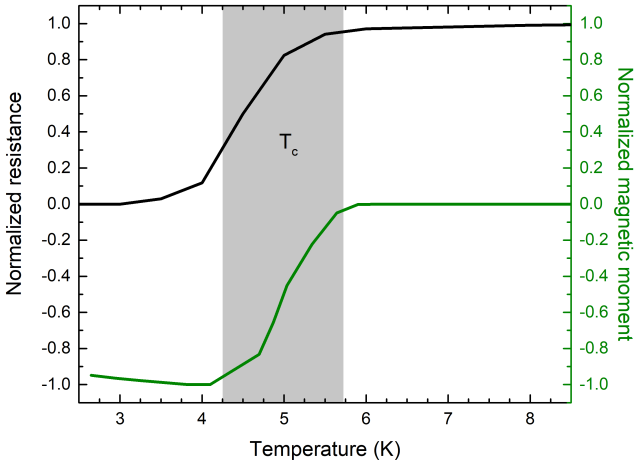

Figure 6.37: Normalized resistance and normalized magnetic moment of the demonstrated 50 nm thick Nb detector structure. The resistance measurement has been performed with a four-point measurement and the magnetic moment has been measured in a SQUID device. Both measurements indicate a critical temperature of ≈ 5 K.

6.6.3 *Detector response*

Before starting to measure the detector response of the 50 nm thick Nb structure for different laser powers we have investigated the maximum response with the same procedure as for the NbN detector. We have illuminated the structure under cryogenic condition at 2.5 K with a laser power of 30 µW and applied different bias currents. The measurement is depicted in figure 6.38. It reveals a maximum response for an applied current of 200 µA. For too low currents we once again notice a smaller response, since the current density is not high enough to break the superconductivity and for higher currents some parts of the structure are no longer superconducting.

The detector response itself, for different temperatures, polarizations and laser powers, is presented in figure 6.39. The detector confirms the expected polarization-dependent response, caused by the different absorption efficiency for TM and TE polarization.

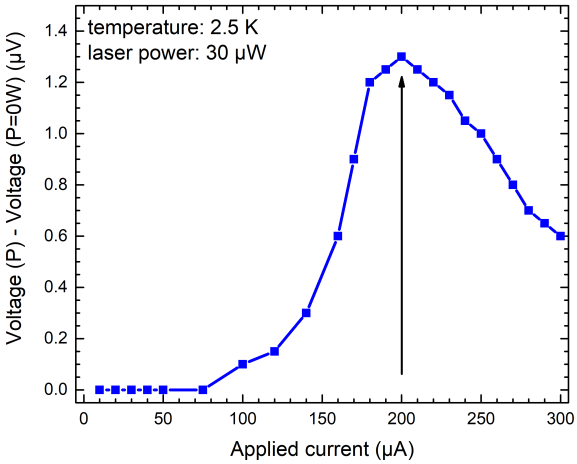

Figure 6.38: Measured detector response of the 50 nm thick Nb detector on a perfect absorber substrate, for different applied currents to find the optimal bias current, at 1140 nm, 2.5 K and with a constant laser power of ≈ 30 µW.

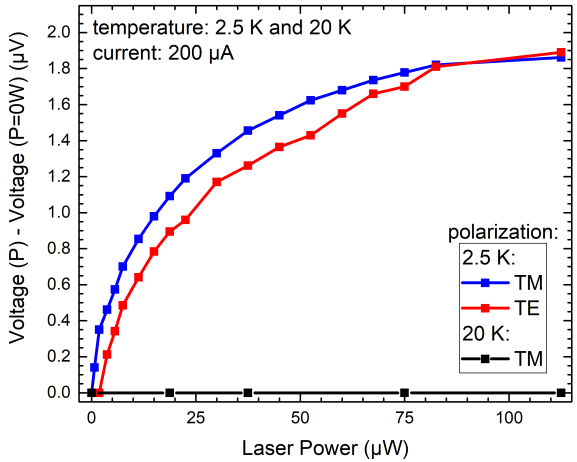

Figure 6.39: Measured detector response of the 50 nm thick Nb detector on a perfect absorber substrate with a wire width of 180 nm, for different for different laser powers, both polarizations and with an optimized applied current of 200 µA.

The detector response is stronger for TM polarization due to higher absorption, leading to a higher detection efficiency. For the high laser powers

the signals become indistinguishable due to the high heat introduction. The measurement at 20 K shows no detector response, as the structure is no longer superconducting in this temperature region, which confirms its working principle.

All in all we have confirmed that our detector principle also works for other materials. The requirements are that the material exhibits plasmonic and superconducting properties and we have validated this statement with the achieved results for NbN and Nb.

6.7 POLARIZATION-INDEPENDENT NBN DETECTORS

The most typical design of SNSPDs is the meander structure, which is similar to the design used for our polarization-dependent detectors. This meander or grid-like design is normally sensitive to the polarization of the incoming light. In our case this effect is even stronger, due to the plasmonic enhancement. In the normal meander detector, the polarization-dependence results from scattering on the grid-like structure. This leads to different detection efficiencies for the different polarizations, even without the use of plasmons [82, 83]. Depending on the application this effect is desired or undesired. Some application need to detect every photon, such as quantum key distribution if the information is encoded in polarization states [84]. And other applications only want to detect photons with a specific polarization.

Another possibility where one needs polarization-independent detectors is for example fiber coupling, using normal single mode fibers, as these do not preserve the polarization of the incoming light, therefore a high absorption and hence detection efficiency is needed for arbitrary polarization.

To overcome the polarization-dependence of the detectors different approaches are used, such as spiral nanostructures [85], double-layer systems [86] and fractal nanostructures [87].

6.7.1 *Different detector designs and polarization definition*

In the following section we have to use an additional criteria to define polarization, as the plasmons will be excited in TM as well as in TE polarization. For the classical polarization-dependent meander detector, we will use the previous definition. For the polarization-independent structures we will

define the polarization with the help of the depicted SEM images and figure 6.40. The light which oscillates vertical, from top to the bottom of the picture, will be defined as TM polarization. The horizontal oscillating light, from left to right of the picture, will be defined as TE polarization. A schematic presentation of the different detector designs and their polarization definition is shown in figure 6.40.

In addition, figure 6.40 reveals the polarization-dependencies of the different detector structures. The classical grid-like meander design exhibits a strong polarization-dependence, due to scattering and the fact that plasmons are only excited in TM polarization. The meander-type and circular polarization-independent detector excite plasmons in both polarization, leading to a strong absorption in every polarization.

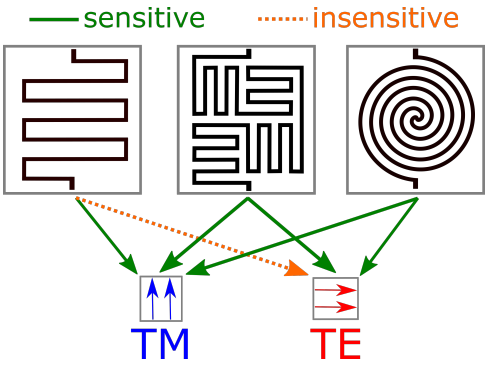

Figure 6.40: Schematic presentation of the different detector designs and their polarization-dependencies [48].

6.7.2 *Meander-type polarization-independent detectors*

The first type of polarization-independent detector we want to introduce is a grid-like structure.

Latices and detector design

The structure consists of a combination of differently arranged small plasmonic latices, as demonstrated in figure 6.41 and 6.42. This arrangement enables the absorption of TM and TE polarized light, as the horizontal latices are able to excite plasmons for TM polarization and the vertical ones excite

TE plasmons. Every other polarization can also be efficiently absorbed, since unpolarized light is a combination of TM and TE light.

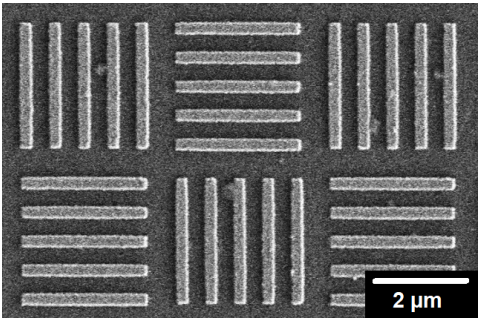

Figure 6.41: SEM image of the test lattice for a meander-type polarization-independent detector structure.

One drawback of this structure is, that each small lattice can only efficiently absorb one polarization. This leads to the fact, that only half of the structure can absorb one polarization, which halves the effective active area of the detector and if a single photon hits the wrong oriented lattice, it will be not efficiently absorbed. This reduces the overall absorption of the whole structure, compared to the classical meander structure, in exchange of the polarization-independence.

Figure 6.41 presents one of the tested nanostructures, where we have used a lattice consisting of five wires before changing the orientation. The structure has been designed in a way that the distance between each nanostructure is equal in all directions. Additional tests with only three wires have also been carried out, revealing that with three wires the absorption slightly drops compared to the lattice with five wires. One explanation could be that the lattice is too small and the electrical field of the plasmon can therefore not interact with enough wires. Five wires on the other hand exhibit good plasmonic properties, as demonstrated in the following part.

In Figure 6.42 a meander-type polarization-independent detector is depicted. The small grids are connected at alternating ends and all small lattices are connected in a row. This allows to form one long continuous wire. To be able to perform a four-point resistance measurement, the detector structure itself is connected to the four large golden contact pads, like the other detectors. The overall active area of the depicted detector is $30 \times 30\ \mu m^2$, whereby halve of it efficiently detects TM and the other halve TE polarized photons.

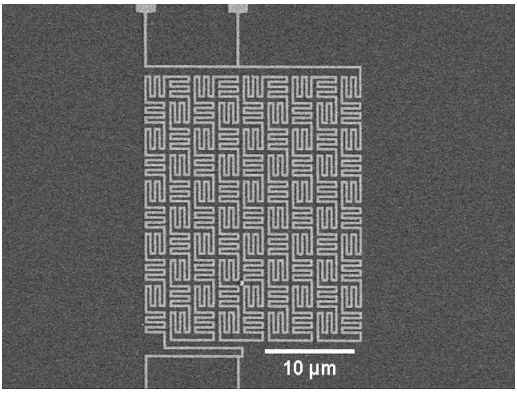

Figure 6.42: SEM image of the active detection area of a finished meander-type polarization-independent detector structure.

Detector absorption

To test the absorption of the fabricated detectors FTIR measurements have been carried out for structures with different wire widths. Figure 6.43 depicts the measured absorption spectra of the 20 nm thick NbN meander-type polarization-independent detector on a perfect absorber substrate with a constant period of 500 nm, an Al_2O_3 spacer thickness of 100 nm and wire widths of 215 and 250 nm.

We notice a maximum absorption of around 80% for both wire widths. This is lower in comparison with the classical detector. The tunability of the resonance wavelength is still possible, but we need wider wires to shift the resonance to higher wavelengths. The resonance of the 250 nm wide structure is shifted red and broader compared the 215 nm structure, which is an expected result, considering the dipole nature of our plasmonic resonances. One explanation for the lower absorption is explained above and could be caused by the fact, that only half of the structure can absorb TM or TE effective.

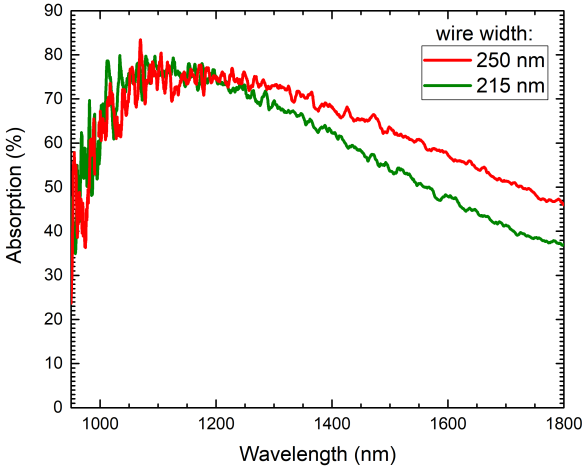

Figure 6.43: Measured absorption spectra of the 20 nm thick NbN meander-type polarization-independent detector on a perfect absorber substrate with a constant period of 500 nm, an Al_2O_3 spacer thickness of 100 nm and wire widths of 215 and 250 nm [48].

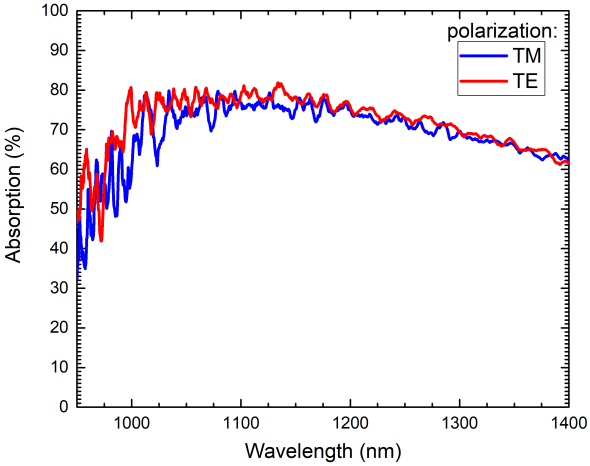

Figure 6.44: Comparison of the measured absorption spectra of the 20 nm thick NbN meander-type detector on a perfect absorber substrate with a constant period of 500 nm, an Al_2O_3 spacer thickness of 100 nm and a wire width of 215 nm for TM and TE polarization [48].

The trade-off for this lower absorption is the polarization-independence. This property is confirmed in figure 6.44, where we have demonstrated the measured absorption spectra of the NbN meander-type detector with a wire width of 215 nm for TM and TE polarization. The measurements reveal an almost identical absorption spectrum for both polarizations. The slight differences can be explained by measurement inaccuracies, since already a small difference in the reference or the measurement position can lead to chances in the results when measuring such small structures.

Detector response

After confirming the polarization-independence of the structure the actual detector response to light incidence was measured.

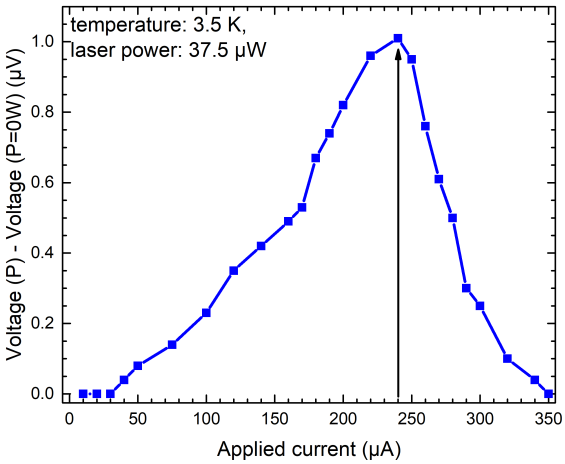

Figure 6.45: Measured detector response of the 20 nm thick NbN meander-type polarization-independent detector on a perfect absorber substrate with a wire width of 250 nm for different applied currents to find the optimal bias current, at 1140 nm, 3.5 K and with a constant laser power of ≈ 37.5 µW.

To make sure the measured response was comparable with previous measurements, the optimized applied bias current has to be determined. The results are shown in figure 6.45, which depicts the measured detector response of the 20 nm thick NbN meander-type polarization-independent detector with a wire width of 250 nm for different applied currents to find

the optimal bias current, at 1140 nm 3.5 K and with a constant laser power of ≈ 37.5 µW. The results reveal a maximum response at 240 µA.

With the optimized applied current the detector response for different polarizations, laser powers and temperatures has been measured. In figure 6.46 we display the detector response of the described detector, at 3.5 K. The shape of the measured response looks similar to the classical detector, but this time there is no difference between TM and TE polarization. This makes sense, since the different responses on the classical detector are caused by the different absorption efficiencies. An additional measurement was carried out at 20 K to confirm the working principle of the detector.

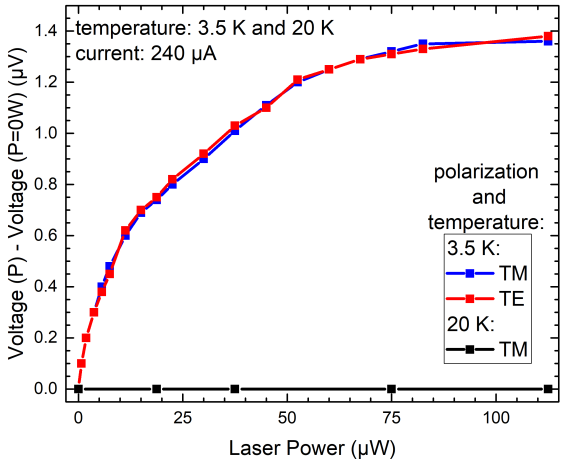

Figure 6.46: Measured detector response of the 20 nm thick NbN meander-type polarization-independent detector on a perfect absorber substrate with a wire width of 250 nm, for different for different laser powers, both polarizations and with an optimized applied current of 240 µA [48].

6.7.3 *Circular polarization-independent detectors*

The second type of polarization-independent detector we want to introduce is a circular structure.

Design

The design of this structure is presented in figure 6.47 and 6.48. The outer part of the detector structure is once again connected to the four large golden contact pads, to enable the four-point resistivity measurement.

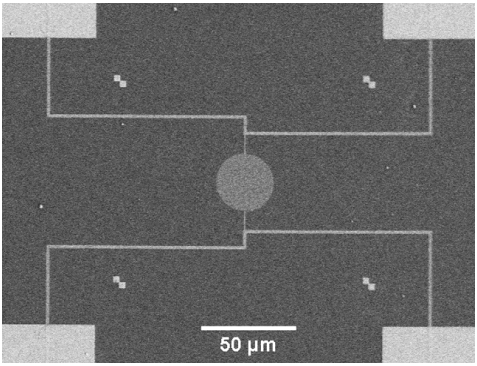

Figure 6.47: SEM image of an entire finished circular polarization-independent detector, with the big Au contact pads in each corner, which are used to carry out a four-point resistivity measurement.

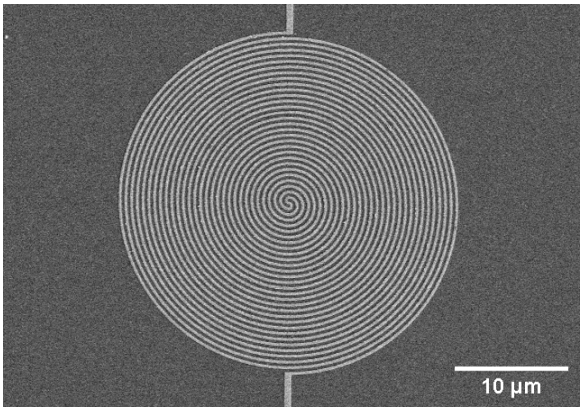

Figure 6.48: SEM image of the active detection area of a finished circular polarization-independent detector structure.

The inner part, depicted in figure 6.48, shows the circular structure, which forms a long continuous wire. This structure consists of slightly shifted semi-circles to achieve the one long wire width an active area of $\approx 30 \times 30\ \mu m^2$.

The idea behind this structure is that a perfect circle exhibits no polarization-dependence due to its perfect rotational symmetry. This way it can form a perfect plasmonic latices with a given wire width and period in each direction.

These reasons should lead to a higher absorption efficiency. However, it is important to align the detector perfectly in the middle of the laser beam, as the circular structure is only in the middle a perfect lattice in every direction. It is preferable to focus the light on the structure, to ensure this condition is fulfilled. Focusing the light is possible thanks to the angle of incidence independence of the plasmonic perfect absorber structure. The focusing and the alignment problem could be addressed by utilizing 3D-printed micro structures, such as fiber lenses and fiber chucks. More examples and advantages are discussed in chapter 7.

Absorption

The absorption of the circular polarization-independent detector structures are demonstrated in figure 6.49, where we display the measured absorption spectra of circular detectors with a constant period of 500 nm, an Al_2O_3 spacer thickness of 100 nm and different wire widths.

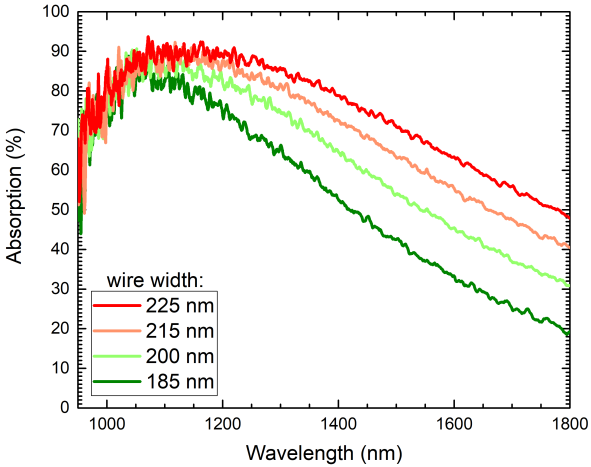

Figure 6.49: Measured absorption spectra of the 20 nm thick NbN circular detector on a perfect absorber substrate with a constant period of 500 nm, an Al_2O_3 spacer thickness of 100 nm and different wire widths [48].

The maximum absorption is around 90%, compared to the grid-like polarization-independent structure it performs better, but in comparison to the classical structure it is still slightly worse. Possible explanations have been already discussed above. In addition, the detector structure is not a perfect circle, it consists of shifted semicircles, leading to a small symmetry break.

Nevertheless, the structure exhibits good plasmonic properties and high absorption. Moreover, this structure shows a better tunability compared to the grid like structure, as it shifts nicely red for wider wire widths.

To confirm the polarization-independence, the measured absorption spectra of the NbN circular detector with a constant period of 500 nm, an Al_2O_3 spacer thickness of 100 nm and a wire width of 215 nm for TM and TE polarization is presented in figure 6.50. It reveals two almost identical absorption curves, which verify the polarization-independence and the high absorption of 90%.

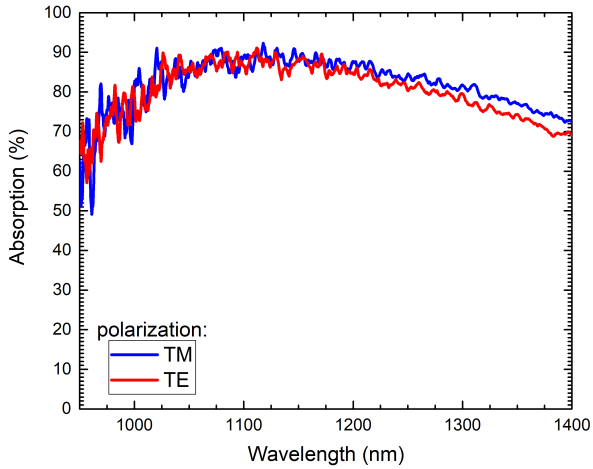

Figure 6.50: Comparison of the measured absorption spectra of the 20 nm thick NbN circular detector on a perfect absorber substrate with a constant period of 500 nm, an Al_2O_3 spacer thickness of 100 nm and wire width of 215 nm for TM and TE polarization [48].

Detector response

Similar as for the other detectors, we have to determine the optimal applied bias current for the circular detector structure, before measuring the detector response for different laser powers and polarizations. Figure 6.51 depicts the detector response of the 20 nm thick NbN circular polarization-independent detector with a wire width of 215 nm for different applied currents to find the optimal bias current, at 1140 nm, 3.5 K and with a constant laser power of ≈ 50 µW.

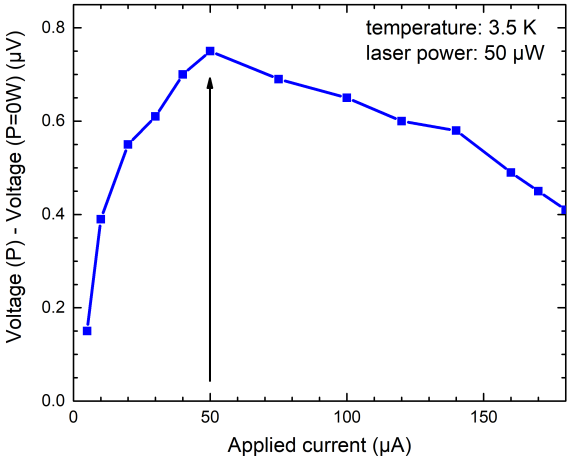

Figure 6.51: Measured detector response of the 20 nm thick NbN circular polarization-independent detector on a perfect absorber substrate with a wire width of 215 nm, for different applied currents to find the optimal bias current, at 1140 nm, 3.5 K and with a constant laser power of ≈ 50 µW.

The detector response for both polarizations and different temperatures is displayed in figure 6.52. It presents the measured response for the circular polarization-independent detector with the optimized applied current of 50 µA. As for the other polarization-independent detector structure, there is no clear difference in the response for the different polarizations, confirming its polarization-independence. The detector at 20 K shows no signal due to not being superconducting.

These results show that the circular structure is superior to the grid like structure, as it exhibits the same polarization-independence, but a higher absorption efficiency.

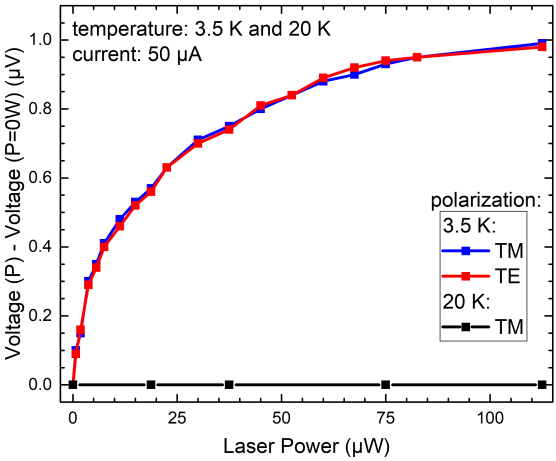

Figure 6.52: Measured detector response of the 20 nm thick NbN circular polarization-independent detector on a perfect absorber substrate with a wire width of 250 nm, for different for different laser powers and both polarizations. With an optimized applied current of 50 µA [48].

All in all we have demonstrated two different polarization-independent NbN detectors, one with a high absorption of 90% and confirmed their polarization-independence via FTIR measurements, as well as with their response to an external laser source under cryogenic conditions.

6.8 COMPARISON OF THE DIFFERENT DETECTOR DESIGNS

To compare the performance of the three different NbN detector structures we directly compare the absorption and normalized detector response in this section.

6.8.1 *Absorption*

The direct comparison of the TM absorption spectra of all three discussed NbN detectors, is depicted in figure 6.53. We notice that the classical meander structure exhibits the highest absorption with over 95%, followed by the circular polarization-independent detector structure with around 90% and in the end the grid-like or meander-type polarization-independent detector with around 80%.

The fact that the classical lattice structure has the highest absorption is most likely it caused by a more optimized structure. In addition, it is almost identical to a perfect plamonic infinite lattice, since the structure, with its active area of 30×30 µm^2, can be considered large compared to the wavefront of the incoming light. The circular structure has a small shift between the semicircles to form the continuous wire, which breaks it symmetry slightly and the grid-like polarization-independent structure halves its effective plasmonic active area, due to the perpendicular wires.

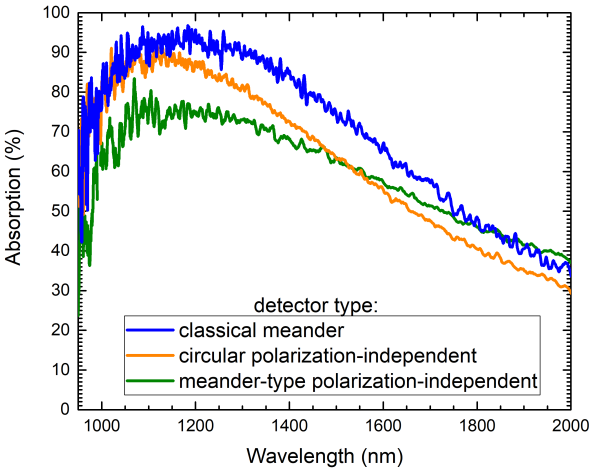

Figure 6.53: Direct comparison of the absorption spectra of all three discussed NbN detectors in TM polarization[47, 48].

All structures exhibit the ability to tune the resonance wavelength to higher and lower wavelengths by adjusting their wire widths, but the tunability is stronger for the classical and circular design than for the grid-like structure.

6.8.2 *Detector response*

In figure 6.54 we present the direct comparison of the normalized detector response of all three discussed NbN detectors in TM polarization. We normalized the responses of the three different detectors to be able to compare them directly, since they all had different resistances due to their different lengths. Hereby the normalized results are obtained by dividing all data

points of the response measurement by the highest measured voltage drop, which is usually the data point with the highest laser power.

By comparing the normalized responses we notice that the classical detector is the structure with the biggest slope, followed by the circular structure, which has the second highest and the grid-like structure.

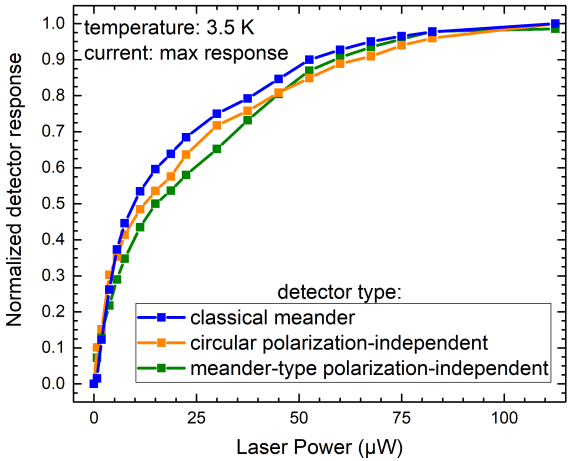

Figure 6.54: Direct comparison of the normalized detector response of all three discussed NbN detectors, in TM polarization[47, 48].

The higher slope can be interpreted as a higher detection efficiency, which we have already observed by the classical meander detector, when we compared the responses for TM and TE polarization. In figure 6.54 we are able to do this again due to the normalization. This means we can observe the detection efficiency, and hence the absorption directly in the detector response. By comparing the order of the response slopes with the order of the highest absorption, both orders match. Telling us that the classical meander, in TM polarization, has the highest detection efficiency, followed by the circular structure.

All in all we have demonstrated that the classical meander design shows the highest detection efficiency, but only for TM polarization. For unpolarized light, on the other hand, the circular detector structures should exhibit the best detection efficiency, since the absorption of the classical detector drops for unpolarized light to under 80% at a wavelength of 1140 nm, which is the mean between the absorption for TM and TE photons, see figure 6.21.

6.9 NBTIN PERFECT ABSORBERS FOR THE VISIBLE SPECTRAL RANGE

The third material which we have used for our detector structures is NbTiN, which is provided by collaborators from Munich. The difference to the previous structures is that the target wavelength for this structures is in the visible spectral range. In this section we present the corresponding absorption curves for different measured nanowire arrays and their simulations.

The target wavelength for this structures is 780 nm. This wavelength has been requested by our collaborators, as they have already established a measurement setup for this wavelength to test their own NbTiN SNSPDs. Our part of the collaboration is to fabricate the plasmonic enhanced detector structures, which will later be measured under cryogenic conditions and analyzed by them. With these measurements we want to confirm that the detection efficiency of SNSPDs could be enhanced by utilizing plasmonic resonances and directly compare them to SNSPDs with the same material but without plasmonic enhancement.

In the beginning we have carried out some simulations, similar as for the other structures, to find the optimized geometric parameters before starting the fabrication of the nanowire arrays. The finished arrays have been measured with a grating spectrometer, which is connected to a microscope and shutter, to be able to measure only the $100 \times 100\ \mu m^2$ nanostructure. The spectrometer itself consists of a grating monochromator and a 2D detector camera for the visible spectral range.

For this structures only 10 nm thick NbTiN was used, as thinner films provide better properties for SNSPDs and the spacer was switched to SiO_2, as our collaborators already used a SiO_2 cavity for their own structures.

In figure 6.55 we present the measured absorption spectra of 10 nm thick NbTiN nanowire arrays on a perfect absorber substrate with a constant period of 300 nm, a SiO_2 spacer thickness of 90 nm and different wire widths in TM polarization. The measurement reveals broadband and highly absorbing resonances with over 97% absorption for arrays with wire widths over 150 nm.

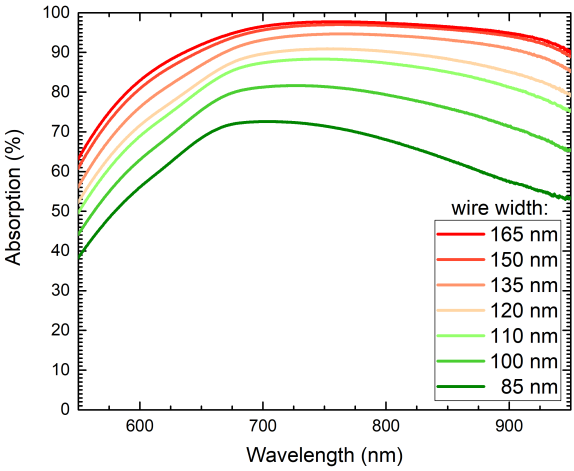

Figure 6.55: Measured absorption spectra of 10 nm thick NbTiN nanowire arrays on a perfect absorber substrate with a constant period of 300 nm, a SiO_2 spacer thickness of 90 nm and different wire widths in TM polarization.

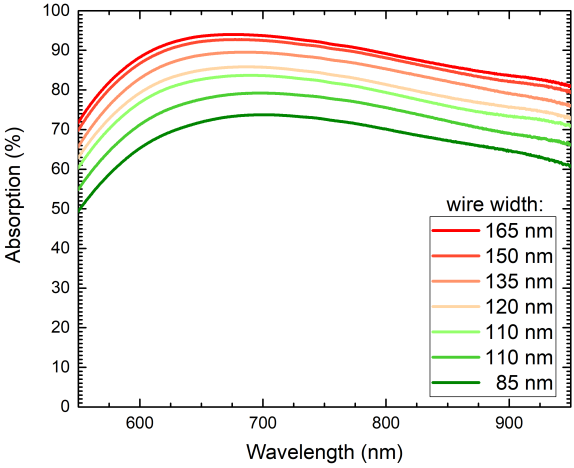

Figure 6.56: Measured absorption spectra of 10 nm thick NbTiN nanowire arrays on a perfect absorber substrate with a constant period of 300 nm, a SiO_2 spacer thickness of 90 nm and different wire widths in TE polarization.

Moreover, we notice a weak tunability of the resonance and a strong dependence on the fill factor, where more dense filled arrays exhibit a higher absorption. This can be explained by the fact that visible photons provide

more energy than IR photons and hence are more likely to be absorbed on their own. This also explains the weak absorption enhancement, since the material itself exhibits a strong intrinsic absorption in the visible spectral range.

Nevertheless, the comparison with the measured TE absorption spectra of the same arrays, which is depicted in figure 6.56, confirms a plasmonic enhancement, as the absorption in TM polarization is higher than in TE polarization.

Furthermore, we observe that the smaller thickness of the NbTiN leads to a strong blue shift of the resonance, which makes it suitable for the visible spectra range. However, it is important to notice that a plasmon needs a certain space to be able to form itself, which makes it difficult to reduce the film thickness even further, as the weak tunability could be already a sign that we are with 10 nm near or at that limit.

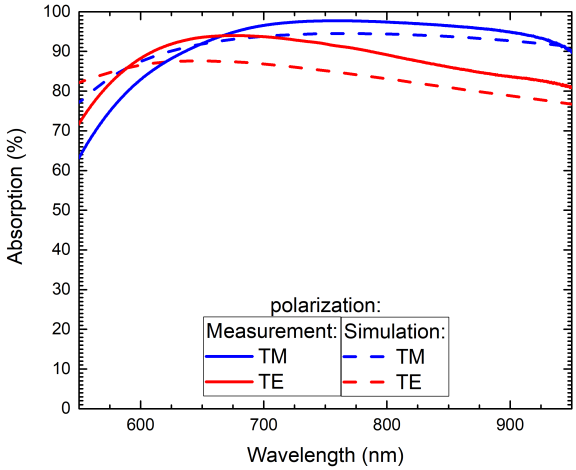

Figure 6.57: Direct comparison of simulated and measured absorption spectra of 10 nm thick NbTiN nanowire array on a perfect absorber substrate with a constant period of 300 nm, a SiO_2 spacer thickness of 90 nm in TM and TE polarization.

Figure 6.57 displays the direct comparison of simulated and measured absorption spectra of a 10 nm thick NbTiN nanowire array with a constant period of 300 nm, a SiO_2 spacer thickness of 90 nm in TM and TE

polarization. By comparing TM and TE polarization one can clearly see the absorption enhancement at the target wavelength of 780 nm. In addition, we confirm a good agreement between simulation and measurement, regarding the resonance position. The measurement exhibits a higher absorption, which is typical the other way around, due to fabrication imperfections.

The measured absorption spectra of 10 nm thick NbTiN nanowire arrays on a perfect absorber substrate with a constant period of 270 nm, a SiO_2 spacer thickness of 90 nm and different wire widths in TM polarization is depicted in figure 6.58. This is the second array set we have fabricated, as the simulations have also predicted high absorbing plasmon resonances for these structures. The measurement confirms these resonances and reveals an absorption of over 95%.

One could expect a higher absorption for the structures with a period of only 270 nm than with a period of 300 nm, but the fabrication for structures with these small periods is difficult. Also there has to be a certain amount of space between each wire, to prevent the tunneling or hopping of the electron between each separate wire. In addition, this confirms, that still we have plasmonic effects, since the structure with the lower fill factor exhibits an higher absorption.

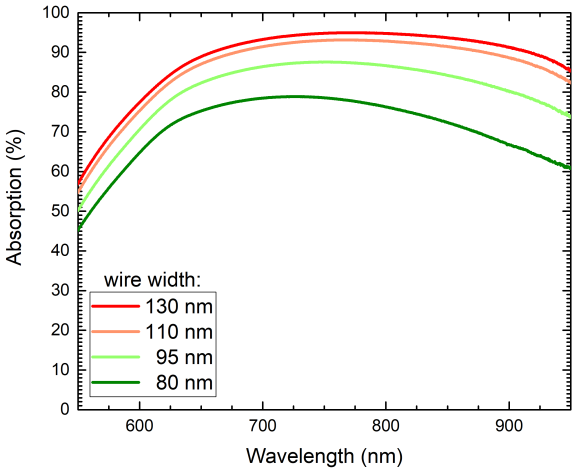

Figure 6.58: Measured absorption spectra of 10 nm thick NbTiN nanowire arrays on a perfect absorber substrate with a constant period of 270 nm, a SiO_2 spacer thickness of 90 nm and different wire widths in TM polarization.

In figure 6.59 we present the SEM picture of the active detection area of a finished NbTiN detector structure with the design used by our Munich collaborators. These detectors have an active area of $\approx 10 \times 10\ \mu m^2$. The foundation of their detectors is also a nanowire array with connections at the end to form one continuous nanowire.

The difference between our structures and their structures is the fact that the connection at the end of the individual wires consist of semicircles to avoid current crouching at the edges. Moreover, the two large wires which are used to connect the structure are impedance matched to 50 Ω. These features get important when one wants to optimize the structures even further regarding time resolution measurements, such as the timing jitter and recovery time.

Furthermore, there are dummy wires around the structure to enhance the absorption of the structure and to provide better boundary conditions. This could be used for our ultra-small detectors to enable even smaller detector structures without losing absorption efficiency, due to too less wires or bad boundary conditions.

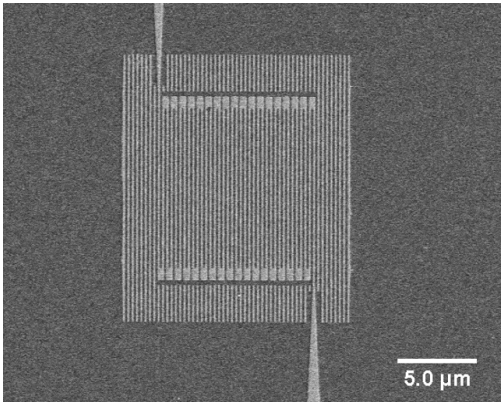

Figure 6.59: SEM image of the active detection area of a finished NbTiN detector structure with the design used by our Munich collaborators.

Until this point we were not able to fabricate a working SNSPD out of NbTiN, as some process during the fabrication destroys the superconducting properies of the ultra thin 10 nm film. One possible explanation could be that the thin NbTiN film oxidizes during the spin-coating process, as we

have to bake the photoresist at 150 °C for one minute. Therefore, we will try different fabrication methods to overcome this problem.

Nevertheless, we are optimistic that the enhanced absorption will lead to a higher detection efficiency, since we have already confirmed this with our own detectors, as shown for our Nb and NbN structures.

All in all we have demonstrated the absorption enhancement in NbTiN nanostructures and reached over 97% absorption, which theoretically should lead to an increased detection efficiency of the NbTiN SNSPDs.

7

COMBINATION OF ULTRA-SMALL PLASMONIC PHOTODETORS AND 3D-NANOPRINTING APPLICATIONS

This chapter introduces the combination of our plasmonic photodetectors and 3D-nanoprinting applications. 3D-printed nanostructures are already used for various quantum technologies, such as fiber-coupling of quantum light sources [88–90] or optical tweezers [91]. In addition, there are several different photoresists with varying properties [92], which ensure the functionality for different applications and wavelengths.

These 3D-printed and micrometer-sized structures are produced utilizing a two-photon polymerization process. A focused laser beam enables us hereby to write the desired structure directly into a photoresist. As we are using a negative photoresist, which polymerizes after laser exposure and a development process, we are able to fabricate small 3D-structures, such as nano-lenses. By applying the photoresist on the end of an optical fiber, we are for example able to produce 3D-printed nano-lenses on top of fibers. The smallest possible part of a structure is hereby dependent on the focal spot of the laser and is a so-called voxel. In our institute we are using a commercially available 3D-printer (Nanoscribe Professional GT) from Nanoscribe. The laser source is a pulsed laser with a wavelength of 780 nm and a pulse energy of 2.25 nJ. These parameters can achieve voxel sizes of only 100 nm [91].

7.1 ADVANTAGES OF 3D-PRINTING AND FIBER INTEGRATION

In our case we want to couple our detector structures to optical fibers, which yields several advantages. One obvious advantage is the fact that the whole setup could be fiber-coupled, avoiding losses through additional optics and alignment issues. Furthermore, the established fiber networks already con-

sist of optical fibers, giving our detectors a great compatibility to the already established infrastructures.

The other advantage is the utilizing of high-NA nano-lenses printed on the end facet of optical fibers. These lenses enable small spot sizes and therefore ultra-small detector structures, and hence leading to a smaller kinetic inductance and shorter recovery times, as explained in equation (3.11). This is possible due to the angle of incidence independence of the perfect absorber substrate, compare figure 6.13, and the high absorbing cross-section of plasmonic resonances, which preserve the high absorption even under these conditions.

Such small detectors are not possible without focusing objectives, as the core diameter of typical fibers in the infrared spectral range are around 6 - 8 µm, leading to a minimum active area of at least 6×6 µm^2. In this thesis we demonstrate a detector with an active area of only 3×3 µm^2. This decreases the active area by a factor of 4, and the resulting detector should therefore have a four times faster recovery time. Theoretically detectors with an active area of only 1×1 µm^2 are also possible, since we have shown that the accuracy of our 3D-printed nanostructures is below 1 µm [89]. To maintain the high absorption for even these small structures, dummy wires could be placed around the actual detector, as demonstrated for the NbTiN structures in figure 6.59.

7.2 SAMPLE DESIGN

In this section the different sample designs will be discussed and analyzed, since we had to modify the design slightly to ensure an accurate alignment of the 3D-printed structures and the durability of the whole sample.

7.2.1 *First fiber detector design*

The first design we used was a standard detector structure, with additional big quadratic alignment markers to align the 3D-printed fiber chuck on top of the nanostructure. Figure 7.1 depicts a SEM image of this new design. The detector is hereby exactly in the middle of these new alignment markers.

The mentioned fiber chuck on top of the bonded sample is depicted in figure 7.2. The bare fiber is later inserted in the middle hole of the chuck and transmits the laser light directly to the detector.

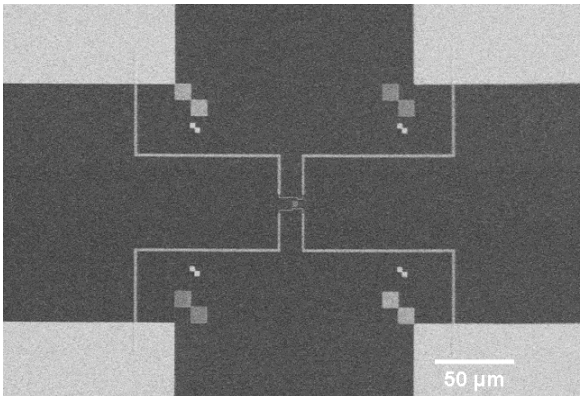

Figure 7.1: SEM image of a detector designed for fiber coupling with additional big quadratic alignment markers.

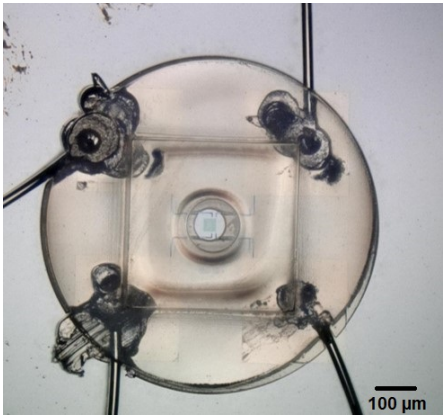

Figure 7.2: Picture of a bonded detector with a fiber chuck on top.

A picture of the mounted sample is presented in figure 7.3. To ensure a fixed position of the fiber inside the chuck, the two parts a glued together with UV-glue after alignment. The picture clearly shows the bond wires, UV-glue and fiber on top of a detector structure.

Figure 7.3: Picture of the first fiber-coupled detector design mounted on the previous sample holder and contacted with the four copper wires. One can clearly notice the optical fiber on top of the detector structure.

Unfortunately, there have been a few issues with this design and we had to slightly redesign the contacts of the detector. While cooling down the sample in the cryostat the bonded electrical contacts often have lost contact to the detector. This problem has been most likely caused by thermal stress due to different thermal expansion coefficients of the different materials.

7.2.2 *Improved fiber detector design*

After analyzing the mentioned issues, we redesigned the detector structure. In the new design we extended the contact wires on the Nb/NbN structure. With these extensions the Au contact pads are no longer under the 3D-printed fiber chuck and UV-glue. This ensures that thermal stress can no longer pull off the bonding wires. The inner parts of the detector are the same as before, since we still need the alignment markers for the fiber chuck.

A SEM image of the new detector design with the extended contacts is displayed in figure 7.4. In addition, figure 7.5 displays a picture of a detector with the new design and confirms that the Au contact pads are no longer covered by the fiber chuck.

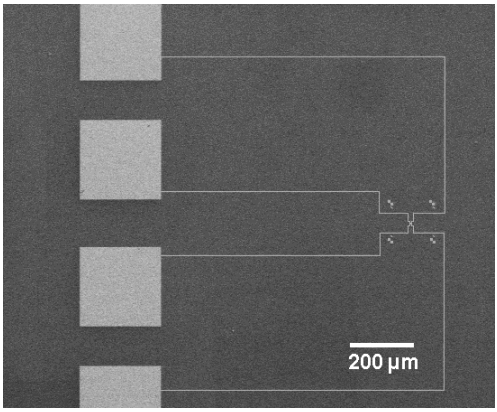

Figure 7.4: SEM image of the improved detector designed for fiber coupling with extended contacts.

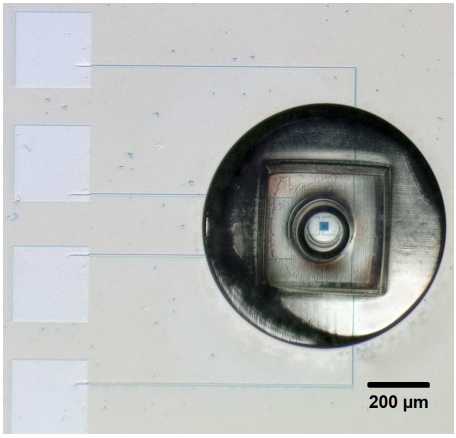

Figure 7.5: Picture of a new detector with extended contacts and a fiber chuck on top. The Au contacts are no longer covered by the fiber chuck.

This new design turned out to be very robust, since we have cooled down different samples several times without breaking parts of it or loosing contact to one of the Au pads.

7.2.3 *Ultra-small detectors and 3D fiber-lenses*

After successfully testing a 30×30 µm^2 fiber coupled Nb detector structure with just a cleaved and bare fiber inserted into the chuck, we have tested detectors with smaller active areas.

As discussed before, to be able to efficiently use smaller active areas with dimensions below the diameter of IR optical fibers, we need to focus the incoming light. This is achieved by the use of fiber-lenses which are directly printed on the end facet of the used optical fibers. With these lenses we are able to reduce the diameter of the focal spot of our incoming light to around 1 µm. This allows us to fabricate detectors with active areas of only 3×3 µm^2, or maybe even 1×1 µm^2, without losing absorption efficiency, due to the plasmonic perfect absorber principle. A picture of such a 3D-printed micro-lens at the end of an optical fiber is depicted in figure 7.6.

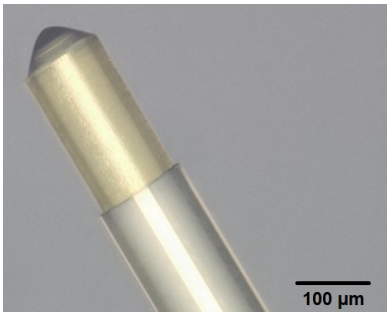

Figure 7.6: Picture of a 3D-printed micro-lens on at the end of an optical fiber.

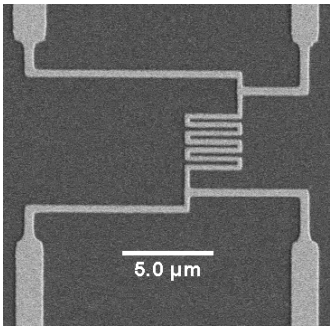

Figure 7.7: SEM image of a detector design with an active area of 3×3 µm^2 for fiber-coupling with a fiber-lens.

In figure 7.7 we present the SEM image of such a Nb detector with an active area of only $3 \times 3\ \mu m^2$. The geometric dimensions and fundamental design of the small Nb detector are identical as for the big ones, which have been discussed in the previous chapter. This ultra-small detector, with the new Au pads is later fiber-coupled and measured to confirm its working principle.

7.3 FIBER-COUPLED MEASUREMENT SETUP

To enable the measurements of the fiber-coupled detectors we have had to modify our sample holder. For the first measurements we have build a fiber leadthrough at the top of the sample holder. Here the important and challenging part is to ensure the vacuum tightness of this component. This has been realized by squeezing a plastic part with a small hole for the fiber in the middle, which will be pressed against the fiber and therefore seal the leadthrough. The sealing of the leadthrough is very important, otherwise air can be sucked into the cryostat and freeze inside.

An additional part we have added to the sample holder is a leadthrough for a coaxial cable, as for time-dependent measurements a coaxial cable is needed due to high losses and high noise of normal cables at high frequencies. The coaxial cable leadthrough was realized in a similar same way as for the fiber by utilizing squeezing o-rings, as it has to satisfy the same criteria.

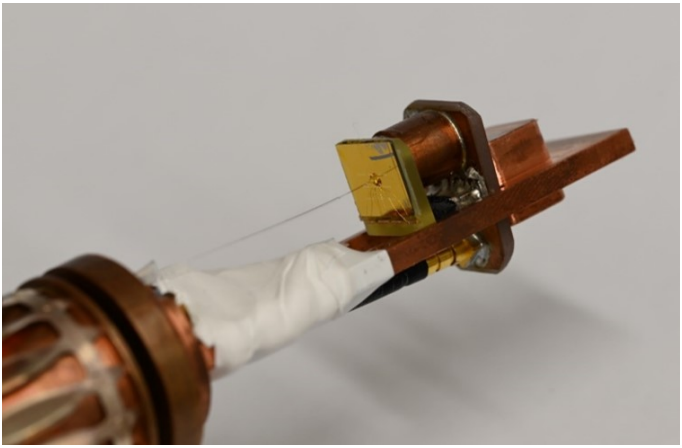

Figure 7.8: Picture of the sample holder with a coaxial cable and an attached fiber-coupled sample.

For the bottom part of the sample holder we had to design a circuit board which connects our sample chip carrier with the coaxial cable. This new lower part is depicted in figure 7.8, where the finished fiber-coupled sample together with the circuit board and the coaxial cable is presented.

After inserting the sample holder with the mounted sample in the cryostat, we ensure the functionality of the fiber and its connection with a fiber-coupled laser in the visible spectral range. A picture of the illuminated sample inside the cryostat is displayed in figure 7.9.

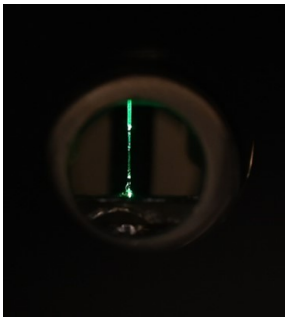

Figure 7.9: Picture of the sample with an attached fiber-coupled sample in the cryostat, a green fiber-coupled laser is used to demonstrate and confirm the functionality of the fiber.

As mentioned, the ability to perform time-resolved measurements requires coaxial cables, but to prevent the applied DC current to reach the amplifier, we installed a bias-tee in our setup. The bias-tee is combination of a coil, which blocks the high frequency signal of the sample and a capacitor, which blocks the DC current and lets the sample signal transmit. The amplifier is needed to amplify the small voltage drop of the sample, since the signal of only one photon is quite small. In the end, the signal is processed in a digital lock-in amplifier, which is triggered with the laser pulse signal and could also be used as oscilloscope. The lock-in is needed, since the sample signal is small and the different connections and the 2 m long coaxial cable introduce noise in our system.

The use of two variable fiber attenuators (Thorlabs VOA1064-FC) enable us to reduce the power of the new pulsed laser. The power is reduced to a point, at which every pulse consists theoretically in average only photon numbers in the order of a single photons [93]. In addition, the attenuators allow us to have a fully fiber-coupled setup, which gives us complete knowledge over all

losses in the setup by measuring the individual losses of the different fiber-couplers and attenuators. This knowledge is used to calculate and estimate the number of photons per pulse. The pulsed laser has a wavelength 1060 nm, a variable repetition rate f_{rep} between 1 – 100 MHz, a ns pulse width and a variable average power P_{av} between µW up to mW.

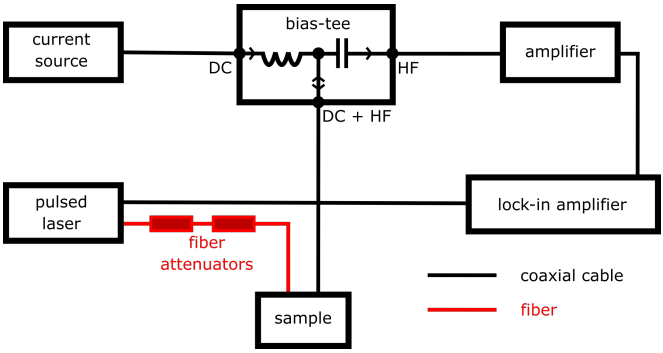

Figure 7.10: Schematic sketch of the new fiber-coupled setup. The new setup uses coaxial cables and a pulsed laser to enable time-resolved and lock-in measurements.

7.4 FIBER-COUPLED DETECTOR RESPONSES

In this section we discuss the measured results with the new setup of a fiber-coupled 50 nm thick Nb detector with a wire width of around 190 nm, a 70 nm thick Al_2O_3 spacer and an active area of only $3 \times 3\ \mu m^2$.

As explained before, we have calculated the actual number of photons hitting the sample with the help of the photon energy E_{photon}, the wavelength λ and the pulse energy E_{pulse}. The pulse energy can be determined with the repetition rate f_{rep}, the average power P_{av} and the applied attenuation and losses. The resulting photon number can than be calculated with

$$N_{photons/pulse} = \frac{E_{pulse}}{E_{photon}} = \frac{P_{av} \cdot \lambda}{f_{rep} \cdot h \cdot c}. \tag{7.1}$$

In figure 7.11 we depict the measured fiber-coupled Nb detector responses for different setup variations in dependence of the photons per pulse. At first a measurement without the fiber attenuators has been carried out, instead we have used a free space setup with filter plates and coupled the laser

afterwards again into a single mode fiber. As amplifier we have used an old model from Agilent (8447D) with a gain of 25 dB. This measurement has yielded the worst results compared to the other setups, as the filters could introduce cavity effects and due to the in-coupling into the fiber a precise assumption of the photon number was difficult.

The second measurement has yielded better results and has been performed with the fiber attenuators and the same amplifier. This time we have been able to repeatable measure pulses with estimated under 100 photons per pulse. The enhanced performance results most likely from the fact that the whole setup was now fiber-coupled and therefore more controllable and precise.

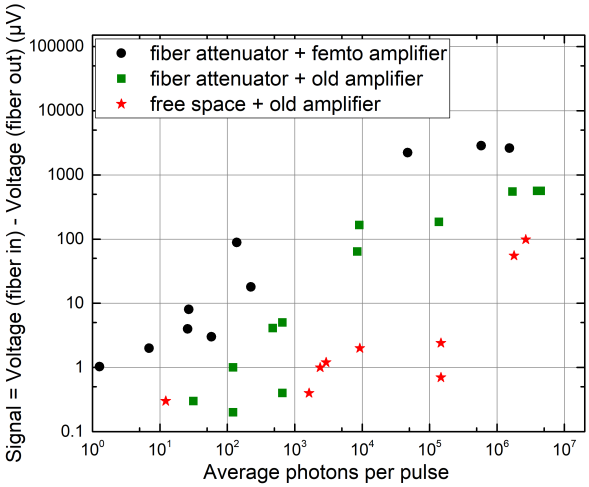

Figure 7.11: Measured fiber-coupled detector responses with different setup variations of a 3×3 µm^2 and 50 nm thick Nb detector, with a wire width of around 190 nm and a 70 nm thick Al_2O_3 spacer.

The third measurements has also been performed with the fiber attenuators, but this time we used a new low noise amplifier from Femto (HVA-200M-40-B, Voltage Amplifier) with a switchable gain between 20 and 40 dB. With the new amplifier and the lock-in we have been able to measure pulses containing in average only single-digit photon numbers. This result could be repeated several times. This is an important step towards single photon detection, since it shows that already pulses with photon numbers on the

order of single photons cause a change in our detector. However, due to the poor signal-to-noise ratio this is not possible without lock-in at the moment.

To ensure the correctness and accuracy of the second and third measurement we explain the measuring process in more detail. The results depicted in figure 7.11 and 7.12 are the subtraction of the measured voltage drops on the detector structure, once with the fiber coupled in and coupled out. This was done to prevent the measuring of any unwanted or artificial signal, since this way also the laser could keep running, ensuring the same conditions for all measurement, expect that one time we have send photons through the fiber onto the detector and the other time not. In addition each measurement was repated several times

Since the power of one single photon could not be measured with an optical power meter, we have measured and characterized each part of the optical setup separately, including the losses in the fiber and couplers, to ensure an accurate calculation of the number of photons per pulse. For the repetitions rate we used 10 MHz for the second and 25 - 40 MHz for the third measurement, to ensure to stay below the recovery time of the detector, which we expected to be in the low nanoseconds or picoseconds regime as stated in [48].

All the described measurement have been carried out with the same sample and with the lock-in amplifier, since due to the low signal-to-noise ratio the measurement without the lock-in was not possible. Therefore, time-related measurements of our ultra-small detector have not been possible.

On different advantage of the lock-in amplifier is the filtering of uncorrelated signal parts. To ensure that we are indeed measure the signal caused by our laser source since additional noise and features, which are not correlated with the trigger of the laser are filtered out by the lock-in amplifier. This in combination with our measurement method ensures that we are able to neglect the dark counts in our results. First, the dark counts do not correlate with the trigger signal of the laser. Second, since we use the voltage difference between plugged in and plugged out fiber as signal, dark counts could lead to an overall bigger signal in both cases, since the could cause a rise of the overall voltage drop, due to breaking the super-

conductivity in some parts of the wire. A explicit determination of the dark counts is not possible in our setup, due to the poor signal-to-noise ratio. Since dark counts are also treated like white noise and therefore perish there.

By comparing the shape of the measurements with the fiber attenuators we realize, that they look similar and are basically just shifted in the y-direction, due to the use of the different amplifiers. In addition, for a certain number of photons per pulse the signals start to saturate, which could be interpreted that at this point the whole structure is not superconducting anymore and therefore, no further photons could be detected.

In figure 7.12 we present only the measurement with the femto amplifier to analyze it in more detail. We performed a detailed error calculation in which we analyzed and calculated the various measurement uncertainties of the different setup components. For example, we measured the different fiber couplers and the stability of the laser power, a detailed description and calculation can be found in the appendix B and have been calculated with the Gaussian error propagation law [94]. The result was a percentage error of 12.81%, which is represented by x-error bars. In addition, it is important to note that we cannot measure half photons, this number is obtained by calculating the photon number with the equation (7.1). Furthermore, it should be noted that we have to assume a Pisson distribution for photons. However, the expected value and variance of this distribution depends on the originally calculated number of events, in our case the number of photons per pulse and is therefore still in the range of single photons. Even with these errors taken into account, our calculated detectable photon numbers are still in the range of single photons.

Since the data points before the saturation exhibit a linear behavior in the double logarithmic plot we are able to fit a power law function with the form of

$$\text{Signal} = a \cdot (\text{Averagephotons per pulse})^b$$

to it. By assuming that a pulse containing average only one photon gives out a signal with approximately 1 µV, a detected pulse with two photons should give a signal of around 2 µV and so on. Since this is a lock-in measurement, the measured signal is averaged over several measurements. This allows us to interpret b as the detection efficiency of our detector, where a perfect detector with 100% detection efficiency should yield $b = 1$. In our case we obtain $b = 0.8$, which gives an estimated detection efficiency of 80% for our

detectors. *a* is in our case just a scaling factor and determined by the used gain of the amplifiers.

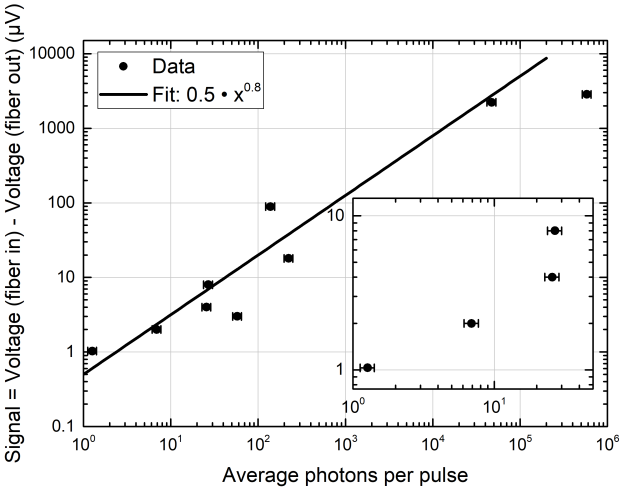

Figure 7.12: Measured fiber-coupled detector responses with error bars for the photon per pulse with fiber attenuators and the new femto amplifier of a 3×3 µm^2 and 50 nm thick Nb detector with a wire width of around 190 nm and a 70 nm thick Al_2O_3 spacer.

In the previous chapter we have stated that our detectors show an absorption efficiency of almost 100%, so how could the detection efficiency be only 80%? The answer to this question is the fact that almost 100% absorption is only achieved in TM polarization, compare figure 6.36, which shows a detector with similar geometries. In the measurement for the fiber-coupled detector no polarization maintaining fiber has been used, therefore, we are dealing here with unpolarized light and the absorption for it lies between the measurement for TM and TE polarized light. Considering this fact a detection efficiency of 80% makes sense, since the absorption of the structure in of the same order.

All in all we demonstrated that we have been able to fabricate ultra-small working detectors with an active area of only 3×3 µm^2 and in addition, estimated that our structures are able to detect pulses containing average single-digit photon numbers with our lock-in measurement.

8

PIXELATED DETECTORS DESIGNS

This chapter is about pixelated superconducting photodetectors and our first designs and approaches to create scalable detector arrays. SNSPDs have been used for different application such as astrophysics [95] and infrared spectroscopy [96]. The advantages of the single superconducting detectors could hereby be used to create fast and highly efficient detector arrays with small pixels.

There are different approaches to manufacture such detector arrays. One way is to just contact each detector on its own [97, 98], which leads to the fact that the finished arrays need $2N$ contacts, whereby N stands for the number of detectors in the array.

The second possibility is to utilize a multilayer structure demonstrated in [99, 100], like the ones used for conventional photodetector arrays. These multilayer designs enable even larger arrays, since the contacts scale with $\sqrt{N}$.

8.1 SINGLE LAYER DESIGN

The first detector design we want to introduce is a single layer design. Hereby we have fabricated multiple detectors and connected them in series, with one additional contact between each detector. A SEM picture of three connected detectors is displayed in figure 8.1. This design uses $N + 1$ contacts for an array with N detectors, giving us a slight advantage compared to the designs which contact each detector separately.

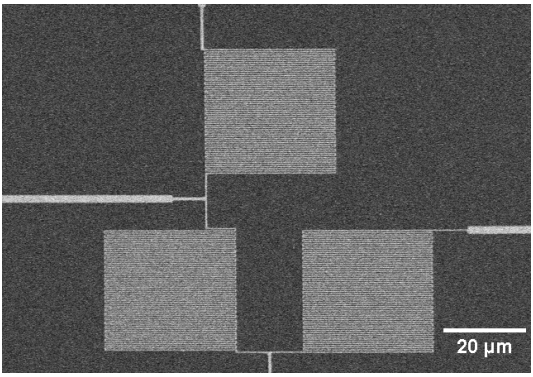

Figure 8.1: SEM picture of the single layer pixel detector design.

After cooling down the structure and confirming its superconducting properties, we have been able to reliably detect which detector has been illuminated with our free space setup. For this we have focused the incoming laser beam only on one of the three detectors and measured the response of all structures, whereby only one structure showed a measurable voltage drop. This procedure has been repeated for all three detector structures, with the same result that only the illuminated detector is showing a response. We only used three detectors, since the cryostat has at the moment only four small copper contact cables, which we can use to connect the detector structure.

Nevertheless, we successfully demonstrated the working principle of our array structure, in which the number of detectors scales linearly with the number of needed contacts. However, for larger detector arrays a multilayer design is more efficient.

8.2 STACKED LAYER DESIGN

The second detector design we want to demonstrate is a multilayer design in which the number of detectors scales with the square root of the contacts and exactly $2 \cdot \sqrt{N}$ contacts are needed for N detectors. Hereby we have used a typical design which is already utilized in conventional photodetector arrays. To understand the working principle of this design we first have to look at the fabrication process which is a multilayer process with three different EBL runs.

The first step is the creation of a Cr etching mask, which covers the big contact pads, as well as the detector structures and the horizontal connection lines. A SEM picture of the afterwards etched Nb structure is displayed in figure 8.2.

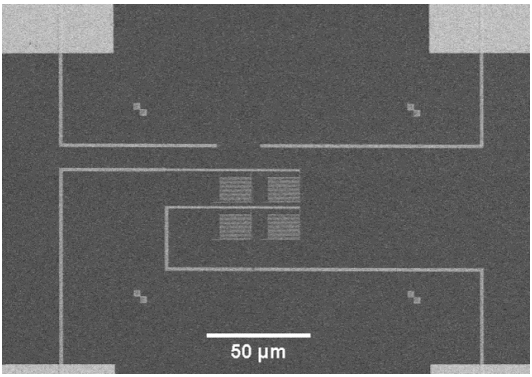

Figure 8.2: SEM picture of the first layer of the multi layer pixel detector design, where one can see the horizontal connections lines and detector structures.

In the second step we used EBL and e-gun evaporation to create an insulating layer on some of the Nb connection lines, where the layers will cross, to prevent short circuits between the first connection lines and the second ones. As insulation layer we have used Al_2O_3. The result of this step is depicted in figure 8.3.

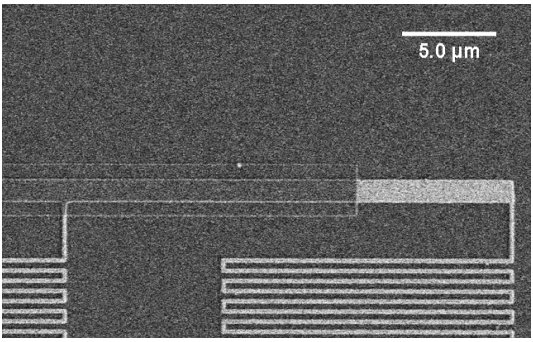

Figure 8.3: Zoomed-in SEM picture of the second layer of the multi layer pixel detector design. The Al_2O_3 layer covers the crossing section of the two conducting layers.

In the third step we have evaporated the last connection lines and big contacts pads using Au, since is exhibits good conducting properties. A zoomed in SEM picture of it can be seen in figure 8.4. Thanks to the insulation Al_2O_3, we are able to cross the different connection lines. The new Au lines connects the unconnected ends of the detectors with the other two contact pads.

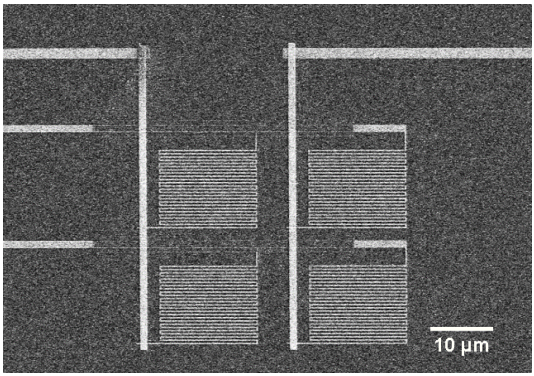

Figure 8.4: Zoomed in SEM picture of the third layer of the multi layer pixel detector design with vertical connection lines.

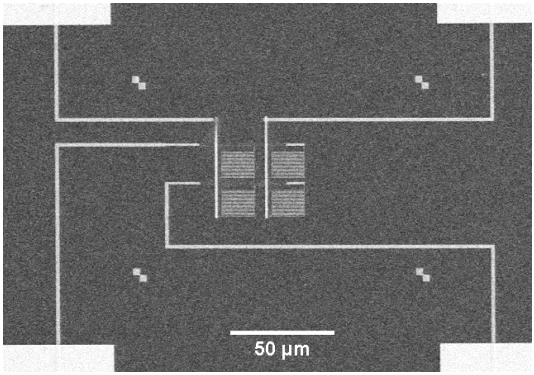

Figure 8.5: SEM picture of the whole finished multi layer pixel detector.

In figure 8.5 we present a SEM image of the whole pixel array structure with all connection lines. With this picture we are now able to completely explain the working principle of the multilayer structure and can understand how we can connect four detectors with only four contacts. Let us assume we want measure the bottom right detector, for this structure we need to

measure the resistance between two right contact pads, for the upper left detector for example we would need the two left pads. With this schema we are able to measure each detector structure individually. In addition, this design is completely scalable, for example a 4×4 detector array would need 8 contacts.

Sadly after cooling down we were not able to measure any detector response, although we could confirm the superconducting state of the sample. After reviewing the structure we realized that the structure is not working, due to its superconducting properties and the excellent conducting properties of the Au. As a superconducting wire exhibits no DC resistivity the current could just travel through the whole other three detectors to reach the two measured contact pads. This reveals the need of a diode or resistor before each detector structure, to avoid this problem, which is still work in progress.

Nevertheless, we have introduced a scalable pixel detector design, which theoretically should be usable after some more engineering. This structure would than inherit all the previous excellent properties of the detector structures demonstrated in this thesis.

9

CONCLUSION AND OUTLOOK

In this thesis highly efficient, ultra-small and plasmonic enhanced superconducting photo detectors for the visible and infrared spectral region were studied and investigated through simulations and measurements on manufactured samples. The detection efficiency was confirmed by lock-in measurements, which have revealed the possibility to detect even single photons.

In the first chapter we reviewed the fundamentals of plasmonic systems, which confirmed the requirement of a negative real part of the dielectric function for plasmon excitations and demonstrated a way to enhance the absorption of our plasmonic structures up to almost 100%.

The theory was followed by a brief discussion of superconductivity and SNSPDs, hereby we discovered that SNSPDs use their superconducting to normal conducting phase transition to detect photons due to breaking of the superconductivity caused by incident photons. We realized that SNSPDs have four important properties. First, the detection efficiency, which is the product of absorption efficiency and read out efficiency. Second, the dark count rate, which informs how often the detector indicates the arrival of photons without an actual photon hitting the detector. Third, the timing jitter, which is the statistical accuracy of the response time. And forth, the recovery time, which scales with the kinetic inductance and hence with the length of the detector structure. This indicates that smaller detectors exhibit shorter recovery times and are therefore faster.

To be able to produce these detector structures, we used various fabrication techniques. The thin superconducting films were sputter deposited and afterwards structured utilizing electron beam lithography, which allowed for a precise and reproducible fabrication of these nanostructures. Moreover, we demonstrated the good quality of the used 20 nm thin NbN films, since

they exhibit a critical temperature of around 11 K, which is higher than the critical temperature of the 50 nm thick Nb films.

Since NbN exhibits the better superconducting properties, compared to our Nb films, we investigated its plasmonic properties with the help of different nanoantenna arrays. Starting with simulations which revealed tunable, well-modulated and relative narrow resonances. These resonances are fundamental nanoantenna dipole resonances and not $\lambda/2$-resonances and confirm the plasmonic properties of NbN. Measurements of fabricated arrays verified these results. In addition, we demonstrated a good thermal geometric stability of temperatures up to 600 °C and good plasmonic properties of temperatures up to 400 - 500 °C. Additionally, simulations of nanoantenna arrays on a perfect absorber substrate were carried out, which have confirmed an absorption of over 99% for these structures.

After proving the plasmonic properties of NbN we started simulating 20 nm thick nanowire arrays on a perfect absorber substrate, since they lay the foundation of the detector structures. These simulations revealed high absorbing, broad and tunable resonances with over 99% absorption over a wide spectral range. Hereby the plasmonic resonances shift red for larger wire widths due to their dipole nature. The corresponding fabricated samples confirmed these results and the FTIR measurements showed an absorption of over 95%. However, the high absorption is only valid for TM polarization due to the excited plasmons. In TE polarization, which represents the intrinsic absorption of the material, the maximum absorption is below 50% and drops for higher wavelengths due to the metallic behavior of the Nb-based materials. To ensure that the photons are indeed absorbed in the plasmonic structure, we simulated the electrical field distribution of one nanowire array and validated that the interaction happens at the plasmonic structure. Further simulations proved the angle of incidence independence of our plasmonic perfect absorber structure, which enables the use of 3D-printed micro-optics and the possibility of ultra-small detectors.

The designed active area of the detector is in principle like the plasmonic wire arrays, but this time with an active area of only 30×30 μm^2 and the different wires are connected at alternating ends to form one long continuous wire. The measured absorption of this over 90% smaller structure is comparable with the bigger wire arrays and also exhibits a maximum absorption of around 90 - 95%, at our target wavelength of 1140 nm. By measuring the critical temperature of the fabricated structures, we checked that the

fabrication process did not worsen the superconducting properties of our materials. The detector is able to recognize laser powers below 1 µW in TM polarization. In TE polarization a minimum of ≈ 2 µW is needed, confirming a stronger response and hence a higher detection efficiency for TM polarized light, which in addition, leads to a polarization-dependent response. The overall shape of the response resembles a curve, which ends in a plateau for high laser powers, since at this point the complete structure is in its normal conducting state due to the high laser power and the introduced heat. Since we noticed a second resonance at lower wavelengths, we performed an additional response measurement at 561 nm, which has confirmed the results measured before. The same simulations and measurements have been also carried out for 50 nm thick Nb structures, with slightly lower absorption, but with the overall same results as for the NbN.

The most typical design of SNSPDs is the meander structure, which is similar to the design of our polarization-dependent detectors. This grid-like design is normally sensitive to the polarization of the incoming light, in our case this effect is even stronger due to the plasmonic enhancement. To tackle this problem, we invented different polarization-independent detector designs and measured their absorption and response to an external light source. In the end we demonstrated that the classical meander design exhibits the highest detection efficiency, but only for TM polarization. For unpolarized light, on the other hand, the circular detector structures exhibit the best detection efficiency with its maximum absorption of around 90%. The absorption of the classical detector drops for unpolarized light to around 80% at a wavelength of 1140 nm, which is the mean between the absorption for TM and TE photons.

With 10 nm thick NbTiN films on a perfect absorber substrate we produced nanowire arrays with over 97% absorption in the visible spectral range, demonstrating the transferability of our concept to lower and theoretically also to much higher wavelengths.

After confirming the functionality of our concept, we fabricated ultrasmall detectors with an active area of only $3 \times 3\ \mu m^2$ by utilizing 3D-printed fiber optics for focusing and fiber chucks for precise alignment. These new structures were measured in our improved and completely fiber-coupled cryogenic setup. After the evaluation of measurements with the new design and setup, we have been able to calculate the number of the incoming photons on these detectors. With these results we have estimated that our

structures can measure pulses containing in average only single-digit photon numbers. This is an important step towards single photon detection, since it shows that already pulses with photon numbers on the order of single photons cause a change in our detector. However, due to the bad signal-to-noise ratio this is not possible without lock-in at the moment. In addition, we estimated that our detectors have at least a detection efficiency of about 80%, which corresponds with their absorption efficiency of around 80% for unpolarized light.

In the end, we demonstrated two different approaches to create scalable detector arrays, one single layer and one multilayer approach. Whereby the multilayer design enables even large arrays, since the electrical contacts only scale with the square root of the detector number.

All in all, we demonstrated that we are able to produce ultra-small, high absorbing and working photodetectors with our plasmonic perfect absorber approach. These structures can have an active area down to only $3 \times 3\ \mu m^2$ and in addition, we confirmed that they are able to detect statistically single photons.

9.1 OUTLOOK

In the future, we want to investigate the Nb-based structures further and improve the samples and the setup to be able to measure the time-dependent properties of our detectors. There are several possible approaches to achieve this. One is to investigate why the resistance of our samples is quite low compared to other thin films. A bigger resistance would lead to a larger detector response, and hence to a better signal-to-noise ratio, which would enable the time-resolved measurements. The second possibility is to improve the cryogenic setup even further, since at the moment we have to use a two meter long coaxial cable, which can act as antenna and therefore introduces additional noise.

In addition, the plasmonic perfect absorber principle can enable high absorbing photodetectors even further in the mid-infrared spectral range. This would allow the possibility to use them for mid-IR spectroscopy [101] or IR space telescopes [102].

The further investigation and improvement of the pixelated detector structures could also yield promising results, since these structure would than inherit all the previous excellent properties of the detectors demonstrated in this thesis and could later even be used in the mid-infrared spectral range.

A

ETCH RECIPES

Used gases:	Ar	15 sccm
	CHF_3	15 sccm
Pressure:		10 mTorr
RF:		200 W
DC:		-600 V
Microwave:		200 W
Magnet:		180 A
Etch rate:	Nb	4.4 $\frac{s}{nm}$
	NbN	4.5 $\frac{s}{nm}$
	NbTiN	4.5 $\frac{s}{nm}$

B

FIBER-COUPLED MEASUREMENT SETUP ERRORS

Component:	Losses/Attenuation:	Introduced measurement error:
Variable fiber attenuator: (Thorlabs VOA1064-FC)	29.2 – 99.999%	±5%
Fiber connector: ADAFC2 - Mating Sleeve	(10 ± 2)%	±5%
Bare fiber connector: BFT1 + Fiber Stop for the BFT1	up to 70%	±5%
Fiber and 3D fiber optics:		
1060XP SM fiber	≤ 2.1 dB/km	
3D IP-S fiber optics	0.5%	±1% (shrinkage)
Reflection on interfaces	5%	±1%

The ±5% are introduced by the Digital Optical Power and Energy Meter and its Standard Photodiode Power Sensors S122C (Ge Photodiode) since it has a measurement uncertainty of ±5%. The Losses/Attenuation of the first three passive components have all been measured with this device.

The losses of the fiber were taken from their data sheet and the losses of the 3D printed parts were calculated using [92] and then additional error of 1% was assumed since the 3D parts have slight manufacturing defects and shrinkage. The refraction at the interfaces was calculated using the different refractive indices and an additional error of 1% was assumed to account for measurement inaccuracies.

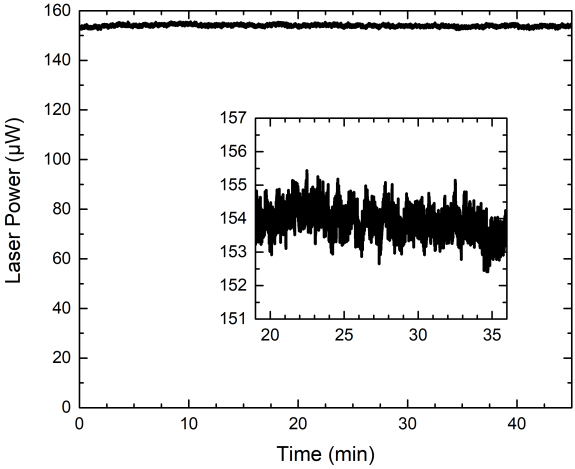

Figure B.1: Measured laser output power stability over 45 minutes.

The laser diode exhibits a stability of ±2% over 45 minutes.

With these parameters we are able to calculate the error for our photon number per pulse in figure 7.11 and 7.12, by using a propagation of uncertainty for equation (7.1). Hereby we take the introduced measurement uncertainty of the optical power meter into account and calculate the error of the average laser power P_{av}. By assuming that the different variables are uncorrelated, the following error results for P_{av} [94]:

$$(\Delta P_{\mathrm{av}})^2 = \left(\frac{\partial P_{\mathrm{av}}}{\partial P_{\mathrm{av\,m}}}\right)^2 \cdot (\Delta P_{\mathrm{av\,m}})^2 + \left(\frac{\partial P_{\mathrm{av}}}{\partial P_{\mathrm{av\,m}}}\right)^2 \cdot (\Delta P_{\mathrm{av\,s}})^2 \tag{B.1}$$

$$+ \left(\frac{\partial P_{\mathrm{av}}}{\partial A_1}\right)^2 \cdot (\Delta A_1)^2 + \left(\frac{\partial P_{\mathrm{av}}}{\partial A_2}\right)^2 \cdot (\Delta A_2)^2 \tag{B.2}$$

$$+ \left(\frac{\partial P_{\mathrm{av}}}{\partial C_1}\right)^2 \cdot (\Delta C_{11})^2 + \left(\frac{\partial P_{\mathrm{av}}}{\partial C_1}\right)^2 \cdot (\Delta C_{12})^2 \tag{B.3}$$

$$+ \left(\frac{\partial P_{\mathrm{av}}}{\partial C_2}\right)^2 \cdot (\Delta C_{21})^2 + \left(\frac{\partial P_{\mathrm{av}}}{\partial C_2}\right)^2 \cdot (\Delta C_{22})^2 \tag{B.4}$$

$$+ \left(\frac{\partial P_{\mathrm{av}}}{\partial C_{\mathrm{F}}}\right)^2 \cdot (\Delta C_{\mathrm{F}})^2 + \left(\frac{\partial P_{\mathrm{av}}}{\partial C_{3\mathrm{D}}}\right)^2 \cdot (\Delta C_{3\mathrm{D}})^2 \tag{B.5}$$

$$+ \left(\frac{\partial P_{\mathrm{av}}}{\partial C_{\mathrm{R}}}\right)^2 \cdot (\Delta C_{\mathrm{R}})^2 \,. \tag{B.6}$$

In this case $\Delta P_{\text{av m}}$ error of the measured laser power before the fiber attenuators, $\Delta P_{\text{av s}}$ represent the error caused by the instability of the laser, ΔA_1 and ΔA_2 are the errors of the measured attenuation caused by the fiber attenuators, ΔC_{11} and ΔC_{21} the measured errors of the attenuation caused by fiber connector, ΔC_{12} and ΔC_{22} the error introduced by the coupling of the fibers in the fiber connector and ΔC_{F} the error of the measured attenuation caused by the bare fiber connector. ΔC_{3D} represents the error of slight manufacturing defects and shrinkag of the 3D printed structures and ΔC_{R} the measurement inaccuracies of the refractive indices.

After calculating we obtain:

$$(\Delta P_{\text{av}})^2 = \left(\frac{P_{\text{av}}}{P_{\text{av m}}}\right)^2 \cdot (\Delta P_{\text{av m}})^2 + \left(\frac{P_{\text{av}}}{P_{\text{av m}}}\right)^2 \cdot (\Delta P_{\text{av s}})^2 \tag{B.7}$$

$$+ \left(\frac{P_{\text{av}}}{A_1}\right)^2 \cdot (\Delta A_1)^2 + \left(\frac{P_{\text{av}}}{A_2}\right)^2 \cdot (\Delta A_2)^2 \tag{B.8}$$

$$+ \left(\frac{P_{\text{av}}}{C_1}\right)^2 \cdot (\Delta C_{11})^2 + \left(\frac{P_{\text{av}}}{C_1}\right)^2 \cdot (\Delta C_{12})^2 \tag{B.9}$$

$$+ \left(\frac{P_{\text{av}}}{C_2}\right)^2 \cdot (\Delta C_{21})^2 + \left(\frac{P_{\text{av}}}{C_2}\right)^2 \cdot (\Delta C_{22})^2 \tag{B.10}$$

$$+ \left(\frac{P_{\text{av}}}{C_{\text{F}}}\right)^2 \cdot (\Delta C_{\text{F}})^2 + \left(\frac{P_{\text{av}}}{C_{3\text{D}}}\right)^2 \cdot (\Delta C_{3\text{D}})^2 \tag{B.11}$$

$$+ \left(\frac{P_{\text{av}}}{C_{\text{R}}}\right)^2 \cdot (\Delta C_{\text{R}})^2 . \tag{B.12}$$

We know $\Delta P_{\text{av m}}$ can be calculated with

$$\Delta P_{\text{av m}} = P_{\text{av m}} \cdot 5\%, \tag{B.13}$$

this also holds for the other variables, which resolves in:

$$\Delta P_{\text{av}} = P_{\text{av}} \cdot (5\%^2 + 2\%^2 + 5\%^2 + 5\%^2 + 5\%^2 + 2\%^2 + 5\%^2 + 2\%^2 \tag{B.14}$$

$$+ 5\%^2 + 1\%^2 + 1\%^2)^{0.5} \tag{B.15}$$

$$\approx P_{\text{av}} \cdot 12.81\% \tag{B.16}$$

LIST OF ACRONYMS

Al_2O_3	Aluminium oxide
Au	Gold
Cr	Chromium
EBL	Electron beam lithography
FTIR	Fourier-transform infrared spectrometer
IR	Infrared
LSP	Localized Surface plasmon
MgO	Magnesium oxide
NA	Numerical aperture
Nb	Niobium
NbN	Niobium nitride
NbTiN	Niobium titanium nitride
SEM	Scanning electron microscope
SiO_2	Silicon dioxide
SNSPD	Superconducting nanowire single photon detector
SPP	Surface plasmon polariton
SQUID	Superconducting quantum interference device
TE	Transverse-electric
TiN	Titanium nitride
TM	Transverse-magnetic
VTI	Variable temperature inset

LIST OF FIGURES

BIBLIOGRAPHY

[1] H. A. Atwater and A. Polman: *Plasmonics for improved photovoltaic devices.* Nature Materials **9**, 205–213 (2010).
DOI 10.1038/nmat2629, cit. on pp. 5, 35.

[2] D. G. Cahill, P. V. Braun, G. Chen, D. R. Clarke, S. Fan, K. E. Goodson, P. Keblinski, W. P. King, G. D. Mahan, A. Majumdar, H. J. Maris, S. R. Phillpot, E. Pop, and L. Shi: *Nanoscale thermal transport. II. 2003–2012.* Applied Physics Reviews **1**, 011305 (2014).
DOI 10.1063/1.4832615, cit. on pp. 5, 35.

[3] H. Aouani, M. Rahmani, M. Navarro-Cía, and S. A. Maier: *Third-harmonic-upconversion enhancement from a single semiconductor nanoparticle coupled to a plasmonic antenna.* Nature Nanotechnology **9**, 290–294 (2014).
DOI 10.1038/nnano.2014.27, cit. on pp. 5, 35.

[4] M. Hentschel, T. Utikal, H. Giessen, and M. Lippitz: *Quantitative Modeling of the Third Harmonic Emission Spectrum of Plasmonic Nanoantennas.* Nano Letters **12**, 3778–3782 (2012).
DOI 10.1021/nl301686x, cit. on pp. 5, 35.

[5] S. Bagheri, N. Strohfeldt, F. Sterl, A. Berrier, A. Tittl, and H. Giessen: *Large-Area Low-Cost Plasmonic Perfect Absorber Chemical Sensor Fabricated by Laser Interference Lithography.* ACS Sensors **1**, 1148–1154 (2016).
DOI 10.1021/acssensors.6b00444, cit. on pp. 5, 19, 33, 35.

[6] M. Sturaro, E. Della Gaspera, N. Michieli, C. Cantalini, S. M. Emamjomeh, M. Guglielmi, and A. Martucci: *Degenerately Doped Metal Oxide Nanocrystals as Plasmonic and Chemoresistive Gas Sensors.* ACS Applied Materials & Interfaces **8**, 30440–30448 (2016).
DOI 10.1021/acsami.6b09467, cit. on pp. 5, 17, 35.

[7] E. Herkert, F. Sterl, N. Strohfeldt, R. Walter, and H. Giessen: *Low-Cost Hydrogen Sensor in the ppm Range with Purely Optical Readout.* ACS Sensors **5**, 978–983 (2020).
DOI 10.1021/acssensors.9b02314, cit. on pp. 5, 35.

[8] A. Farag, M. Ubl, A. Konzelmann, M. Hentschel, and H. Giessen: *Utilizing niobium plasmonic perfect absorbers for tunable near- and mid-IR photodetection.* Optics Express **27**, 25012–25021 (2019). DOI 10.1364/OE.27.025012, cit. on pp. 5, 35.

[9] A. Eftekharian, H. Atikian, and A. H. Majedi: *Plasmonic superconducting nanowire single photon detector.* Optics Express **21**, 3043–3054 (2013). DOI 10.1364/OE.21.003043, cit. on pp. 5, 35.

[10] E. Scattolo, A. Cian, L. Petti, P. Lugli, D. Giubertoni, and G. Paternoster: *Near Infrared Efficiency Enhancement of Silicon Photodiodes by Integration of Metal Nanostructures Supporting Surface Plasmon Polaritrons.* Sensors **23**, 856 (2023). DOI 10.3390/s23020856, cit. on pp. 5, 35.

[11] S. Bagheri, N. Strohfeldt, M. Ubl, A. Berrier, M. Merker, G. Richter, M. Siegel, and H. Giessen: *Niobium as Alternative Material for Refractory and Active Plasmonics.* ACS Photonics **5**, 3298–3304 (2018). DOI 10.1021/acsphotonics.8b00530, cit. on pp. 5, 35, 36, 41.

[12] P. Karl, M. Ubl, M. Hentschel, P. Flad, Z. Y. Chiao, J. W. Yang, Y. J. Lu, and H. Giessen: *Optical properties of niobium nitride plasmonic nanoantennas for the near- and mid-infrared spectral range.* Optical Materials Express **10**, 2597–2606 (2020). DOI 10.1364/OME.403093, cit. on pp. 5, 29, 35, 36, 38–40, 42.

[13] N. Gisin, G. Ribordy, W. Tittel, and H. Zbinden: *Quantum cryptography.* Reviews of Modern Physics **74**, 145–195 (2002). DOI 10.1103/RevModPhys.74.145, cit. on pp. 5, 21.

[14] H.-K. Lo, M. Curty, and K. Tamaki: *Secure quantum key distribution.* Nature Photonics **8**, 595–604 (2014). DOI 10.1038/nphoton.2014.149, cit. on pp. 5, 21.

[15] K. Takemoto, Y. Nambu, T. Miyazawa, Y. Sakuma, T. Yamamoto, S. Yorozu, and Y. Arakawa: *Quantum key distribution over 120 km using ultrahigh purity single-photon source and superconducting single-photon detectors.* Scientific Reports **5**, 14383 (2015). DOI 10.1038/srep14383, cit. on pp. 5, 21.

[16] J. L. O'Brien: *Optical Quantum Computing.* Science **318**, 1567–1570 (2007). DOI 10.1126/science.1142892, cit. on pp. 5, 21.

[17] E. Knill, R. Laflamme, and G. J. Milburn: *A scheme for efficient quantum computation with linear optics*. Nature **409**, 46–52 (2001). DOI 10.1038/35051009, cit. on pp. 5, 21.

[18] W. Zhang, L. You, H. Li, J. Huang, C. Lv, L. Zhang, X. Liu, J. Wu, Z. Wang, and X. Xie: *NbN superconducting nanowire single photon detector with efficiency over 90% at 1550 nm wavelength operational at compact cryocooler temperature*. Science China Physics, Mechanics & Astronomy **60**, 120314 (2017). DOI 10.1007/s11433-017-9113-4, cit. on pp. 6, 21, 26, 45.

[19] K. M. Rosfjord, J. K. W. Yang, E. A. Dauler, A. J. Kerman, V. Anant, B. M. Voronov, G. N. Gol'tsman, and K. K. Berggren: *Nanowire single-photon detector with an integrated optical cavity and anti-reflection coating*. Optics Express **14**, 527–534 (2006). DOI 10.1364/OPEX.14.000527, cit. on pp. 6, 21, 45.

[20] N. I. Landy, S. Sajuyigbe, J. J. Mock, D. R. Smith, and W. J. Padilla: *Perfect Metamaterial Absorber*. Physical Review Letters **100**, 207402 (2008). DOI 10.1103/PhysRevLett.100.207402, cit. on pp. 6, 9, 17, 43.

[21] S. A. Maier: *Plasmonics: Fundamentals and Applications*, 1 edition, Springer US, 2007. ISBN 978-0-387-33150-8, cit. on pp. 9, 14, 16.

[22] P. Drude: *Zur Elektronentheorie der Metalle*. Annalen der Physik **306**, 566–613 (1900). DOI 10.1002/andp.19003060312, cit. on p. 11.

[23] X. Yin, T. Steinle, L. Huang, T. Taubner, M. Wuttig, T. Zentgraf, and H. Giessen: *Beam switching and bifocal zoom lensing using active plasmonic metasurfaces*. Light: Science & Applications **6**, e17016 (2017). DOI 10.1038/lsa.2017.16, cit. on p. 17.

[24] F. Sterl, N. Strohfeldt, S. Both, E. Herkert, T. Weiss, and H. Giessen: *Design Principles for Sensitivity Optimization in Plasmonic Hydrogen Sensors*. ACS Sensors **5**, 917–927 (2020). DOI 10.1021/acssensors.9b02436, cit. on p. 17.

[25] A. Tittl, P. Mai, R. Taubert, D. Dregely, N. Liu, and H. Giessen: *Palladium-based plasmonic perfect absorber in the visible wavelength range and its application to hydrogen sensing*. Nano Letters **11**, 4366–4369 (2011). DOI 10.1021/nl202489g, cit. on p. 19.

[26] C. M. Natarajan, M. G. Tanner, and R. H. Hadfield: *Superconducting nanowire single-photon detectors: physics and applications.* Superconductor Science and Technology **25**, 063001 (2012). DOI 10.1088/0953-2048/25/6/063001, cit. on pp. 21, 24, 25.

[27] D Rosenberg, A. J. Kerman, R. J. Molnar, and E. A. Dauler: *High-speed and high-efficiency superconducting nanowire single photon detector array.* Optics Express **21**, 1440–1447 (2013). DOI 10.1364/OE.21.001440, cit. on p. 21.

[28] A. Mukhtarova, L. Redaelli, D. Hazra, H. Machhadani, S. Lequien, M. Hofheinz, J.-L. Thomassin, F. Gustavo, J. Zichi, V. Zwiller, E. Monroy, and J.-M. Gérard: *Polarization-insensitive fiber-coupled superconducting-nanowire single photon detector using a high-index dielectric capping layer.* Optics Express **26**, 17697–17704 (2018). DOI 10.1364/OE.26.017697, cit. on p. 21.

[29] I. Esmaeil Zadeh, J. W. N. Los, R. B. M. Gourgues, V. Steinmetz, G. Bulgarini, S. M. Dobrovolskiy, V. Zwiller, and S. N. Dorenbos: *Single-photon detectors combining high efficiency, high detection rates, and ultra-high timing resolution.* APL Photonics **2**, 111301 (2017). DOI 10.1063/1.5000001, cit. on p. 21.

[30] S. Steinhauer, L. Yang, S. Gyger, T. Lettner, C. Errando-Herranz, K. D. Jöns, M. A. Baghban, K. Gallo, J. Zichi, and V. Zwiller: *NbTiN thin films for superconducting photon detectors on photonic and two-dimensional materials.* Applied Physics Letters **116**, 171101 (2020). DOI 10.1063/1.5143986, cit. on p. 21.

[31] S. Miki, T. Yamashita, H. Terai, and Z. Wang: *High performance fiber-coupled NbTiN superconducting nanowire single photon detectors with Gifford-McMahon cryocooler.* Optics Express **21**, 10208–10214 (2013). DOI 10.1364/OE.21.010208, cit. on p. 21.

[32] F. Marsili, V. B. Verma, J. A. Stern, S. Harrington, A. E. Lita, T. Gerrits, I. Vayshenker, B. Baek, M. D. Shaw, R. P. Mirin, and S. W. Nam: *Detecting single infrared photons with 93% system efficiency.* Nature Photonics **7**, 210–214 (2013). DOI 10.1038/nphoton.2013.13, cit. on p. 21.

[33] V. B. Verma, B. Korzh, F. Bussières, R. D. Horansky, S. D. Dyer, A. E. Lita, I. Vayshenker, F. Marsili, M. D. Shaw, H. Zbinden, R. P. Mirin, and S. W. Nam: *High-efficiency superconducting nanowire single-photon detectors fabricated from MoSi thin-films*. Optics Express **23**, 33792–33801 (2015).
DOI 10.1364/OE.23.033792, cit. on p. 21.

[34] R. M. Heath, M. G. Tanner, T. D. Drysdale, S. Miki, V. Giannini, S. A. Maier, and R. H. Hadfield: *Nanoantenna Enhancement for Telecom-Wavelength Superconducting Single Photon Detectors*. Nano Letters **15**, 819–822 (2015).
DOI 10.1021/nl503055a, cit. on p. 21.

[35] X. Hu, E. A. Dauler, R. J. Molnar, and K. K. Berggren: *Superconducting nanowire single-photon detectors integrated with optical nano-antennae*. Optics Express **19**, 17–31 (2011).
DOI 10.1364/OE.19.000017, cit. on p. 21.

[36] J. P. Sprengers, A. Gaggero, D. Sahin, S. Jahanmirinejad, G. Frucci, F. Mattioli, R. Leoni, J. Beetz, M. Lermer, M. Kamp, S. Höfling, R. Sanjines, and A. Fiore: *Waveguide superconducting single-photon detectors for integrated quantum photonic circuits*. Applied Physics Letters **99**, 181110 (2011).
DOI 10.1063/1.3657518, cit. on p. 21.

[37] G. N. Gol'tsman, O. Okunev, G. Chulkova, A. Lipatov, A. Semenov, K. Smirnov, B. Voronov, A. Dzardanov, C. Williams, and R. Sobolewski: *Picosecond superconducting single-photon optical detector*. Applied Physics Letters **79**, 705–707 (2001).
DOI 10.1063/1.1388868, cit. on p. 21.

[38] D. Van Delft and P. Kes: *The discovery of superconductivity*. Physics Today **63**, 38–43 (2010).
DOI 10.1063/1.3490499, cit. on p. 21.

[39] R. Gross and A. Marx: *Festkörperphysik*, 2 edition, Oldenbourg Wissenschaftsverlag, 2014.
ISBN 978-3-11-035869-8, cit. on pp. 21, 22.

[40] W. Meissner and R. Ochsenfeld: *Ein neuer Effekt bei Eintritt der Supraleitfähigkeit*. Die Naturwissenschaften **21**, 787–788 (1933).
DOI 10.1007/BF01504252, cit. on p. 22.

[41] F. London and H. London: *The electromagnetic equations of the supraconductor*. Proceedings of the Royal Society of London. Series A - Mathematical and Physical Sciences **149**, 71–88 (1935).
DOI 10.1098/rspa.1935.0048, cit. on p. 22.

[42] J. Bardeen, L. N. Cooper, and J. R. Schrieffer: *Theory of Superconductivity*. Physical Review **108**, 1175–1204 (1957). DOI 10.1103/PhysRev.108.1175, cit. on p. 23.

[43] S. Hunklinger: *Festkörperphysik*, 5 edition, De Gruyter, 2017. ISBN 9783110567755, cit. on pp. 24, 66.

[44] S. Steinhauer, S. Gyger, and V. Zwiller: *Progress on large-scale superconducting nanowire single-photon detectors*. Applied Physics Letters **118**, 100501 (2021). DOI 10.1063/5.0044057, cit. on p. 26.

[45] X. Yang, L. You, L. Zhang, C. Lv, H. Li, X. Liu, H. Zhou, and Z. Wang: *Comparison of Superconducting Nanowire Single-Photon Detectors Made of NbTiN and NbN Thin Films*. IEEE Transactions on Applied Superconductivity **28**, 1–6 (2018). DOI 10.1109/TASC.2017.2776288, cit. on p. 27.

[46] S. Miki, M. Fujiwara, M. Sasaki, B. Baek, A. J. Miller, R. H. Hadfield, S. W. Nam, and Z. Wang: *Large sensitive-area NbN nanowire superconducting single-photon detectors fabricated on single-crystal MgO substrates*. Applied Physics Letters **92**, 2006–2009 (2008). DOI 10.1063/1.2870099, cit. on p. 27.

[47] P. Karl, S. Mennle, M. Ubl, P. Flad, J.-W. Yang, T.-Y. Peng, Y.-J. Lu, and H. Giessen: *Niobium nitride plasmonic perfect absorbers for tunable infrared superconducting nanowire photodetection*. Optics Express **29**, 17087–17096 (2021). DOI 10.1364/OE.424148, cit. on pp. 29, 45, 50, 53, 54, 57–59, 64–70, 93, 94.

[48] P. Karl, S. Mennle, M. Ubl, M. Hentschel, P. Flad, J.-W. Yang, T.-Y. Peng, Y.-J. Lu, and H. Giessen: *Tunable infrared high absorbing polarization independent niobium nitride plasmonic perfect absorber nanowire photodetectors*. Optical Materials Express **12**, 2453–2461 (2022). DOI 10.1364/ome.458242, cit. on pp. 29, 45, 82, 85, 87, 89, 90, 92–94, 111.

[49] T. Shiino, S. Shiba, N. Sakai, T. Yamakura, L. Jiang, Y. Uzawa, H. Maezawa, and S. Yamamoto: *Improvement of the critical temperature of superconducting NbTiN and NbN thin films using the AlN buffer layer*. Superconductor Science and Technology **23**, 045004 (2010). DOI 10.1088/0953-2048/23/4/045004, cit. on p. 31.

[50] S. J. Lee and J. B. Ketterson: *Critical sheet resistance for the suppression of superconductivity in thin Mo-C films.* Physical Review Letters **64**, 3078–3081 (1990).
DOI 10.1103/PhysRevLett.64.3078, cit. on p. 31.

[51] S. Bagheri, H. Giessen, and F. Neubrech: *Large-Area Antenna-Assisted SEIRA Substrates by Laser Interference Lithography.* Advanced Optical Materials **2**, 1050–1056 (2014).
DOI 10.1002/adom.201400218, cit. on p. 33.

[52] J. H. Park, P. Ambwani, M. Manno, N. C. Lindquist, P. Nagpal, S. H. Oh, C. Leighton, and D. J. Norris: *Single-crystalline silver films for plasmonics.* Advanced Materials **24**, 3988–3992 (2012).
DOI 10.1002/adma.201200812, cit. on p. 35.

[53] E. K. Payne, K. L. Shuford, S. Park, G. C. Schatz, and C. A. Mirkin: *Multipole plasmon resonances in gold nanorods.* Journal of Physical Chemistry B **110**, 2150–2154 (2006).
DOI 10.1021/jp056606x, cit. on p. 35.

[54] M. R. Gonçalves, H. Minassian, and A. Melikyan: *Plasmonic resonators: fundamental properties and applications.* Journal of Physics D: Applied Physics **53**, 443002 (2020).
DOI 10.1088/1361-6463/ab96e9, cit. on p. 35.

[55] U. Guler, V. M. Shalaev, and A. Boltasseva: *Nanoparticle plasmonics: Going practical with transition metal nitrides.* Materials Today **18**, 227–237 (2015).
DOI 10.1016/j.mattod.2014.10.039, cit. on pp. 36, 41.

[56] A. Semenov, B. Günther, U. Böttger, H. W. Hübers, H. Bartolf, A. Engel, A. Schilling, K. Ilin, M. Siegel, R. Schneider, D. Gerthsen, and N. A. Gippius: *Optical and transport properties of ultrathin NbN films and nanostructures.* Physical Review B - Condensed Matter and Materials Physics **80**, 1–10 (2009).
DOI 10.1103/PhysRevB.80.054510, cit. on p. 36.

[57] T. Wieduwilt, A. Tuniz, S. Linzen, S. Goerke, J. Dellith, U. Hübner, and M. A. Schmidt: *Ultrathin niobium nanofilms on fiber optical tapers - A new route towards low-loss hybrid plasmonic modes.* Scientific Reports **5**, 1–12 (2015).
DOI 10.1038/srep17060, cit. on p. 36.

[58] M. W. Konevecki, K. L. Westra, B. T. Sullivan, K. E. Kornelson, and M. J. Brett: *Optical constants of reactively-sputtered NbN films.* Thin Solid Films **232**, 228–231 (1993).
DOI 10.1016/0040-6090(93)90013-F, cit. on p. 36.

[59] J. C. Ndukaife, V. M. Shalaev, and A. Boltasseva: *Plasmonics—turning loss into gain*. Science **351**, 334–335 (2016). DOI 10.1126/science.aad9864, cit. on p. 36.

[60] J. C. Ndukaife, A. V. Kildishev, A. G. A. Nnanna, V. M. Shalaev, S. T. Wereley, and A. Boltasseva: *Long-range and rapid transport of individual nano-objects by a hybrid electrothermoplasmonic nanotweezer*. Nature Nanotechnology **11**, 53–59 (2016). DOI 10.1038/nnano.2015.248, cit. on p. 36.

[61] S. Bagheri, C. M. Zgrabik, T. Gissibl, A. Tittl, F. Sterl, R. Walter, S. De Zuani, A. Berrier, T. Stauden, G. Richter, E. L. Hu, and H. Giessen: *Large-area fabrication of TiN nanoantenna arrays for refractory plasmonics in the mid-infrared by femtosecond direct laser writing and interference lithography [Invited]*. Optical Materials Express **5**, 2625–2633 (2015). DOI 10.1364/OME.5.002625, cit. on pp. 36, 41.

[62] T. Weiss, G. Granet, N. A. Gippius, S. G. Tikhodeev, and H. Giessen: *Matched coordinates and adaptive spatial resolution in the Fourier modal method*. Optics Express **17**, 8051–8061 (2009). DOI 10.1364/OE.17.008051, cit. on p. 37.

[63] T. Weiss, N. A. Gippius, S. G. Tikhodeev, G. Granet, and H. Giessen: *Efficient calculation of the optical properties of stacked metamaterials with a Fourier modal method*. Journal of Optics A: Pure and Applied Optics **11**, 114019 (2009). DOI 10.1088/1464-4258/11/11/114019, cit. on p. 37.

[64] L. Novotny: *Effective Wavelength Scaling for Optical Antennas*. Physical Review Letters **98**, 266802 (2007). DOI 10.1103/PhysRevLett.98.266802, cit. on p. 38.

[65] C. Langrock, E. Diamanti, R. V. Roussev, Y. Yamamoto, M. M. Fejer, and H. Takesue: *Highly efficient single-photon detection at communication wavelengths by use of upconversion in reverse-proton-exchanged periodically poled $LiNbO_3$ waveguides*. Optics Letters **30**, 1725–1727 (2005). DOI 10.1364/OL.30.001725, cit. on p. 38.

[66] Y. Saito, S. Kawata, H. Nakane, and H. Adachi: *Emission characteristics of niobium nitride field emitters*. Applied Surface Science **146**, 177–181 (1999). DOI 10.1016/S0169-4332(99)00068-9, cit. on p. 41.

[67] U. Guler, A. Boltasseva, and V. M. Shalaev: *Refractory plasmonics.* Science **344**, 263–264 (2014).
DOI 10.1126/science.1252722, cit. on p. 41.

[68] P. Nagpal, D. P. Josephson, N. R. Denny, J. DeWilde, D. J. Norris, and A. Stein: *Fabrication of carbon/refractory metal nanocomposites as thermally stable metallic photonic crystals.* Journal of Materials Chemistry **21**, 10836 (2011).
DOI 10.1039/c1jm10997a, cit. on p. 41.

[69] G. V. Naik, J. L. Schroeder, X. Ni, A. V. Kildishev, T. D. Sands, and A. Boltasseva: *Titanium nitride as a plasmonic material for visible and near-infrared wavelengths.* Optical Materials Express **2**, 478–489 (2012).
DOI 10.1364/OME.2.000478, cit. on p. 41.

[70] L. Gui, S. Bagheri, N. Strohfeldt, M. Hentschel, C. M. Zgrabik, B. Metzger, H. Linnenbank, E. L. Hu, and H. Giessen: *Nonlinear Refractory Plasmonics with Titanium Nitride Nanoantennas.* Nano Letters **16**, 5708–5713 (2016).
DOI 10.1021/acs.nanolett.6b02376, cit. on p. 41.

[71] U. Guler, G. V. Naik, A. Boltasseva, V. M. Shalaev, and A. V. Kildishev: *Performance analysis of nitride alternative plasmonic materials for localized surface plasmon applications.* Applied Physics B: Lasers and Optics **107**, 285–291 (2012).
DOI 10.1007/s00340-012-4955-3, cit. on p. 41.

[72] A. Kharitonov and S. Kharintsev: *Tunable optical materials for multi-resonant plasmonics: from TiN to TiON [Invited].* Optical Materials Express **10**, 513–531 (2020).
DOI 10.1364/ome.382160, cit. on p. 41.

[73] L. Braic, N. Vasilantonakis, A. Mihai, I. J. Villar Garcia, S. Fearn, B. Zou, N. M. Alford, B. Doiron, R. F. Oulton, S. A. Maier, A. V. Zayats, and P. K. Petrov: *Titanium Oxynitride Thin Films with Tunable Double Epsilon-Near-Zero Behavior for Nanophotonic Applications.* ACS Applied Materials & Interfaces **9**, 29857–29862 (2017).
DOI 10.1021/acsami.7b07660, cit. on p. 41.

[74] K. A. Arpin, M. D. Losego, A. N. Cloud, H. Ning, J. Mallek, N. P. Sergeant, L. Zhu, Z. Yu, B. Kalanyan, G. N. Parsons, G. S. Girolami, J. R. Abelson, S. Fan, and P. V. Braun: *Three-dimensional self-assembled photonic crystals with high temperature stability for thermal emission modification.* Nature Communications **4**, 2630 (2013).
DOI 10.1038/ncomms3630, cit. on p. 41.

[75] G. Albrecht, M. Ubl, S. Kaiser, H. Giessen, and M. Hentschel: *Comprehensive Study of Plasmonic Materials in the Visible and Near-Infrared: Linear, Refractory, and Nonlinear Optical Properties.* ACS Photonics **5**, 1058–1067 (2018).
DOI 10.1021/acsphotonics.7b01346, cit. on p. 41.

[76] G. Albrecht, S. Kaiser, H. Giessen, and M. Hentschel: *Refractory Plasmonics without Refractory Materials.* Nano Letters **17**, 6402–6408 (2017).
DOI 10.1021/acs.nanolett.7b03303, cit. on p. 41.

[77] M. Fenker, H. Kappl, O. Banakh, N. Martin, and J. Pierson: *Investigation of Niobium oxynitride thin films deposited by reactive magnetron sputtering.* Surface and Coatings Technology **201**, 4152–4157 (2006).
DOI 10.1016/j.surfcoat.2006.08.104, cit. on p. 42.

[78] A. J. Kerman, E. A. Dauler, J. K. W. Yang, K. M. Rosfjord, V. Anant, K. K. Berggren, G. N. Gol'tsman, and B. M. Voronov: *Constriction-limited detection efficiency of superconducting nanowire single-photon detectors.* Applied Physics Letters **90**, 101110 (2007).
DOI 10.1063/1.2696926, cit. on p. 46.

[79] J. Kischkat, S. Peters, B. Gruska, M. Semtsiv, M. Chashnikova, M. Klinkmüller, O. Fedosenko, S. Machulik, A. Aleksandrova, G. Monastyrskyi, Y. Flores, and W. Ted Masselink: *Mid-infrared optical properties of thin films of aluminum oxide, titanium dioxide, silicon dioxide, aluminum nitride, and silicon nitride.* Applied Optics **51**, 6789–6798 (2012).
DOI 10.1364/AO.51.006789, cit. on p. 47.

[80] R. Walter, A. Tittl, A. Berrier, F. Sterl, T. Weiss, and H. Giessen: *Large-Area Low-Cost Tunable Plasmonic Perfect Absorber in the Near Infrared by Colloidal Etching Lithography.* Advanced Optical Materials **3**, 398–403 (2015).
DOI 10.1002/adom.201400545, cit. on p. 57.

[81] N. Liu, M. Mesch, T. Weiss, M. Hentschel, and H. Giessen: *Infrared Perfect Absorber and Its Application As Plasmonic Sensor*. Nano Letters **10**, 2342–2348 (2010).
DOI 10.1021/nl19041033, cit. on p. 57.

[82] S. N. Dorenbos, E. M. Reiger, N. Akopian, U. Perinetti, V. Zwiller, T. Zijlstra, and T. M. Klapwijk: *Superconducting single photon detectors with minimized polarization dependence*. Applied Physics Letters **93**, 161102 (2008).
DOI 10.1063/1.3003579, cit. on p. 81.

[83] E. F. C. Driessen, F. R. Braakman, E. M. Reiger, S. N. Dorenbos, V. Zwiller, and M. J. A. de Dood: *Impedance model for the polarization-dependent optical absorption of superconducting single-photon detectors*. The European Physical Journal Applied Physics **47**, 10701 (2009).
DOI 10.1051/epjap/2009087, cit. on p. 81.

[84] A. Poppe, A. Fedrizzi, R. Ursin, H. R. Boehm, T. Loruenser, O. Maurhardt, M. Peev, M. Suda, C. Kurtsiefer, H. Weinfurter, T. Jennewein, and A. Zeilinger: *Practical quantum key distribution with polarization entangled photons*. Optics Express **12**, 3865–3871 (2004).
DOI 10.1364/OPEX.12.003865, cit. on p. 81.

[85] J Huang, W. J. Zhang, L. X. You, X. Y. Liu, Q Guo, Y Wang, L Zhang, X. Y. Yang, H Li, Z Wang, and X. M. Xie: *Spiral superconducting nanowire single-photon detector with efficiency over 50% at 1550 nm wavelength*. Superconductor Science and Technology **30**, 074004 (2017).
DOI 10.1088/1361-6668/aa6d03, cit. on p. 81.

[86] V. B. Verma, F. Marsili, S. Harrington, A. E. Lita, R. P. Mirin, and S. W. Nam: *A three-dimensional, polarization-insensitive superconducting nanowire avalanche photodetector*. Applied Physics Letters **101**, 251114 (2012).
DOI 10.1063/1.4768788, cit. on p. 81.

[87] X. Chi, K. Zou, C. Gu, J. Zichi, Y. Cheng, N. Hu, X. Lan, S. Chen, Z. Lin, V. Zwiller, and X. Hu: *Fractal superconducting nanowire single-photon detectors with reduced polarization sensitivity*. Optics Letters **43**, 5017–5020 (2018).
DOI 10.1364/OL.43.005017, cit. on p. 81.

[88] L. Bremer, K. Weber, S. Fischbach, S. Thiele, M. Schmidt, A. Kaganskiy, S. Rodt, A. Herkommer, M. Sartison, S. L. Portalupi, P. Michler, H. Giessen, and S. Reitzenstein: *Quantum dot single-photon emission coupled into single-mode fibers with 3D printed micro-objectives*. APL Photonics **5**, 106101 (2020). DOI 10.1063/5.0014921, cit. on p. 101.

[89] M. Sartison, K. Weber, S. Thiele, L. Bremer, S. Fischbach, T. Herzog, S. Kolatschek, M. Jetter, S. Reitzenstein, A. Herkommer, P. Michler, S. L. Portalupi, and H. Giessen: *3D printed micro-optics for quantum technology: Optimised coupling of single quantum dot emission into a single-mode fibre*. Light: Advanced Manufacturing **2**, 103 (2021). DOI 10.37188/lam.2021.006, cit. on pp. 101, 102.

[90] J. Schwab, K. Weber, J. Drozella, C. Jimenez, A. Herkommer, L. Bremer, S. Reitzenstein, and H. Giessen: *Coupling light emission of single-photon sources into single-mode fibers: mode matching, coupling efficiencies, and thermo-optical effects*. Optics Express **30**, 32292–32305 (2022). DOI 10.1364/OE.465101, cit. on p. 101.

[91] P. Ruchka, S. Hammer, M. Rockenhaeuser, R. Albrecht, J. Drozella, S. Thiele, H. Giessen, and T. Langen: *Microscopic 3D printed optical tweezers for atomic quantum technology*. Quantum Science and Technology **7**, 045011 (2022). DOI 10.1088/2058-9565/ac796c, cit. on p. 101.

[92] M. Schmid, D. Ludescher, and H. Giessen: *Optical properties of photoresists for femtosecond 3D printing: refractive index, extinction, luminescence-dose dependence, aging, heat treatment and comparison between 1-photon and 2-photon exposure*. Optical Materials Express **9**, 4564–4577 (2019). DOI 10.1364/OME.9.004564, cit. on pp. 101, 129.

[93] M. D. Eisaman, J. Fan, A. Migdall, and S. V. Polyakov: *Invited Review Article: Single-photon sources and detectors*. Review of Scientific Instruments **82**, 071101 (2011). DOI 10.1063/1.3610677, cit. on p. 108.

[94] H. J. Eichler, H.-D. Kronfeldt, and J. Sahm: *Das neue Physikalische Grundpraktikum*. Springer-Lehrbuch, 3 edition, Springer Berlin Heidelberg, 2016. ISBN 978-3-662-49022-8, cit. on pp. 112, 130.

[95] R. W. Romani, A. J. Miller, B. Cabrera, S. W. Nam, and J. M. Martinis: *Phase-resolved Crab Studies with a Cryogenic Transition-Edge Sensor Spectrophotometer*. The Astrophysical Journal **563**, 221–228 (2001). DOI 10.1086/323874, cit. on p. 115.

[96] J. S. Dam, P. Tidemand-Lichtenberg, and C. Pedersen: *Room-temperature mid-infrared single-photon spectral imaging*. Nature Photonics **6**, 788–793 (2012). DOI 10.1038/nphoton.2012.231, cit. on p. 115.

[97] Q. Chen, B. Zhang, L. Zhang, R. Ge, R. Xu, Y. Wu, X. Tu, X. Jia, D. Pan, L. Kang, J. Chen, and P. Wu: *Sixteen-Pixel NbN Nanowire Single Photon Detector Coupled With 300-μm Fiber*. IEEE Photonics Journal **12**, 1–12 (2020). DOI 10.1109/JPHOT.2019.2954938, cit. on p. 115.

[98] W. Zhang, J. Huang, C. Zhang, L. You, C. Lv, L. Zhang, H. Li, Z. Wang, and X. Xie: *A 16-Pixel Interleaved Superconducting Nanowire Single-Photon Detector Array With A Maximum Count Rate Exceeding 1.5 GHz*. IEEE Transactions on Applied Superconductivity **29**, 1–4 (2019). DOI 10.1109/TASC.2019.2895621, cit. on p. 115.

[99] M. S. Allman, V. B. Verma, M. Stevens, T. Gerrits, R. D. Horansky, A. E. Lita, F. Marsili, A. Beyer, M. D. Shaw, D. Kumor, R. Mirin, and S. W. Nam: *A near-infrared 64-pixel superconducting nanowire single photon detector array with integrated multiplexed readout*. Applied Physics Letters **106**, 192601 (2015). DOI 10.1063/1.4921318, cit. on p. 115.

[100] V. B. Verma, R. Horansky, F. Marsili, J. A. Stern, M. D. Shaw, A. E. Lita, R. P. Mirin, and S. W. Nam: *A four-pixel single-photon pulse-position array fabricated from WSi superconducting nanowire single-photon detectors*. Applied Physics Letters **104**, 051115 (2014). DOI 10.1063/1.4864075, cit. on p. 115.

[101] J. Haas and B. Mizaikoff: *Advances in Mid-Infrared Spectroscopy for Chemical Analysis*. Annual Review of Analytical Chemistry **9**, 45–68 (2016). DOI 10.1146/annurev-anchem-071015-041507, cit. on p. 124.

[102] G. H. Rieke, G. S. Wright, T. Böker, J. Bouwman, L. Colina, A. Glasse, K. D. Gordon, T. P. Greene, M. Güdel, T. Henning, K. Justtanont, P.-O. Lagage, M. E. Meixner, H.-U. Nørgaard-Nielsen, T. P. Ray, M. E. Ressler, E. F. van Dishoeck, and C. Waelkens: *The Mid-Infrared Instrument for the James Webb Space Telescope, I: Introduction*. Publications of the Astronomical Society of the Pacific **127**, 584–594 (2015).
DOI 10.1086/682252, cit. on p. 124.

ACKNOWLEDGMENTS

During the time of my studies and doctoral thesis I received help from many different people, which helped to the successful completion of my thesis. Here, I would like to thank all those who supported and helped me throughout this time.

In particular, I would like to thank:

- Prof. Dr. Harald Giessen for offering me the PhD position in this interesting and important field of research.
- Prof. Dr. Maria Daghofer and Prof. Dr. Peter Michler for being part of my examination committee.
- Dr. Yu-Jung Lu and her team for providing us the NbN samples.
- Dr. Mario Hentschel, Monika Ubl and Philipp Flad, who are doing a great job by ensuring that our cleanroom is running and the help with the sample fabrication.
- Sandra Mennle for being a great bachelor/master student, office mate, helpful discussions and all the other help.
- Dr. Andy Steinmann for helpful discussions and all the other help.
- Dr. Tobias Steinle and the Stuttgart Instruments team for the help with the lasers.
- Prof. Dr. Thomas Weiss, Dr. Steffen Both and Sascha Böhrkircher for the help with the smatrix program.
- Dr. Ksenia Weber and Paul Ruchka from the 3D-printing team for great collaboration and sample fabrication.
- Gabriele Untereiner for helping with sample fabrication.
- Dr. Florian Mörz for being a great office mate and helpful discussions.

- Prof. Dr. Kai Müller and his team for providing us the NbTiN samples and help with the setup.
- Ralf Kamella and his team from the mechanical workshop for the fabrication and help with the design of mechanical components.
- The low temperature workshop for providing liquid helium and help with the cryostat.
- The IQST management and members for funding the thesis and the many interesting events.
- My family, who supported me during all situations and always believed in me.
- My good friends Michelle and Sandra for all the support.
- All present and former colleagues from PI4 for the nice and funny working atmosphere.